

Electronic Theses and Dissertations, 2004-2019

2019

Nanoplasmonics In Two-dimensional Dirac and Three-dimensional Metallic Nanostructure Systems

Alireza Safaei
University of Central Florida

 Part of the [Physics Commons](#)

Find similar works at: <https://stars.library.ucf.edu/etd>

University of Central Florida Libraries <http://library.ucf.edu>

This Doctoral Dissertation (Open Access) is brought to you for free and open access by STARS. It has been accepted for inclusion in Electronic Theses and Dissertations, 2004-2019 by an authorized administrator of STARS. For more information, please contact STARS@ucf.edu.

STARS Citation

Safaei, Alireza, "Nanoplasmonics In Two-dimensional Dirac and Three-dimensional Metallic Nanostructure Systems" (2019). *Electronic Theses and Dissertations, 2004-2019*. 6775.
<https://stars.library.ucf.edu/etd/6775>

NANOPLASMONICS IN TWO-DIMENSIONAL DIRAC AND THREE-
DIMENSIONAL METALLIC NANOSTRUCTURE SYSTEMS

by

ALIREZA SAFAEI

M.S. Sharif University of Technology, 2012

M.S. University of Central Florida, 2018

A dissertation submitted in partial fulfillment of the requirements
for the degree of Doctor of Philosophy
in the Department of Physics
in the College of Sciences
at the University of Central Florida
Orlando, Florida

Spring Term

2019

Major Professors:

Debashis Chanda

and

Michael N. Leuenberger

© 2019 Alireza Safaei

ABSTRACT

Surface plasmons are collective oscillation of electrons which are coupled to the incident electric field. Excitation of surface plasmon is a route to engineer the behavior of light in nanometer length scale and amplifying the light-matter interaction. This interaction is an outcome of near-field enhancement close to the metal surface which leads to plasmon damping through radiative decay to outgoing photons and nonradiative decay inside and on the surface of the material to create an electron-hole pair *via* interband or intraband Landau damping. Plasmonics in Dirac systems such as graphene show novel features due to massless electrons and holes around the Dirac cones. Linear band structure of Dirac materials in the low-momentum limit gives rise to the unprecedented optical and electrical properties. Electronical tunability of the plasmon resonance frequency through applying a gate voltage, highly confined electric field, and low plasmon damping are the other special properties of the Dirac plasmons. In this work, I will summarize the theoretical and experimental aspects of the electrostatically tunable systems made from monolayer graphene working in mid-infrared regime. I will demonstrate how a cavity-coupled nanopatterned graphene excites Dirac plasmons and enhances the light-matter interaction. The resonance frequency of the Dirac plasmons is tunable by applying a gate voltage. I will show how different gate-dielectrics, and the external conditions like the polarization and angle of incident light affect on the optical response of the nanostructure systems. I will then show the application of these nanodevices in infrared detection at room temperature by using plasmon-assisted hot carriers generation. An asymmetric nanopatterned graphene shows a high responsivity at room temperature which is unprecedented. At the end, I will demonstrate the properties of surface plasmons on 3D noble metals and its applications in light-funneling, photodetection, and light-focusing.

I dedicate this work to my beloved wife Zahra Tavakoli whose unconditional encouragement and support made it possible for me to complete my PhD program. I wish to express my heartfelt love to my parents, for their endless supports and love. To my family, I love you all.

ACKNOWLEDGMENTS

“For those who exercise patience, Allah (swt) will help and show a way out of every difficulty.”

First, I would like to acknowledge my advisor, Dr. Debashis Chanda and co-advisor, Dr. Michael N. Leuenberger, for their patience, comprehensive knowledge, and precious advices. I also appreciate my committee members Drs. Lei Zhai, and Eduardo Mucciolo for their advice and suggestions. I would like to thank my lab fellows, Dr. Sayan Chandra, Sushrut Modak, Abraham Vázquez-Guardado, Daniel Franklin and Muhammad Waqas Shabbir for helping me through my experiments and simulations. I would also like to thank the University of Central Florida, Department of Physics, College of Sciences, and NanoScience Technology Center for offering me access to this PhD program and correlated services.

I want to give my special appreciations to my family for their encouragement and most of all, my sweet wife for her continuous love, tolerating difficulties, patience, and inspiration words.

TABLE OF CONTENTS

LIST OF FIGURES	x
LIST OF ABBREVIATIONS.....	xiii
CHAPTER 1: INTRODUCTION	1
Background and motivation	1
2D Dirac plasmons	2
The behavior of electrons and phonons of graphene.....	3
Plasmon decay and hot carriers.....	5
Infrared photodetection	7
Plasmon-assisted Bolometric Effect	7
Plasmon-induced Photo-thermoelectric Effect.....	9
Phase shift due to plasmon excitation	10
The scope of this work	12
CHAPTER 2: ENHANCED LIGHT-GRAPHENE INTERACTION.....	20
Introduction	20
Theoretical model.....	23
Nanostructure Design	23
The Parameters of FDTD Simulation	26
Diffraction of the Surface Plasmons.....	27
Coupled Dipole Approximation	28
The Effect of Carrier Mobility.....	30
Fabrication and experimental results.....	33
Device Fabrication Process	33
Gate Dielectric	35
Light Absorption Measurement.....	37
Materials Characterization and Measurement	39
Plasmon-phonon Coupling	40
Conclusion.....	45
CHAPTER 3: THE EFFECTS OF ANGLE OF INCIDENCE, POLARIZATION AND PATTERNING ON DIRAC PLASMONS	47
Introduction	47
Plasmonic resonances in the complementary arrays	50

Plasmon Lifetime.....	50
Geometrical Tunability.....	51
Fabrication and characterization	55
Nanopatterning Monolayer Graphene	55
The Light Absorption of the Substrate	57
The Quality of the Gate Dielectric	58
Finding the Carrier Mobility.....	59
Geometric and electrostatic tunable absorption at normal incidence.....	60
Angle dependent infrared absorption	62
Effect of Angle of Incidence for the Cavity-coupled and Cavity-uncoupled Systems	62
Effect of Light Polarization on the Angular Response.....	66
Plasmon Decay Rate	68
Conclusion.....	68
CHAPTER 4: INFRARED DETECTION BASED ON DIRAC PLASMON-ASSISTED HOT CARRIER GENERATION	72
Introduction	72
Plasmon assisted hot carrier generation	74
Asymmetric Photo-thermoelectric Effect	74
Fabrication.....	75
Experimental Characterizations.....	76
Seebeck Coefficient Measurement	78
Photovoltage generation.....	79
Dirac Plasmon Decay	79
Nature of Generated Signal	80
FEM Simulation	81
Comparison of FEM Simulation and Experimental Results	83
D.C photoresponse	85
D.C Photo-thermoelectric Voltage Measurement	85
Functionality of the D.C Responsivity	86
Noise Equivalent Power	88
A.C photoresponse	88
A.C Photoresponse Measurement.....	88
Nanopatterning Effects on the Photoresponse.....	90

Response Time	91
Single-pixel imaging	92
Conclusion.....	93
CHAPTER 5: SURFACE PLASMON EXCITATION ON QUASI-3D NANOSTRUCTURES	94
Introduction	94
Light coupling	96
Quasi-3D Nanostructure Design.....	96
The Effect of Quality Factor of the Optical Cavity	98
The Dispersion of the Optical Cavity	99
Loss Mechanism	102
Experimental results	103
Conclusion.....	104
CHAPTER 6: PLASMON-ASSISTED MID-INFRARED PHOTODETECTION USING 3D NOBLE METALS	105
Introduction	105
Quasi-3D plasmonic crystal “light funnel”	107
Nanostructure Design	107
Angular Optical Response	109
Plasmon Loss Mechanism	111
Light detection.....	112
Detection Circuit.....	112
Detector Fabrication	113
Bolometer performance.....	115
Responsivity	115
Detectivity and Response Time.....	116
Conclusion.....	118
CHAPTER 7: PLASMON-ASSISTED LIGHT FOCUSING	120
Introduction	120
Focusing mechanism	123
Spatially Varying Gradient Phase Response	123
Cylindrical Optical Lens Phase Distribution	124
Lens design parameters	125

Figure of Merit of Optical Lenses	125
Volume of Focal Point.....	127
Efficiency of the Flat Lens	127
Focal Length Trend	128
Polarization dependent flat lens	129
The Effect of Periodicity	129
Confocal Measurement.....	131
Field Intensity of the Focal Line.....	132
Polarization independent flat lens	134
The Advantages of Double-layer Flat Lens.....	134
Fabrication	134
Filed Intensity of the Focal Point	137
Transmission efficiency	139
Conclusion.....	142
APPENDIX A: PUBLISHER’S PERMISSION.....	143
APPENDIX B: PUBLISHER’S PERMISSION.....	145
APPENDIX C: PUBLISHER’S PERMISSION.....	147
APPENDIX D: PUBLISHER’S PERMISSION.....	149
LIST OF REFERENCES	151

LIST OF FIGURES

Figure 1: The honeycomb lattice and Brillouin zone of graphene.....	4
Figure 2: Extraordinary absorption in cavity-coupled nanomesh graphene and the effect of carrier mobility on absorption enhancement.	24
Figure 3: Near-field distribution.	25
Figure 4: Simulation convergence.	27
Figure 5: Fabricated system and characterizations.	34
Figure 6: Carrier mobility measurement.	36
Figure 7: Fabricated system and dynamic tunable response.	38
Figure 8: Energy loss dispersion.	40
Figure 9: Comparison of cavity-coupled hole and disk arrays in graphene.	50
Figure 10: Exciting surface plasmon on graphene nanodisk and nanohole arrays.	52
Figure 11: Geometrical tunability.	54
Figure 12: Fabrication and characterization.	56
Figure 13: Light absorption of different layers.	57
Figure 14: Characterization and comparison of the hard (Al_2O_3) and soft (ion-gel) gate dielectrics.	58
Figure 15: Electrostatic doping of graphene.	59
Figure 16: Experimental and simulated results of enhanced light-matter interaction in the cavity-coupled patterned graphene.	60
Figure 17: Experimental and simulated results of enhanced light-matter interaction in the patterned graphene without optical cavity.	61
Figure 18: Angle dependent infrared absorption.	63
Figure 19: The absorption of angled incident light by the patterned graphene with nanohole array.	64
Figure 20: The absorption of angled incident light by the patterned graphene with nanodisk array.	65
Figure 21: The angular response for the polarized and unpolarized lights.	67
Figure 22: The plasmon decay rates.	68
Figure 23: Graphene detector architecture.	75

Figure 24: Light absorption maximization.	76
Figure 25: The Raman spectra of the graphene detectors.	77
Figure 26: The electrical and thermoelectric properties of the graphene samples.	78
Figure 27: FEM simulation results.	83
Figure 28: Circuit diagram of the D.C measurement.	86
Figure 29: The trend of D.C responsivity.	87
Figure 30: Circuit design of the AC measurement.	89
Figure 31: The effect of nanopatterning and the response time.	90
Figure 32: Single-pixel imaging.	92
Figure 33: The light absorption of the quasi-3D nanostructure.	97
Figure 34: The optical properties of the cavity and metasurface.	98
Figure 35: The dispersion of the optical cavity.	99
Figure 36: Loss process in the cavity-coupled hole-disk system.	101
Figure 37: Characterization and measurement results	103
Figure 38: Cavity-coupled quasi-3D plasmonic crystal “Light Funnel”.	108
Figure 39: Angular optical response and power loss.	109
Figure 40: Photodetection mechanism.	114
Figure 41: The bolometer performance.	116
Figure 42: Gradient phase shift and focusing.	123
Figure 43: Focal length and efficiency variation.	126
Figure 44: Phase shift.	128
Figure 45: SEM image and top view of electric field intensity at focus of the single layer flat lens.	130
Figure 46: Schematic of the confocal measurement method.	131
Figure 47: Focal point measurement of the single layer flat lens.	133
Figure 48: Focal point measurement of the polarization independent bilayer flat lens.	135
Figure 49: The light absorption spectrum of SU-8 polymer.	136
Figure 50: Comparison of the focal point in X-Z and Y-Z planes for the bi-layer lens with $P=1.3 \mu\text{m}$	137
Figure 51: Comparison of the focal point in X-Z and Y-Z planes for the bi-layer lens with $P=2.0 \mu\text{m}$	138

Figure 52: Transmission efficiency. 140

LIST OF ABBREVIATIONS

A.C	Alternating Current
AFM	Atomic Force Microscopy
CDA	Coupled Dipole Approximation
CNP	Charge Neutrality Point
CVD	Chemical Vapour Deposition
D.C	Direct Current
EBL	Electron Beam Lithography
EM	Electromagnetic
FDTD	Finite-Difference Time-Domain
FEM	Finite Element Modeling
FS	Frequency Selective
FTIR	Fourier-Transform Infrared Spectroscopy
FWHM	Full Width at Half Maximum
GNR	Graphene NanoRibbon
GO	Graphene Oxide
GPs	Graphene Plasmons
hLSP	hybrid Localized Surface Plasmon
IR	Infrared
LO	Longitudinal Optical Phonon
LSPs	Localized Surface Plasmons
LSPR	Localized Surface Plasmon Resonances
LWIR	Long-Wave Infrared
Mid-IR	Mid-Infrared
MWIR	Mid-Wave Infrared
NA	Numerical Aperture
NEP	Noise-Equivalent Power

NIR	Near-Infrared
PDMS	Poly Dimethylsiloxane
Ps	picosecond
RCWA	Rigorous Coupled Wave Analysis
RD	Relief-Depth
RGO	Reduced Graphene Oxide
RIE	Reactive Ion Etcher
ROIC	ReadOut Integrated Circuit
RPA	Random Phase Approximation
PTE	Photo-Thermoelectric
SEM	Scanning Electron Microscope
SERS	Surface Enhanced Raman Spectroscopy
SPs	Surface Plasmons
SPPPs	Surface Plasmon Phonon Polaritons
TO	Transverse Optical

CHAPTER 1: INTRODUCTION

Background and motivation

Light-matter interaction depends on the behavior of the fundamental particles within the volume of the matter. Therefore, the incident light has different impacts on two- and three-dimensional materials [1]. These effects not only set by the inherent properties of light, such as wavelength, polarization, chirality and the angle of incidence, but also depends on the properties of the material like, bandgap, dimensionality, Fermi level, carrier density [1, 2], *etc.* It is possible to control the optical and electronical properties of the thin films like refractive index, carrier mobility, bandgap and light emission by patterning them at the nanoscale [1-11]. Understanding and engineering the light-matter interaction at the nanoscale is an important and fast-growing field in science and technology. Nanoscale light-matter interaction is the most fundamental phenomenon to design the light absorbers [2, 3, 12], epsilon-zero metamaterials [13-15], optical modulators [16], the light beam steerers [10, 17], photovoltaic devices [18, 19], photodetectors [4, 8, 9], *etc.* Various strategies have been employed to control the light-matter interaction in nanostructures, such as: (i) coupling the nanostructures to an optical cavity [20], (ii) coupling the nanostructures to a photonic crystal cavity [21, 22], and (iii) excitation of surface plasmons on nanostructures [2, 3, 23].

In nanostructures, the incident electromagnetic wave at right momentum transfer can propagate on the metal-dielectric interface and excite collective oscillation modes of electrons on the metal surface called surface plasmons (SPs) [1, 24]. There are two modes of surface plasmon. The propagating mode called surface plasmon polariton which propagates along the interface of

metal and dielectric with a wavelength much smaller than the wavelength of the incident light. The localized surface plasmons (LSPs) are the other surface plasmon modes which are concentrated on the edges of the nanostructures, enhances the light-matter interaction. The free electrons couple to the incident light and respond collectively by resonant oscillation. The light-matter interaction of LSP is stronger due to tight localization of electric field [25, 26]. The resonance frequency is determined by the properties of light and nanostructure such as dielectric function of metal and surrounding medium, geometrical parameters, light polarization and angle of incidence. The surface plasmon are being used in nanophotonics for light concentration [27], enhancing hot-carrier generation [28-31], phase shift [10, 17, 32], photodetection [4, 33], engineering the optical properties of surface [10, 17, 34], *etc.* Applying surface plasmon miniaturizes the optical circuits with the feature sizes much smaller than the current technology.

2D Dirac plasmons

Exciting surface plasmon on graphene is a distinct technique to increase light absorption with exceptional properties. The surface plasmon couples the incident electromagnetic wave to the conductive medium that gives rise to direct absorption of light by monolayer graphene and provides the opportunity of electrical tunability of the plasmon resonance frequency through applying a gate voltage, high degree of electric field confinement, and low plasmon damping rate [35-38]. The increased light-matter interaction results in enhanced spontaneous emission rate close to the nanostructure edges [27, 39]. Exciting surface plasmons leads to increase light-graphene interaction, which can be utilized for infrared photodetectors [40], optical switching of infrared plasmon [41], and lasing in THz domain [42]. Plasmonics in Dirac systems such as graphene, topological insulators, and Weyl semimetals show distinctive features due to massless electrons

and holes around the Dirac nodes. Linear dispersion relation of Dirac materials around Dirac cones in Brillouine zone gives rise to the unprecedented optical and electrical properties [43].

Recent theoretical work suggests that it is possible to achieve an absorbance above 90% in the mid-IR range by connecting graphene with high carrier mobility of $\mu \sim 10,000 \text{ cm}^2/\text{Vs}$ to a silicon diffractive grating [44] and designing graphene nanoribbons [44, 45], or nanodisks [46]. In addition, the theoretically proposed antidot array on high-mobility graphene could achieve an absorbance of 50% in the THz regime [38]. It is to be stressed that these high carrier mobilities can be achieved only for mechanically exfoliated graphene. However, recent experiments tried to excite Dirac plasmon on nanoribbons [39, 47, 48] and nanodisks [49, 50] made of graphene grown by means of chemical vapour deposition (CVD), which resulted in a much lower electron mobility of around $\mu \sim 1,000 \text{ cm}^2/\text{Vs}$, demonstrate lower light absorption of 19% and 28%, respectively.

The behavior of electrons and phonons of graphene

Graphene is an atomically thick material made from a two-dimensional honeycomb array of carbon atoms, as shown in Figure 1. The interaction of adjacent carbon atoms in graphene creates special electronic and phononic behaviors. Each atom has four valence electrons in four atomic orbitals s , p_x , p_y and p_z . The overlapping of in-plane orbitals s , p_x and p_y hybridizes them into three sp^2 orbitals which generates strong σ -band and make rigid hexagonal lattice. The overlapping of the adjacent out-of-plane p_z orbitals is responsible for the low-energy linear behavior of graphene [1, 51]. Around the Dirac points, the energy dispersion of carriers can be described by a low energy Dirac Hamiltonian

$$H_G(\mathbf{k}) = h(\mathbf{k}) \cdot \boldsymbol{\sigma}, \quad (1)$$

where $h(\mathbf{k}) = [h_x(\mathbf{k}), h_y(\mathbf{k}), 0]$ and $\boldsymbol{\sigma} = [\boldsymbol{\sigma}_x, \boldsymbol{\sigma}_y, \boldsymbol{\sigma}_z]$ are Pauli matrices. For a small wavevector $\mathbf{q} = \mathbf{k} - \mathbf{K}$, the eigenvalues of the Hamiltonian are reduced to $h(\mathbf{k}) = \hbar v_F q$, which is a linear function of momentum q . The electron-electron interactions can only renormalize some parameters like Fermi velocity (v_F), without any effect on the electronic ground state of graphene.

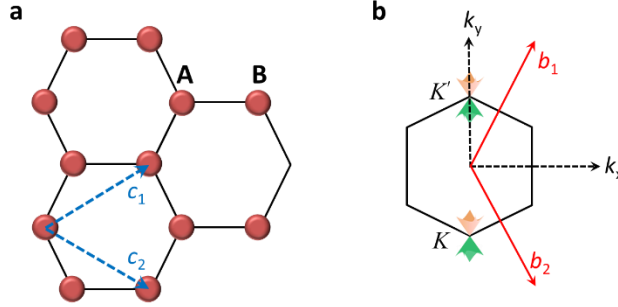


Figure 1: The honeycomb lattice and Brillouin zone of graphene.

(a) The atomic lattice structure of graphene. The arrows c_1 and c_2 show the lattice vectors of the lattice with two-atom unit cell indicated by **A** and **B**. (b) The first Brillouin zone of monolayer graphene with the reciprocal lattice vectors shown by b_1 and b_2 . The band structure of graphene in low-momentum limit has gapless Dirac cones at K and K' points.

The lattice vibrations of crystal in graphene called phonons have two different modes: Optical and Acoustic. The optical phonon energy is very high ($\omega_0 \approx 200 \text{ meV}$) originating from the rigid carbon-carbon bonds. The out-of-plane phonons called flexural phonons can occur in suspended graphene; however, since for graphene on substrate they get pinned to the substrate, their contribution is negligible. The acoustic phonons have a linear dispersion relation, $\omega_q = s|q|$, where $s \approx 10^6 \text{ cm s}^{-1}$. While the interaction of electrons and optical phonons can be significant at $\omega_0 \approx 200 \text{ meV}$, translational invariance of the graphene lattice makes the coupling of electron and long-wavelength acoustic phonons inefficient [11, 48, 51].

Plasmon decay and hot carriers

Excitation of surface plasmons make it possible to engineer the behavior of light on nanostructures and enhance the light-matter interaction [19, 52-54]. This amplified interaction is a result of the near-field enhancement close to the metal surface, following by plasmon damping via radiative decay and also nonradiative decay inside the material. The nonradiative decay happens due to Ohmic loss or Landau damping, i.e. generation of electron-hole pairs via interband or intraband transitions, electron-phonon interaction, and geometry effects. While the intraband transition occurs in the conduction band, the interband transition happens between other bands (such as the s- or d-band) and the conduction band [55-57].

The direct photon emission due to coherent electron oscillation is the reason of the radiative decay channel of plasmon damping. Increase in the size of nanoparticles enhances the radiative decay of the surface plasmons. In the opposite way, decrease in the size of the nanoparticle makes the non-radiative decay as the main plasmon decay channel.

Nonradiative decay of surface plasmon through Landau damping generates electron-hole pair. If the energy of these plasmon-assisted excited carriers is much larger than the thermally excited electron-hole pairs, they are called hot carriers. Generation of hot-carrier has lots of applications in photodetection, energy harvesting, phase transition and photocatalysis. The hot carriers can be used for chemical reactions [58] in metals and to make photocurrents in a semiconductor for the photovoltaic effect [18, 59]. The energy distribution of the generated hot carriers is a function of the metal band structure. For example, for copper and gold, the energy of the excited holes is higher than electrons; however, for aluminum and silver, the energy of electron are almost equal. The asymmetry between the generated hot electron and holes by the surface plasmon helps to collect more hot carriers before inelastic scattering. There are several factors to

design hot-carrier-based devices: (i) The energy distribution of the plasmon-assisted hot carriers, (ii) the subsequent elastic and inelastic scatterings, and (iii) the hot-carrier transport. The inelastic scatterings due to the Coulomb interaction give rise to the thermalization of the hot carriers among each other and reaching to their equilibrium temperature. Another inelastic scattering can happen due to the electron-phonon interaction results in the cooling of the carriers and reaching to the equilibrium temperature of the material lattice. For example, in graphene thermalization happens on a time scale of 100 fs , while cooling due to coupling to the phonons is much slower and occurs on a time scale of 10 ps .

The significance of graphene electrons is the ease of the thermalization of excited carriers without cooling by the lattice which is the regime of hot carriers. This regime is very important and attractive for the high-speed energy transportation like photodetectors and optical switches. The weak coupling of graphene electrons and lattice makes the population of hot carriers very stable. The scattering of electrons and high energy optical phonons ($\omega_0 \approx 200\text{ meV}$) is important only at high temperatures due to rigid carbon-carbon bonds. In addition, the large mismatch of the Fermi velocity ($v_F \approx 10^8\text{ cm s}^{-1}$) and the sound velocity ($s \approx 10^6\text{ cm s}^{-1}$) is the reason of weak inelastic scattering of electrons and acoustic phonons. As a result, in absence of substrate phonons, due to the inefficient scattering of carriers by the lattice, heating the carriers can keep them out of the equilibrium temperature of the lattice for a long time and increase their transduction length scale. While the hot carriers in the regular semiconductors like GaAs can only be generated at low temperatures [60], they can exist even at room temperature in graphene. These special properties of hot carriers in graphene candidate it as a special material for the hot carriers-based optoelectronics applications such as photodetection, energy harvesting and optical modulation.

Infrared photodetection

Infrared (IR) detection and imaging over atmospheric transparent 3-5 μm and 8-12 μm bands are increasingly becoming important for space explorations [61], spectroscopy [2, 11], meteorology [62], chemical/biological identification [63], target tracking [61] and night vision [64]. However, there are two major limitations in mid-IR detection and imaging. First of all, due to the low photon energy of mid-IR radiation, cryogenic cooling is required for high-sensitive detection based on low bandgap materials [62]. Various kinds of microbolometers offer uncooled detection of IR radiations [4, 21]. However, microbolometers suffer from low sensitivity, slow response and tedious multi-step complex lithographic processes [4]. The second drawback is the absence of frequency tunability for multi-spectral infrared detection/imaging. At present all cooled and uncooled mid-IR detectors are being “bucket” detectors generate integrated signal resulting in loss of spectral information [62]. Surface plasmon-assisted photodetection is an efficient way to overcome the current limitations of infrared detections. There are two general approaches to design plasmon-assisted photodetection: (i) Using the lossy plasmons as a mechanism of multispectral photodetection in infrared frequency domain by virtue of bolometric principle [65, 66]. (ii) Plasmon-assisted hot-carrier generation.

Plasmon-assisted Bolometric Effect

Light-matter interactions can be controlled by manipulating the electric and magnetic responses of a material. The fundamental order of LSP, the dipolar excitation, has the highest strength and its properties, i.e. resonance frequency and lifetime, are determined by the particle polarizability and lattice sum which depend on the metal/insulator dielectric functions and the geometrical parameters. This dependence gives a way to control and tailor the surface plasmon

resonances to desired frequencies. The main disadvantage of LSP excitation on the metal surface is the large plasmon decay rate mainly due to the finite metal conductivity that decreases the lifetime of the excited surface plasmon and induce losses in the form of heat dissipation. For a long time, this loss was considered to be a major limiting factor in realization of plasmonic devices but later this very loss is used as a benefit.

The lossy plasmons can be used as a mechanism for the “color” sensing in infrared frequency domain by virtue of bolometric principle. A quasi 3D plasmonic crystal consisting of vertically-separated complementary nanohole and nanodisk arrays coupled to an optical cavity is able to excite surface plasmon and increase the light absorption in infrared domain with a very narrow bandwidth. The general behavior of this complex system is determined by the interaction of optical cavity modes, hybrid plasmonic excitation on the disk array and vertical/horizontal coupling of the metallic dipolar elements. The geometric nature of this plasmonic crystal “funnels” the light through the subwavelength holes coupled to the disk array by exciting hybrid plasmon, which is dissipated in the form of resistive loss resulting from induced micro-currents on the edge of dipole elements (holes and disks). Surface patterning with a superlattice to sense the power dissipation with external biasing circuitry can be the detection mechanism. The frequency selective infrared absorption spectroscopy has proven to be a very important tool in the detection and identification of airborne chemicals by comparing infrared light absorption in presence and absence of airborne contaminants. The geometrical tunability and narrow bandwidth of the light absorption not only determines the contaminants, but also their concentration.

Plasmon-induced Photo-thermoelectric Effect

To overcome the limitations of infrared detection, *i.e.*, slow response, cryogenic cooling, spectral tunability, and low sensitivity, a material should be able to strongly absorb infrared radiation with actively tunable frequency bands. Moreover, the incident absorption should be detectable by a high-speed electronic detection mechanism at room temperature with low noise-equivalent power (NEP) [67, 68]. No known “bulk” material fulfils all of these requirements. Apart from the active material, the detection scheme should be efficient to generate strong signal and high detectivity along with ultrafast response time at room temperature. Photothermoelectric effect is an effective detection route to address these concerns [30, 69-72].

Photothermoelectric effect needs an active material with large Seebeck coefficient (S) and low electronic heat capacity (C_p) to generate an intense signal [71]. The two-dimensional material graphene offers some of these attributes due to its unique and tunable band dispersion relation [73-75]. In addition, since the monolayer graphene has much smaller C_p compared to bulk materials, it can generate much higher temperature difference for a specific absorbed power [71]. The picosecond response time of the photothermoelectric effect in monolayer graphene [1] candidates it as an appropriate material to generate an ultrafast and large photovoltage. However, because of the absence of bandgap and single-atom thickness, graphene absorption across the optical spectrum is very weak ($< 3\%$) [11, 76]. Recent attempts in exploiting photothermoelectric effect to generate photovoltage need high incident power to produce enough potential difference [33, 71, 72]. Furthermore, because of heating both the atomic lattice and the electron system in those detectors, they suffer from slow response [71].

The strong thermoelectricity in graphene which changes the charge mode to the energy mode can be used to increase the collection of hot carriers for photodetection. While in the thermoelectric effect, a spatial temperature gradient is used to generate voltage, in Peltier effect a charge current produces heat. While in the case of the thermoelectric and photothermoelectric effects a thermal gradient is introduced into both the lattice and the electron system, which results in a thermoelectric voltage in equilibrium when the electron diffusion current is equal and opposite to an electric current, plasmon-assisted photothermoelectric detection is based on the efficient heating of the charge carriers only, giving rise to an ultrafast response of the electron system while bypassing the lattice system, thereby leading to the fast buildup of a thermoelectric voltage. This is the plasmon-induced hot-carrier Seebeck effect. This effect is especially pronounced when the electron-electron interaction is much larger than the electron-phonon interaction, which is the case for graphene. The plasmon-induced hot-carrier Seebeck effect takes advantage of the strong asymmetric absorption provided by the LSP-carrier coupling across the detector active area. The strong asymmetry is possible because of the strong absorption of the incident radiation. Due to the ultrafast plasmonic excitation and charge transport in graphene, a fast photoresponse is expected[48].

Phase shift due to plasmon excitation

Conventional optical elements such as lenses, waveplates and polarizers function by adding phase delays to the propagating light gradually through optical path. The collected phase by propagating light through these lenses can be defined as $\Delta\varphi = \Delta n |\mathbf{k}| \Delta l$, where Δn is the refractive index difference between the surrounding medium and lens, $|\mathbf{k}|$ is the magnitude of wavenumber and Δl is the propagation distance. In the conventional lenses made from natural dielectrics and air medium, Δn is small which means that the thicknesses of these dielectric optical

components should be much larger than the wavelength of incoming light to accumulate 0 to π phase shift. That means reaching to subwavelength ultrathin lenses by conventional optical lenses is impossible. For fabrication of the compact and integrated optoelectronic devices such as CCD's, optical detectors, displays and even solar cells, the optical lenses should be miniaturized and ultracompact. Optical aberration (e.g. spherical and chromatic aberrations) is another constraint for operation of conventional dielectric optical lenses. Abbe-Rayleigh diffraction limit is a natural obstacle in regular optical lenses due to employing only far-field and lack of using near-field[77, 78]. Metamaterial optical components by abrupt changing of phase, amplitude or the polarization over the wavelength of the incident light using subwavelength optical scatterer, according to the Huygens principle[79] are able to form the optical wavefront of the incident wave into arbitrary shapes with subwavelength resolution[17, 80-116]. The optical response of these optical scatterers are spatially variable. The change in optical properties are achieved through scattering of the incident light beam by the coupled optical antenna sitting on an array or through transmission/reflection at lossy interface[17, 117-121]. Subwavelength resolution using the metamaterial surface lens can eliminate higher diffraction order and funnel the incident light beam into a single point that functions as propagating mode known as focal point and its location is characterized by the focal length[78, 90, 91, 94, 95, 101, 107, 122]. In addition, possibility of the optical impedance matching with that of free space by metamaterial interface can reduce reflection to the free space, leading to higher transmission efficiency[17]. Going beyond the Abbe-Rayleigh diffraction limit requires the involvement of evanescent field components which is possible by metasurfaces with wide range of spatial frequency elements and subwavelength resolution capability going beyond the current imaging technology[78, 104, 122-124].

One approach to engineer the phase response of the metasurface is fabrication of an inhomogeneous two dimensional (2D) or quasi 2D pattern based on metallic or polar dielectric nanostructure[17, 85-87, 89, 90, 92-103, 107-116, 125, 126]. Light beam impinging on a metasurface gives rise to excitation of surface plasmon on the metallic nanostructure with a specified antenna length (L_{res}) leading to coupling of the incident light beam to the metasurface. Strong interaction between the incident light beam and surface plasmon leads to abrupt phase change of the scattered electric field[17, 87, 89, 90, 92, 93, 102, 108, 109, 113, 114, 125, 126]. The generalized optical law for the first time has been shown for the V-shaped optical antenna array[108, 124]. Excitation of surface plasmon is due to charge oscillation inside the optical antenna derived by the incident electric field and in resonance frequency, the deriving optical field is in phase with the optical antenna current, but varying the length of the nanostructure gives rise to change in the resonance frequency and excited current leads or lags the incident field. A (quasi) 2D pattern comprised of optical antenna with different lengths can create a spatial variable phase response surface and mould the optical wavefront to any shape[17, 124].

The scope of this work

In this work I study the properties of the surface plasmon on nanopatterned monolayer graphene and quasi three-dimensional gold structures. In addition, I show the application of this plasmon-assisted enhanced light-matter interaction in the novel optoelectronics devices such as photodetectors and optical flat lens. In Chapter 2, a direct enhancement method in the light-graphene interaction is shown based on cavity coupled patterned graphene in a square array whereby the Fermi energy is tuned by means of an external gate voltage, leading to a predicted maximum absorption of 60% and dynamic tunability up to 2 μm which closely corroborate experimentally measured absorption of ~45% and gate voltage tunable spectral shift of ~2 μm in

monolayer graphene. Such high absorption and large spectral shift in monolayer graphene is observed, for the first time, due to the strong coupling between localized surface plasmon resonances on the nanomesh graphene and optical cavity modes. Unlike other metal pattern based plasmon excitations, this direct excitation of surface plasmon on graphene surface ensures 100% absorption in the monolayer graphene, in the right conditions. Moreover, absence of impurities (metals) like other indirect absorption enhancement methods ensures high carrier mobility.

The coupled system is relatively more tolerant to low carrier mobility of graphene compared to other techniques (when mobility goes down from $960 \text{ cm}^2/\text{V.s}$ to $250 \text{ cm}^2/\text{V.s}$, the maximum absorption changes from 45% to 31% experimentally). The feature sizes of nanostructures in this design are much larger than the previous nanoribbon/disk designs [49, 50][49, 50][49, 50][49, 50][49, 50] (present 330 nm vs 60-100 nm nanoribbon/disk) which reduce fabrication challenges for practical implementation. Further, a large area embossing-based nanoimprinting technique is used to pattern the graphene. This technique is more efficient and scalable compared to the e-beam lithography process typically used in other graphene plasmonic nanostructure designs.

I developed an analytical model based on the many-body physics that considered the effects of the electron-phonon interaction between the substrate and the electrons on the graphene, giving rise to a modified plasmon-phonon dispersion relation which resulted in accurate correspondence between theoretical predictions and experimental observations.

In Chapter 3, I modify the patterning and electrical doping of graphene to enhance the absorption of normal and non-normal incident light. Plasmons are qualitatively characterized by their lifetimes. Longer lifetime results in stronger electric field confinement, which manifests as higher and sharper absorption (lower FWHM) in the spectral response. Nanopatterning of

graphene introduces graphene edges, which play a vital role in modifying the light absorption spectrum. Edge scattering effects, radiative and non-radiative decay arising from Landau damping through interband and intraband transitions contribute collectively to increase the decay rates of the plasmonic excitations. Therefore, the fundamental question that arises is how critical is the role of graphene edge on the LSPs excitation, decay rate and overall absorption behavior of patterned graphene? In this chapter, in order to investigate these aspects I identified complementary nanostructures, i.e. nanoholes and nanodisks, such that the qualitative nature of the edges are similar. A direct comparison of these complementary structures elucidates the differences in the plasmonic excitations, the degree of electrostatic spectral tunability and polarization dependences as a function of incident angle. I have applied theoretical and experimental approaches to gain insight into the underlying physical phenomena.

I demonstrate the effect of graphene nanopatterning and the edges on the plasmon lifetime and the light absorption. The maximum achieved light absorption is experimentally measured 90% (60%) for the cavity coupled graphene nanodisk (nanohole) array for the specified geometry parameters and $E_F = -1\text{eV}$ which is independent of the light polarization. An ideal strategy to enhance the light-graphene interaction should be independent of the angle of the incident light (θ_i). I measured for the first time the dependence of the light absorption as a function of θ_i for s- and p-polarized light and showed they are in very good agreement with the simulated results. At the end I show the peak wavelength and moreover the magnitude of the absorption of the unpolarized light by the patterned graphene are almost independent of the angle of incidence for $\theta_i < 50^\circ$.

In Chapter 4, I show one of the applications of graphene plasmonics in photodetection. Recent reports have shown multiple ways to enhance light-matter interactions on monolayer graphene, however, attempts to convert the absorbed light into significant electrical signal for

photodetection have suffered due to the absence of bandgap. Unless new physical phenomena are discovered to circumvent the absence of bandgap limitation, graphene will remain as a scientific marvel without any practical usage.

In this chapter, I demonstrate, for the first time, an asymmetric plasmon-induced hot-carrier Seebeck photodetection scheme on monolayer graphene at room temperature that exhibits a remarkable responsivity of 2900 V/W, detectivity (D^*) of 1.1×10^9 Jones along with an ultrafast response of ~ 100 ns in the technologically relevant 8 – 12 μm band, the performance of which compares favorably even with present cryogenically cooled detection schemes.

This detection scheme is based on the generation of hot-carriers in graphene and outlines the processes involved in their efficient collection at the detector terminals. To develop the plasmon-assisted thermoelectric based photodetector, an asymmetric electronic environment is created by partially patterning the large area monolayer CVD grown graphene between the source and drain. This results in the generation of a high temperature gradient that surpasses the theoretical limit set by the intrinsic Seebeck coefficient of graphene. Along with the temperature rise from intrinsic intraband hot carrier generation in graphene, the plasmon-assisted hot carriers in the patterned section further enhances the effective temperature gradient (ΔT) across the source-drain contacts. The different carrier mobilities of the patterned and unpatterned sections of the channel lead to differential Joule heating during carrier transport, which accentuates the thermal gradient in the system. Interestingly, due to the electrostatic tunability of the graphene dielectric function, ΔT and as a result the photo-thermoelectric voltage are gate-controllable. The presented detector design and choice of constituent materials favor direct integration with the matured silicon-based readout integrated circuit (ROIC), unlike other schemes involving polymers or materials that need heterojunction epitaxial growth on specific substrates for operability. These results outline a novel

strategy for uncooled, tunable and multispectral infrared detection based on practical CVD grown large area graphene sheets.

In Chapter 5, I study the surface plasmon excitation in the noble three-dimensional material like gold and introduce an interesting application for the surface plasmon called light funneling. Diffraction does not allow light to bend through an aperture on an opaque film if the aperture dimension is subwavelength. This can be shown through diffraction analysis that constructive interference in the forward direction cannot take place for an aperture whose dimension is less than the wavelength of the incident light [127]. However, the situation changes if the incident light excites surface plasmon on the patterned film. The reduction in effective plasmon wavelength, the coupling between plasmons on both sides of the film and re-radiation of oscillating electrons at resonance enables tunneling of the photon through the subwavelength opaque aperture – called extraordinary light transmission [83, 91, 128-140]. Such extraordinary transmission has been widely studied in the context of single apertures [83, 91, 138, 140] as well as array [129-131, 133-137, 139] in various shapes and geometry. The phenomenon solely depends on dielectric properties of the metal, aperture dimensions and periodicity which affects the transmission through near-field and far-field couplings [128, 130-132, 134, 136-140].

In this chapter, I present a resonant cavity-assisted light funneling through sub-wavelength complimentary hole/disk array in a wavelength regime far away from the natural plasmon resonance of the metallic array in the 3-5 μm band, resulting in 100% absorption of the incident photon over a narrow bandwidth. The fundamental light-funneling and the subsequent perfect absorption processes originate from the excitation of hybrid localized surface plasmon (hLSP) modes consist of spoof and regular plasmons which are indistinguishable from one another due to the spatial and temporal overlap. Moreover, simple nanoimprint lithography based large area

fabrication process makes this a practical platform for narrowband plasmonic cavity-based devices and sensors. For a given metal and aperture dimension, the absorption band of which is widely tunable across a wide spectral range with the cavity phase.

This approach demonstrates a unique cavity phase driven light funneling through a subwavelength complementary aperture pair where previously observed funneling is not possible due to the absence of natural plasmon resonance at that wavelength range. The cavity phase driven tunable photon capture opens up a new way of enhancing light-matter interactions for practical applications like frequency-selective infrared detection, bio-sensing and light harvesting.

In Chapter 6, I show a novel application of lossy plasmons as a mechanism of “color” sensing in infrared frequency domain by virtue of bolometric principle. I propose quasi 3D plasmonic crystal consisting of vertically-separated complementary nanohole and nanodisk arrays coupled to an optical cavity. The general behavior of this complex system is determined by the interaction of optical cavity modes, hybrid plasmonic excitation on the disk array and vertical/horizontal coupling of the metallic dipolar elements. The geometric nature of this plasmonic crystal “funnels” the light through the subwavelength holes coupled to the disk array by exciting hybrid plasmon, which is dissipated in the form of resistive loss resulting from induced micro-currents on the edge of dipole elements (holes and disks). Surface patterning with a superlattice to sense the power dissipation with external biasing circuitry show promising results with very high spectral selectivity and response time. A 3 dB response time of 100 μ s is measured, which outperforms present microbolometer’s typical response time of 10-15 ms. The frequency selective infrared absorption spectroscopy has proven to be a very important tool in the detection and identification of airborne chemicals by comparing infrared light absorption in presence and

absence of airborne contaminants. The geometrical tunability and narrow bandwidth of the light absorption not only determines the contaminants, but also their concentration.

Detection of mid infrared photons is scientifically challenging and expensive process due to the cryogenic cooling requirement. The proposed metasurface bolometer possesses inherent frequency selective detection capability by simple dimensional changes paving the path towards low cost room temperature mid-infrared “color” photon detection with high signal to noise ratio ($D^* \sim 10^8 - 10^9 \text{ cm} \cdot \sqrt{\text{Hz}} / \text{W}$) when packaged into a commercial detector architecture. In this chapter I theoretically and experimentally demonstrate a “light funnel” to collect and detect multi-color photons with high degree of frequency selectivity and detection sensitivity. The proposed concept attempts to address both efficient photon collection as well as tunable frequency selective detection limitations of present infrared detectors.

Finally, Chapter 7 contains another usage of the surface plasmon called focusing effect. For conventional refractive lenses index contrast is small which means that the thicknesses of these dielectric optical components need to be much larger than the wavelength of incoming light to accumulate 0 to π phase shift. That means subwavelength compact planar geometry is not possible in conventional lenses making optical systems bulky. Further, conventional lenses are limited by optical aberrations (e.g. spherical and chromatic) and diffraction limit. Abbe-Rayleigh diffraction limit is a natural obstacle in conventional optical lenses due to the far-field interference and absence of near-field. Various, planar lenses are demonstrated following diffractive optics concept of phase control based on dielectric scatterers on a 2D plane. However, in the mid-infrared wavelength range (3-16 μm) such engineered dielectric surfaces are not possible due to the lack of optically transparent materials with high index contrast.

Plasmonic nanoantennas enable abrupt change in phase, amplitude and polarization of the incident light using subwavelength optical nanoantenna on a planar surface. Such control of phase according to the Huygens principle allows formation of arbitrary wavefront shapes enabling subwavelength focusing. In this chapter, I propose theoretically and experimentally an ultrathin flat lens working in the mid-IR spectral range with geometrically tunable focal length and sub-diffraction focusing ability. The transmission efficiency of this flat lens is substantially higher compared to other reported plasmonic lenses due to the low metallic fill-fraction and the geometry. The biggest limitation of dielectric as well as metallic flat lenses is bandwidth of operation due to the inherent narrowband resonance. Previously, reported plasmonic flat lens are limited to narrow operation bandwidth in the infrared spectral range. None of these works reported the most critical lens parameter transmission efficiency. The proposed lens in contrast offers wide bandwidth and relatively low loss due to its gradient design and low metallic fill-fraction. For the optimum design the experimentally measured transmission remained $> 60\%$ over the entire $4 - 10 \mu\text{m}$ mid-IR spectral range which promises further improvement in broadband transmission efficiency with improved fabrication procedures. Single (polarization dependent) and bi-layer (polarization independent) designs enable polarization degree of freedom as well as tunable line and point focusing, respectively. Further, such geometry defined tunable optical response overcomes the challenges associated with the unavailability of mid-infrared transparent materials for low footprint planar integration with thermal imaging systems.

CHAPTER 2: ENHANCED LIGHT-GRAPHENE INTERACTION

Published at <https://journals.aps.org/prb/abstract/10.1103/PhysRevB.96.165431> on 17 October 2017 by Physical Review B . DOI: <https://doi.org/10.1103/PhysRevB.96.165431>, Alireza Safaei, Sayan Chandra, Abraham Vázquez-Guardado, Jean Calderon, Daniel Franklin, Laurene Tetard, Lei Zhai, Michael N. Leuenberger, and Debashis Chanda

Introduction

Graphene, one of the widely studied two dimensional materials, possesses a very high carrier mobility and a fast carrier relaxation time [74, 75, 141-143], making it an attractive candidate for ultrafast electronics and optoelectronic devices such as transistors [144], optical switches [16, 22, 145], mid-infrared (MIR) photodetectors [33, 146], photovoltaic devices [147], ultrafast lasers [148], *etc.* The performance of such devices critically depends on the extent of light-matter interaction in graphene, which is limited due to its low optical absorption ($< 2.5\%$) in the visible to IR wavelength range. Graphene absorption is low across the wide optical wavelength range. In the visible wavelength range, the light absorption in graphene is $\sim 2.3\%$ [76, 149], in near-infrared (NIR) is $< 2\%$, in MIR $< 3\%$ [149] and in far-infrared range $< 10\%$ [150]. In nanostructures, light waves propagating at a metal-dielectric interface can excite collective modes of electrons at the metal surface, resulting in the generation of charge density waves called surface plasmons. There are two types of surface plasmon modes, localized surface plasmons and surface plasmon polaritons, propagating along the interface with an effective wavelength much less than that of incident light [151]. Recent studies primarily focused on three approaches to enhance light absorption in mono-layer graphene: (i) excitation of surface plasmons on patterned graphene [39,

47, 48, 50, 152], (ii) plasmonic light focusing on graphene using metal patterns, as a means to increase absorption of light [16, 22, 153, 154], and (iii) cavity-induced absorption enhancement. In the first category graphene nanoresonator arrays show a mere $< 12\%$ absorption in the $8 - 12 \mu\text{m}$ band [39, 48]. In category two, indirect enhancement methods based on plasmonic effects are employed, where some type of metal pattern is used to enhance the light-graphene interactions [16, 20, 22, 155-157]. In these approaches the majority of the energy is dissipated as metallic loss [158], which defeats its purpose. In category three theoretically, it has been predicted that coupling of patterned graphene with an optical cavity can improve absorption to more than 90% [27, 159]. However, the maximum absorption value reported for cavity coupled graphene film was $\sim 30\%$ at $\lambda = 1.5 \mu\text{m}$ [39], $\sim 24\%$ absorption in the $5 - 7 \mu\text{m}$ wavelength range [152] and less than 20% [49] at $\lambda \sim 8 \mu\text{m}$ for isolated graphene nanodisks, which cannot be used for practical applications due to lack of electrical continuity. Enhanced tunable absorption on electrically continuous mono-layer graphene is still a scientific challenge.

In this chapter, I demonstrate a direct enhancement method based on cavity-coupled patterned mono-layer graphene whereby the Fermi energy (E_F) is tuned by an external gate voltage, leading to a predicted maximum absorption of 60% in the $8-12 \mu\text{m}$ band and a dynamic tunability of up to $2 \mu\text{m}$. For the present demonstration we chose the atmospherically transparent $8-12 \mu\text{m}$ band, since it is essential for infrared thermal imaging and there is a lack of low bandgap absorbers. This 60% absorption can only be achieved if the combined absorption of surrounding layers is $< 40\%$. However, the ion-gel and the SU-8 polymer films which I used as gate dielectric and cavity spacer layers, respectively, absorb $> 50\%$ amount of the incident light. In order to reduce their absorption to around 45% at $\lambda=10 \mu\text{m}$, the cavity thickness needs to be decreased to $L = 1.1 \mu\text{m}$. Henceforth, I report the experimentally measured absorption of 45% in the patterned graphene

($A=1-R$) with respect to the absorption of the structure without graphene as the reference. Remarkably, I achieve a more than 100% improvement in absorption along with a large gate voltage controlled spectral tunability of up to $\sim 2 \mu\text{m}$ [152]. This is attributed to the strong coupling between localized surface plasmon resonances (LSPR) on patterned graphene and the optical cavity modes, the operating band of which is defined by the pattern and cavity dimensions. Surface plasmon couples the incident electromagnetic wave (far-field) to the surface wave (near-field). This means the amplitude of the excitation field determines the amount of near-field enhancement [6, 151, 160, 161]. The cavity geometry based on the cavity thickness enhances the excitation field on the patterned graphene due to the constructive interference between the incident field and back reflected field which in turn enhances the LSP on the patterned graphene [6, 151, 160, 161]. The LSPs in the patterned graphene sheet are edge plasmons that are localized at the edge of each hole [162-164]. The proposed design offers distinct advantages over previous studies. Firstly, this coupled system is more tolerant to the low carrier mobility of CVD graphene, which is evident from the nominal decrease in absorption from 45% for carrier mobility of $960 \text{ cm}^2/\text{V}\cdot\text{s}$ to 31%, as the carrier mobility decreases to $250 \text{ cm}^2/\text{V}\cdot\text{s}$. Secondly, the feature sizes of nanostructures in this design are much larger than the previous nanoribbon/disk designs [49, 50], which reduces fabrication challenges for practical implementation. Finally, the nanoimprinting based large area low cost patterning makes this approach suitable for both enhanced absorption and optoelectronic applications [1, 2, 8, 11, 165, 166].

Theoretical model

Nanostructure Design

An array of nanoholes on graphene conserves the continuity of graphene, and by coupling this perforated graphene to an optical cavity, I show that it is possible to achieve constructive interference between the incident and scattered electric fields, giving rise to strong enhancement of the absorption. Consequently, the strong light-matter interaction amplifies direct light absorption in graphene even in conditions of low carrier mobility, unlike other techniques [39, 47, 48, 50, 152] where high carrier mobility is required for absorption enhancement. The system consists of a dielectric slab of thickness L and refractive index $n_d = 1.56$ sandwiched between patterned graphene and an optically thick (200 nm) gold back reflector, as illustrated in Figure 2: Extraordinary absorption in cavity-coupled nanomesh graphene and the effect of carrier mobility on absorption enhancement. a-right (inset). The patterned graphene is obtained by perforating a square array of holes with 330 nm diameter and 400 nm period. A simple embossing based nanoimprinting technique [161, 167] was followed to pattern the graphene sheet. The cavity supports transverse electromagnetic modes when the slab thickness satisfies the phase equation $L = m\lambda/4n_{eff}$, where n_{eff} is the effective refractive index of the dielectric slab, λ is the incident electromagnetic wavelength, and $m = [1,2,3,\dots]$ is the m -th order of the optical cavity mode. The n_{eff} value, which includes the effect of patterned graphene is calculated by the effective medium approach [6, 168, 169].

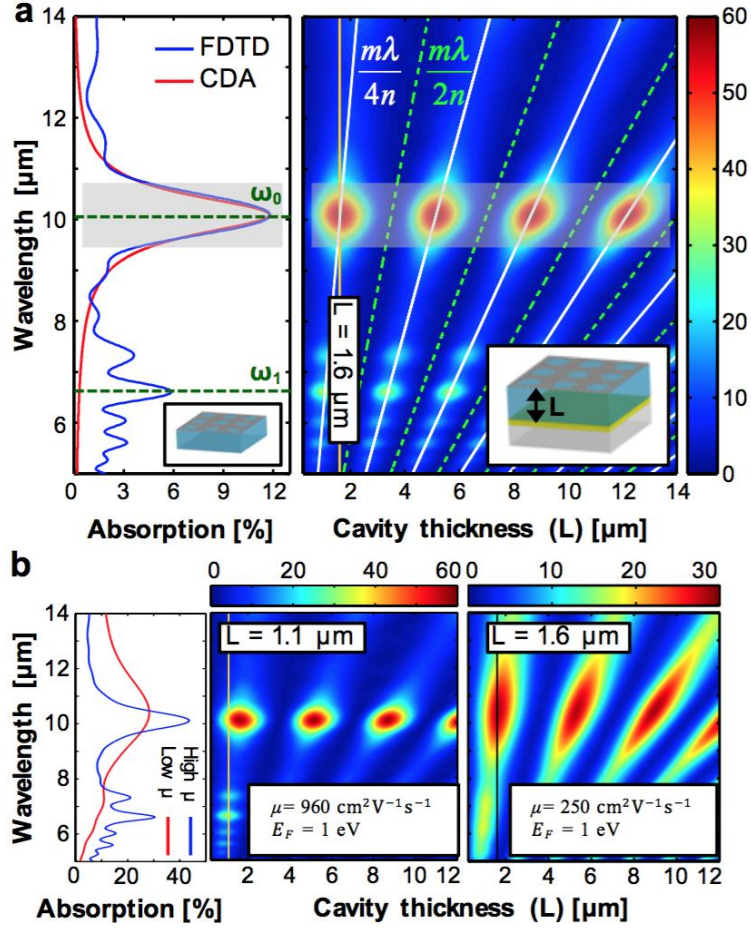


Figure 2: Extraordinary absorption in cavity-coupled nanomesh graphene and the effect of carrier mobility on absorption enhancement.

(a) (left) FDTD and CDA predicted absorption of the patterned graphene. (right) FDTD prediction of absorption as a function of cavity thicknesses for the cavity-coupled case. The white solid and green dotted lines represent constructive and destructive cavity modes respectively. (b) FDTD predicted cavity length and wavelength dependent absorption for high (middle) and low mobility (right). The corresponding wavelength dependent absorption for two cavity thicknesses are shown in (left).

The finite-difference time domain (FDTD) simulations (with auto shutoff min of 10^{-8} , simulation time of 5000 fs and meshing of 0.05 nm) reveal that for odd/even cavity modes excited with x-polarized light, the incident and reflected electric fields interfere constructively/destructively giving rise to a maximum/minimum value in the surface plasmon enhanced absorption for

graphene with electron mobility of $\mu = 960 \text{ cm}^2/\text{V}\cdot\text{s}$ and Fermi energy of $E_F = 1.0 \text{ eV}$ (Figure 2a-right). In the case of destructive interference, the incident and reflected electric fields have a phase difference of π such that their interference results in zero net amplitude [6, 151, 160]. The FDTD absorption spectrum (Figure 2a-left) shows two distinct peaks at ω_0 and ω_1 , which can be attributed to LSP and SPP modes, respectively. This is evident from the corresponding real $[\text{Re}(E_z)]$ part and intensity ($|E_z|^2$) of the z-component of the electric field distribution for both plasmonic modes, as shown in Figure 3. The nature of the plasmonic mode at ω_0 is further confirmed to be a LSP because of the close correspondence between the FDTD and coupled dipole approximation (CDA) [46, 169] modelled absorption spectra of the patterned graphene without optical cavity (Figure 2a-left) [54].

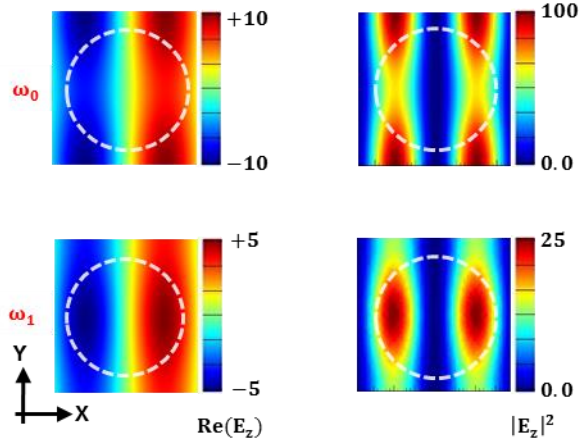


Figure 3: Near-field distribution.

The real part and the intensity of electric field distribution in z-direction derived from FDTD for different plasmonic modes. The white circle line shows the graphene edges.

Due to the symmetrical square lattice pattern of the holes, the excitation of LSP is independent

of light polarization for normal angle of incidence. The solid white and green dotted lines in the FDTD calculation in Figure 2a-right show the analytical dispersions of the cavity modes as a function of wavelength and cavity thickness, which accurately depicts the origin of this extraordinary absorption arising from the temporal and spatial overlap between the LSP resonance and the cavity modes. The FDTD simulation shows that a cavity length of $L = 1.6 \mu\text{m}$, which satisfies the cavity resonance condition, needs to be chosen in order to achieve $\sim 60\%$ light absorption in patterned graphene at around $\lambda = 10 \mu\text{m}$, giving rise to about a 30-fold absorption enhancement compared to pristine graphene. I use the optical cavity to strongly increase the absorption of the incident light by means of the enhancement of the electric field on the patterned graphene. The bare pattern graphene absorbs $\sim 12\%$ of the incident light (Figure 2a) which is theoretically and experimentally enhanced to $\sim 60\%$ and $\sim 45\%$ for specific cavity lengths at $\lambda = 10 \mu\text{m}$, respectively. A comparison between the uncoupled and the cavity-coupled systems (Figure 2a-left and right) shows an increase in absorption from 12% to 60%, without change in the LSP resonance frequency for all cavity modes.

The Parameters of FDTD Simulation

The FDTD simulation time was set to 5000 fs, the “auto shut-off time”, which defines the convergence as 10^{-8} (this is very small compared to typical simulations for 3D nanostructures (10^5)). The monolayer graphene sheet in FDTD simulation is considered as a bulk material with thickness of 0.5 nm [36, 44]. This means the simulation always completely converges. Moreover, the periodic boundary condition ensures better convergence. To show the effect of “auto shut-off time” on the results, the absorption of patterned graphene for different “auto shut-off times” are overlaid in Figure 4. For all these plots the ripples are present, which means that the ripples are not artifacts of the FDTD simulation. The simulation for shorter time steps and the results were

same. These ripples are the different modes emerging at lower wavelengths because of diffraction of surface EM waves.

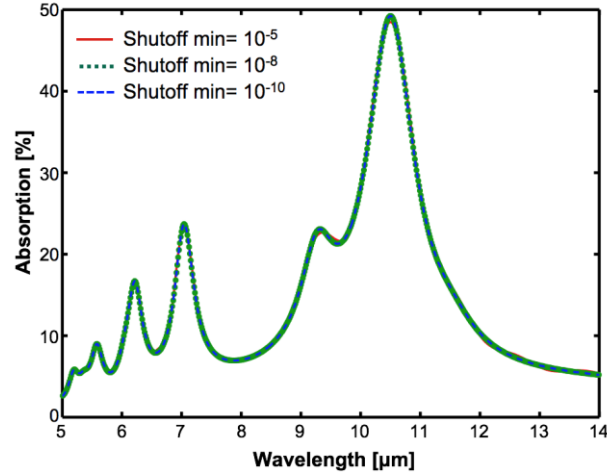


Figure 4: Simulation convergence.

The light absorption of cavity coupled patterned graphene with cavity thickness of $L = 1400 \text{ nm}$, Period=400 nm, Diameter=330 nm, $E_f = 1.0 \text{ eV}$ and $\mu = 960 \text{ cm}^2/\text{V.s}$ for different auto shutoff mins.

Diffraction of the Surface Plasmons

There is no diffraction for the incident light because the period of the pattern is less than the wavelength of the incident light. But, the wavelength of the propagating surface wave is much less than that of free space, resulting in diffractions that are seen as ripples. For graphene in an asymmetric dielectric medium, the plasmon wavenumber (k_p) can be calculated by means of

$$\frac{\epsilon_1}{q_{z1}} + \frac{\epsilon_2}{q_{z2}} + 2\sigma^{\text{intr}}(\omega) = 0, \quad (2)$$

where ε_1 and ε_2 are dielectric functions of adjacent environments, $q_{z1,2} = \sqrt{\varepsilon_{1,2} - (k_p/k)^2}$ and k is the wavenumber of incident EM wave [38, 170]. The plasmon diffraction orders correspond to the solutions of Equation. (2) [45], which leads to different peaks at lower wavelengths.

Coupled Dipole Approximation

For analytical calculation of the optical extinction of the perforated graphene in the long wavelength limit, each element is considered as an electric dipole in the electrostatic limit with a specific polarizability $\alpha(\omega)$. The polarizability of a generalized ellipsoidal nanoparticle is [46, 171]

$$\alpha(\omega) = \varepsilon_0 V \frac{\varepsilon - \varepsilon_m}{\varepsilon + L_e (\varepsilon - \varepsilon_m)}, \quad (3)$$

where ε and ε_m are the dielectric functions of the conductive element and surrounding medium, respectively. The parameter V defines the volume, and the shape factor of the ellipsoid, L_e , is given by

$$L_e = \frac{abc}{2} \int_0^\infty \frac{dq}{(a^2 + q) \left\{ (q + a^2)(q + b^2)(q + c^2) \right\}^{\frac{1}{2}}}, \quad (4)$$

where a is the diameter of the ellipsoid along the light polarization direction, b and c are the diameters along the other two dimensions. For the graphene disk array, $a = b = d$, where d is the disk diameter and $c = t$, where t is the thickness of graphene. To calculate the light absorption of perforated graphene, the light reflection/transmission of graphene disk array is used as light transmission/reflection of graphene hole array. This is an approximation to calculate the optical responsivity of perforated metal by CDA approach. Derivation of the LSP frequency is possible by calculation of the total electric potential in presence of two-dimensional nanostructure elements.

The total electric potential in space is due to the combination of the radiation of the graphene nanostructure and the external electric field, *i.e.*

$$\Phi(\mathbf{r}) = \Phi^{ext}(\mathbf{r}) - \frac{i}{\omega} \int_0^d \int_0^{2\pi} \frac{d^2 \mathbf{r}' \cdot \nabla' \cdot \sigma(\mathbf{r}', \omega) \nabla' \Phi(\mathbf{r}')}{|\mathbf{r} - \mathbf{r}'|}. \quad (5)$$

By considering homogeneous doping of graphene, it can be assumed that the conductivity does not depend on position, and outside graphene the conductivity goes to zero. It means that $\sigma(\mathbf{r}, \omega) = F(\mathbf{r})\sigma(\omega)$, where $F(\mathbf{r}) = 1/0$ for inside/outside graphene. By defining a dimensionless variable $\mathfrak{R} = \frac{r}{d}$, the electric potential is given by

$$\Phi(\mathbf{r}) = \Phi^{ext}(\mathbf{r}) + \eta \int_0^1 \int_0^{2\pi} \frac{d^2 \mathfrak{R}' \cdot \nabla' \cdot F(\mathfrak{R}') \nabla' \Phi(\mathfrak{R}')}{|\mathfrak{R} - \mathfrak{R}'|}, \quad (6)$$

where

$$\eta = \frac{e^2 E_F}{\pi \hbar^2 \varepsilon_m d} \frac{1}{\omega(\omega + i\tau^{-1})}. \quad (7)$$

Equation. (6) introduces a self-consistent potential that in absence of external potential has real eigenvalues related to the plasmonic modes. The LSP frequency is given by [50]

$$\omega_p = \frac{e}{\hbar} \sqrt{\frac{\mathfrak{S} E_F}{\pi \varepsilon_m d}} - \frac{i}{2\tau}, \quad (8)$$

where \mathfrak{S} is the eigenvalue of Equation. (6) and can be derived by solving this eigensystem or by using the results from the FDTD simulation. The imaginary part of ω_p is responsible for the bandwidth of the absorption peak. In addition, Equation. (8) can be applied for the graphene nanoribbon by replacing d (diameter) with w (nanoribbon width) [44].

The lattice contribution S describes the near field and far field coupling of the electric dipoles [172]

$$S = \sum_{j \neq i} \left[\frac{(1 - ikr_{ij})(3 \cos^2 \theta_{ij} - 1)e^{ikr_{ij}}}{r_{ij}^3} + \frac{k^2 \sin^2 \theta_{ij} e^{ikr_{ij}}}{r_{ij}} \right], \quad (9)$$

where r_{ij} is the distance between electric dipoles i and j , θ_{ij} is the angle between dipole j and \mathbf{r}_{ij} , and $k = \omega/c$ defines the wavenumber.

The optical reflection coefficient of the disk array can be calculated by using the polarizability and the lattice contribution [46]

$$r_{disk} = \frac{\pm i \Xi}{\alpha^{-1} - S}, \quad (10)$$

where

$$\Xi = \frac{2\pi k}{A} \begin{cases} (\cos \vartheta)^{-1}, s - polarization \\ \cos \vartheta, p - polarization \end{cases}, \quad (11)$$

and ϑ is the incident angle, which is zero in my study, A is the area of the unit cell, and positive/negative sign stands for s/p polarization. The transmission coefficient of the disk array can be obtained through $t_{disk} = 1 + r_{disk}$.

The Effect of Carrier Mobility

The absorption enhancement further depends on the electron mobility [173] and Fermi energy of graphene [35, 37, 48, 152, 157], which in turn is affected by the choice of dielectric material, substrate, and gate bias. It is well known that graphene on a polymer substrate has a low carrier mobility [143, 174] ($< 1000 \text{ cm}^2/\text{V.s}$) because of extra scattering processes. Typical scattering centers consist of charge impurities, polymers residues, and coupling centers between

graphene electrons and polar or non-polar optical phonons of the polymer matrix [173, 175, 176]. To study the impact of the reduced carrier mobility of patterned graphene on its absorption spectra, I performed FDTD simulations for two different carrier mobilities (μ) of 960 cm²/V.s and 250 cm²/V.s, while maintaining the same E_F for the cavity-coupled system. In the FDTD simulations, the real and imaginary parts of graphene's refractive index (n,k) were calculated from the carrier mobility using the random phase approximation (RPA). In RPA, for high frequencies the complex graphene conductivity is given by [74, 75, 142]

$$\sigma(\omega) = \frac{e^2 \omega}{i\pi\hbar^2} \left[\int_{-\infty}^{+\infty} d\varepsilon \frac{|\varepsilon|}{\omega(\omega+i\tau^{-1})} \frac{d\rho_F(\varepsilon)}{d\varepsilon} - \int_{-\infty}^{+\infty} d\varepsilon \frac{\rho_F(-\varepsilon) - \rho_F(\varepsilon)}{(\omega+i\delta)^2 - 4\varepsilon^2} \right], \quad (12)$$

where $\delta \rightarrow 0$ is the infinitesimal parameter that is used to bypass the poles of the integral. The first and second terms correspond to the intraband electron-photon scattering processes and direct electron interband transitions, respectively. By performing the first integral, the intraband scattering is found to be similar to the Drude conductivity at low temperature $k_B T \ll E_F$ [142]

$$\sigma^{\text{intra}}(\omega) \approx i \frac{e^2 E_F}{\pi\hbar^2 (\omega + i\tau^{-1})}, \quad (13)$$

where k_B is the Boltzmann constant and T is the temperature. At high EM wave frequencies in the visible domain $\hbar\omega \gg (E_F, k_B T)$, where E_F is the Fermi energy with respect to the charge neutrality point (CNP) of the Dirac cone, interband transitions dominate and the light absorbance of graphene is $A = \pi\alpha \approx 2.3\%$, which is independent of wavelength ($\alpha \approx 1/137$ is the fine structure constant) [74]. However, in the mid-IR frequency range and for high Fermi energy $E_F \gg \hbar\omega$, graphene's optical response is dominated by intraband transitions and the conductivity (σ) follows the Drude-Lorentz model [74, 75, 142], i.e. Equation. (13), where τ is the relaxation time determined by impurity scattering (τ_{imp}) and electron-phonon ($\tau_{\text{el-ph}}$) interaction time as

$\tau^{-1} = \tau_{imp}^{-1} + \tau_{el-ph}^{-1}$. According to the charge conservation law, the relation of the bulk current J_V and the surface current J_S for a material is given by [177]

$$\iint J_S ds = \iiint J_V dV, \quad (14)$$

which means the relation of two- and three-dimensional conductivity is defined by

$$\sigma_{3D} = \frac{\sigma_{2D}}{t}, \quad (15)$$

where t describes the thickness of the material. The dielectric function of graphene can be obtained via its AC conductivity by means of [178]

$$\varepsilon(\omega) = \varepsilon_g + \frac{i\sigma_{3D}}{\varepsilon_0\omega}, \quad (16)$$

where $\varepsilon_g = 2.5$ is the dielectric constant of graphite. Substituting Equation. (15) into Eq. (16) gives the in-plane dielectric function of graphene, i.e.

$$\varepsilon(\omega) = \varepsilon_g + \frac{i\sigma^{int ra}}{\varepsilon_0\omega t} = \varepsilon_g - \frac{e^2 E_F}{\varepsilon_0 \pi \hbar^2 \omega(\omega + i\tau^{-1})t}, \quad (17)$$

whereas the surface-normal component is $\varepsilon_z = 2.5$. The $\varepsilon(\omega)$ values calculated using Equation. (17) were used to obtain the (n,k) values for the FDTD simulations performed for different Fermi energies.

Figure 2b-left shows a nominal decrease in the peak absorption from 45% to 31% as the electron mobility is decreased. For a relatively high carrier mobility (960 cm²/V.s) loss is small and therefore the bandwidth of the absorption spectrum is narrow, indicating an increased lifetime of plasmons, as observed in Figures. 2b-middle and 2b-left (blue) for a cavity thickness of $L = 1.1$ μm (this cavity thickness is chosen to show nearby high frequency weaker resonances). Higher

loss in lower carrier mobility graphene gives rise to reduced plasmon lifetime and broadening of absorption spectrum, as shown in Figures. 2b-right and 2b-left (red). The results from the FDTD simulations demonstrate that my device architecture can induce considerable absorption for low mobility graphene, which is a significant improvement over previously strategized devices that are functional only for high mobility graphene [39, 47-50].

Fabrication and experimental results

To experimentally verify the results, the cavity-coupled patterned graphene device was fabricated based on the schematic presented in Figure 5a. Large area CVD grown graphene was transferred on the substrate, and it was verified to be a monolayer by performing Raman characterization, as shown in Figure 5b. Figure 5c shows the scanning electron microscope (SEM) image of a nanoimprinted-patterned graphene showing good uniformity in nanohole diameter across the patterned film. Furthermore, the graphene continuity and nano-pattern formation was confirmed by conductive atomic force microscopy (AFM), which shows the difference in conductivity in the holes of the patterned graphene with respect to the surrounding (Figure 5d).

Device Fabrication Process

The graphene sheet is grown on a 25 μm thick copper foil in an oven composed of a molten silica tube heated in a split tube furnace. The molten silica tube and copper foil are loaded inside the furnace, evacuated, back filled with hydrogen, and heated up to 1000 °C while keeping a 50 sccm H_2 stream. The subsequent steps include reinstating the copper foil at 1000 °C for 30 minutes, inserting 80 sccm of CH_4 for 30 minutes. Then the furnace is cooled down to room temperature without gas feeding. An optically thick layer of Cr/Au (4 nm / 200 nm) is deposited on a glass substrate as a back reflector using e-beam deposition. A photoresist (SU-8) layer is spin-coated on

the gold back reflector to form an optical cavity, that is cured under UV lamp for 2 hours and baked on a hot plate for 1 hour at 95 °C in order to complete the cross-linking process. A thin layer (~20 nm) of Gold-Palladium (Au-Pd) is sputtered on the dielectric spacer which function as a gate electrode.

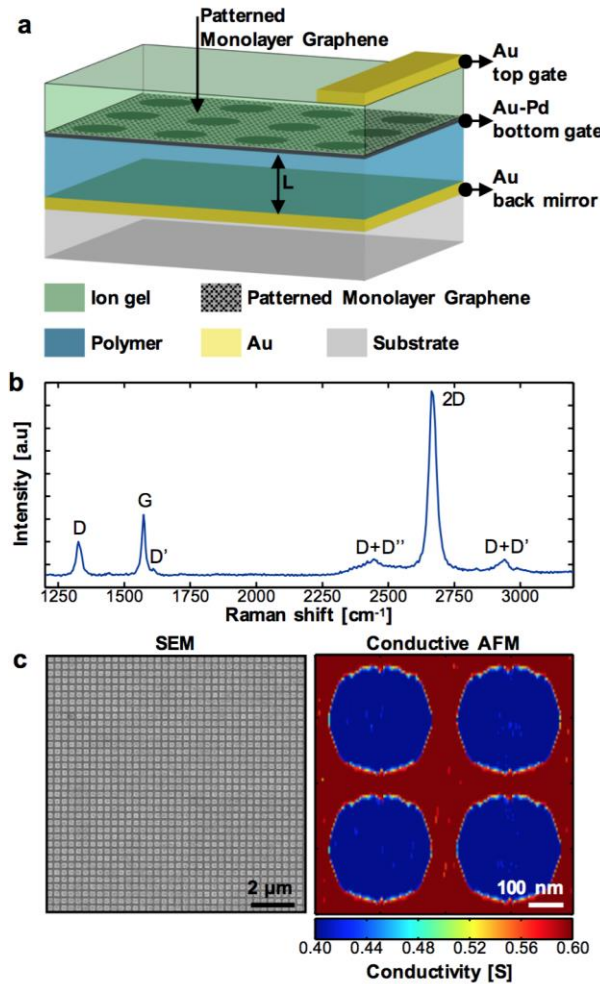


Figure 5: Fabricated system and characterizations.

(a) Schematic of the cavity-coupled patterned graphene. (b) The Raman spectrum of grown pristine graphene. The presence of sharp and strong 2D peak proves mono-layer graphene. (c) SEM image of the fabricated patterned graphene on dielectric slab (left) and Conductive AFM image of patterned graphene on copper foil (right).

A CVD-grown graphene sheet is transferred onto the Au-Pd layer using a PMMA transfer layer which is subsequently dissolved in Acetone. The square lattice hole pattern is fabricated following a simple large area nanoimprinting technique [161, 167]. A poly dimethylsiloxane (PDMS) stamp is embossed against a thin photoresist (SU-8) layer that is spun coated on the graphene layer, followed by reactive ion etcher (RIE) in order to perforate the graphene layer. Low carrier mobility nanomesh graphene is prepared by rinsing the residual polymers (PMMA and SU-8) in acetone one time for a few seconds. In contrast, the high carrier mobility sample is prepared by repeating this process for more than ten times in order to reduce polymer residues from the perforated graphene. A high capacitance ion gel film with refractive index of 1.3 [179] is drop-casted on graphene in order to tune its Fermi energy to high values ($\sim 1\text{eV}$). Ion gel is a printable gate dielectric polymer [49, 180] made by mixing ionic liquid ([EMIM][TFSI]) (Sigma-Aldrich, Inc.) with dry PS-PEO-PS (10-44-10 kg/mol) triblock copolymer (Polymer Source, Inc.) with ratio 1:0.04 in a dry solvent (dichloromethane) (Sigma-Aldrich, Inc.) and by stirring the mixture overnight. Then it is left for 48 hours inside high vacuum chamber (pressure $< 10^{-6}$ torr) in order to evaporate the remaining solvent. The materials are dried in high vacuum for 24 hours then transferred to the glovebox for 4 days. The gate is fabricated by depositing Cr/Au (3 nm / 40 nm) on Si substrate. A copper wire is connected to the gate by applying silver paste on the side and back. The resulting substrate is flipped upside down and put on top of the ion gel.

Gate Dielectric

I used ion gel as the dielectric layer to electrostatically dope patterned graphene. The measured capacitance of the ion gel layer is $C = 2.4 \mu\text{F}/\text{cm}^2$ and its absorption in mid-IR spectrum is low. The Fermi energy of graphene is given by $E_F = \hbar v_F (\pi\rho)^{1/2}$, where $v_F \simeq 10^6 \text{ m/s}$ is the

Fermi velocity and n is the electron/hole density obtained from $\rho = C\Delta V/e$, where ΔV is gate voltage relative to CNP. The reported Fermi energies are calculated based on this relation. To estimate the corresponding Fermi energies experimentally, the conductivity of graphene sheet is calculated based on $\sigma(E_F) = \sigma_{min}(1 + E_F^4/\Delta^4)^{1/2}$, where σ_{min} is the minimum conductivity and Δ is the disorder strength parameter. As shown in Figures 6a and 6b, by fitting this conductivity to the experimental data (red dotted line), $\sigma_{min} = 0.289 \text{ ms}/0.371 \text{ ms}$ and $\Delta = 297 \text{ meV}/177 \text{ meV}$ are obtained for the diagram shown in Figures 6a/6b.

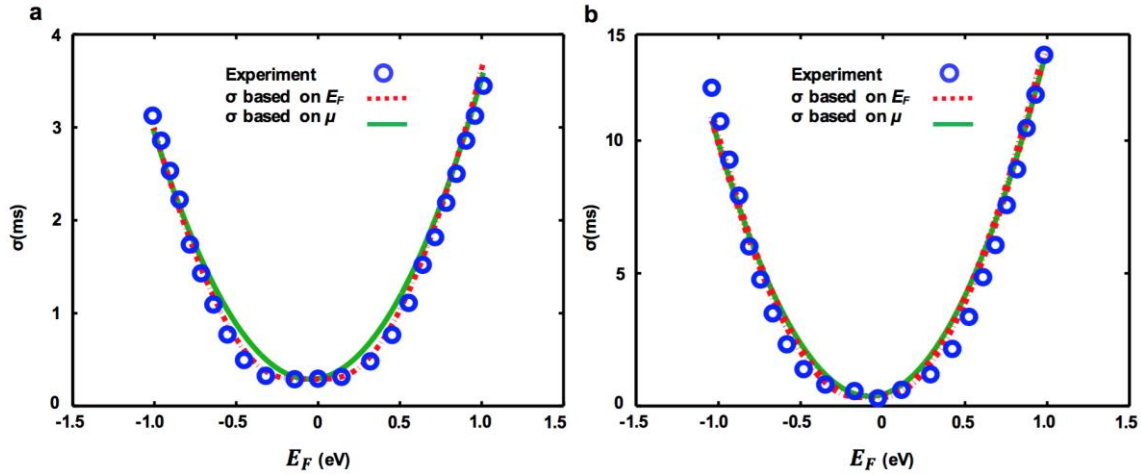


Figure 6: Carrier mobility measurement.

(a)-(b) Electrical conductivities of monolayer graphene sheets with different carrier mobilities. Experimental results and analytical calculations for (a) $\mu = 250 \text{ cm}^2/\text{V.s}$ and (b) $\mu = 960 \text{ cm}^2/\text{V.s}$ show the dependence of electrical conductivity on Fermi energy. The dotted red diagram is the electrical conductivity by $\sigma(E_F) = \sigma_{min}(1 + E_F^4/\Delta^4)^{1/2}$ and the solid green diagram demonstrates $\sigma = \rho e \mu$.

The relation between conductivity and mobility is $\sigma = \rho e \mu$, where μ is the carrier mobility of graphene. Fitting this equation (green solid line) to the experimental results yields $\mu = 250/960 \text{ cm}^2/\text{V.s}$ for Figures 6a/6b. Positive and negative gate voltages correspond to n-doped

and p-doped graphene, with a minimum conductivity occurring at the CNP. According to this analysis we find that the CVD graphene sheet is p-doped during growth and transfer (~ 0.05 eV).

Light Absorption Measurement

For graphene absorption measurement, I followed a well-known technique to experimentally measure the reflection spectra of thin films and 2D materials [6, 39, 48-50, 152, 160, 161, 167, 181, 182]. In the experimental measurement with FTIR, I took the reflection spectrum of the structure with unpatterned graphene as the reference such that the FTIR calibrates the spectrum as $R=|r|^2=1$ in the entire wavelength range. Following this, the reflection spectrum (R) of the structure with patterned graphene is measured with respect to the reference. Due to the presence of the back mirror, the transmission (T) is zero and hence absorption (A) = $1-R-T=1-R$. This directly yields the absorption measurements shown in Figures 7 and 8 which closely matches with the FDTD predicted absorption spectra.

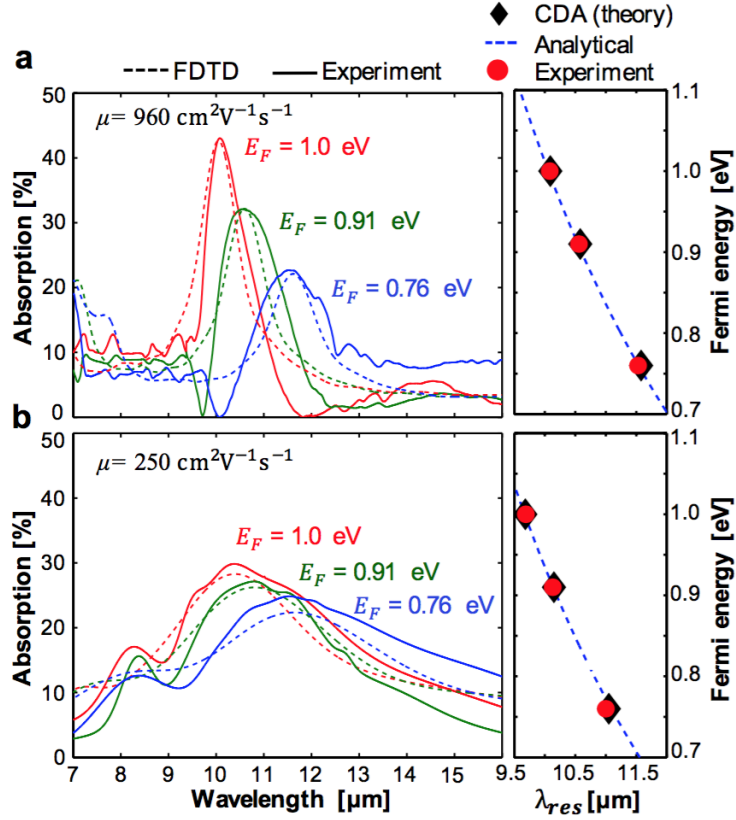


Figure 7: Fabricated system and dynamic tunable response.

Experimentally measured (solid) and theoretically predicted (dashed) mobility dependent tunable absorption spectra for a high (a) ($L=1.1 \mu\text{m}$) and low (b) ($L=1.6 \mu\text{m}$) mobility mono-layer patterned graphene. Right figures showing the comparison of experimental, CDA and theoretical results. Theoretical graphene plasmon frequency follows $\omega_p \propto \sqrt{E_F} \propto n^{1/4}$.

Figure 7 shows the FDTD simulated and experimentally measured electronically tunable absorption spectra of the cavity-coupled devices for high ($960 \text{ cm}^2/\text{V.s}$) (a) and low ($250 \text{ cm}^2/\text{V.s}$) (b) carrier mobility graphene. The carrier mobility is influenced by the degree of oxidation and polymer residues on the graphene surface. In both cases, E_F was varied between 0.7 eV to 1.0 eV. The high and low carrier mobility graphene devices exhibit a large $\sim 2 \mu\text{m}$ and $\sim 1 \mu\text{m}$ electrostatic tunability, respectively. The smaller peak in Figure 7b-left around $7.6 \mu\text{m}$ corresponds to polymer residue, which shows the effect of impurities in graphene's optical response. An increase in the

Fermi energy leads to an increase in the electron density of graphene (ρ), which strengthens the electric dipole moment generated by the LSP resonance on the nanopatterned edges and therefore enhances light absorption, as shown in Figure 7b. As seen from Figures 7a-right and 7b-right, there is a good agreement between CDA predictions, experimental measurements, and analytical graphene plasmon frequency $\omega_p \propto \sqrt{E_F} \propto \rho^{1/4}$ [183]. According to the experimental absorption spectra, the plasmon lifetimes ($\tau_{PL} = \hbar\Gamma^{-1}$) for high (960 cm²/V.s) and low (250 cm²/V.s) carrier mobility graphene are determined to be $\tau_{PL(high)} \approx 38\text{fs}$ and $\tau_{PL(low)} \approx 16\text{fs}$, respectively, which is compatible with the momentum relaxation time (τ).

Materials Characterization and Measurement

After RIE and the polymer removal, conductive AFM was used to confirm the presence of a patterned graphene layer on the substrate. After patterning the graphene on copper foil following the same procedure and parameters used to pattern the graphene sheet on the SU-8 layer, conductive AFM (MultiMode, Atomic Force Microscope, Nanoscope III, Digital Instruments, Santa Barbara, California) is employed to map of conductivity of the patterned graphene with nanoscale spatial resolution. Conductive (Au coated) cantilevers with spring constant $k = 0.06\text{ N/m}$ was used. Measurements are performed in contact mode and a full IV curve was collected at each pixel of the image. The Raman spectrum of the grown graphene sheet is measured by WITec Renishaw RM 1000B Micro-Raman Spectrometer with an excitation laser wavelength of 514 nm and a 50x objective lens. The results of conductive AFM and Raman spectroscopy are shown in Figure 5. The mobility is measured by using the model 2450 SourceMeter® SMU instrument and a four-point probe.

Plasmon-phonon Coupling

While the theoretical prediction using the FDTD method is in excellent agreement with the LSP peak locations (ω_0) in the experimental curves (Fig. 8b), it fails to explain the asymmetric line-shape of the resonance.

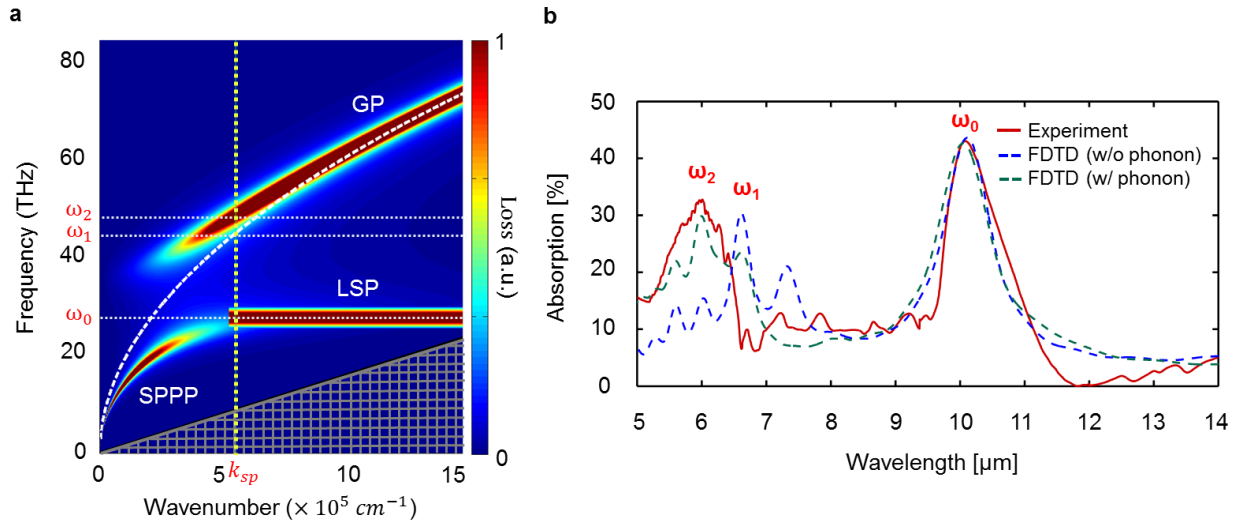


Figure 8: Energy loss dispersion.

(a) The loss function for graphene with $E_F = 1.0\text{eV}$. k_{sp} is the plasmon wavenumber associated with the second mode. ω_0 , ω_1 and ω_2 represent the LSPR, the resonance propagating plasmon frequency without and with plasmon-phonon interaction, respectively. (b) The experimental and theoretical prediction of the plasmon excitation on patterned graphene with period = 400 nm, diameter = 330 nm and $\mu = 960 \text{ cm}^2/\text{V}\cdot\text{s}$ coupled to an optical cavity with cavity thickness of 1.1 μm .

Hence, we can infer that in my device the effective combination of SU-8 polymer and the ion-gel matrix behaves as a polar substrate. Polar materials have ions of different valence, whose oscillating dipole moment gives rise to the interaction between electrons and optical phonons-called the Fröhlich interaction. The surface optical phonons in polar substrates are Fuchs–Kliewer like [184]. By placing graphene on a polar substrate the long range Fröhlich interaction mediates

the interaction between optical phonons and surface plasmons in graphene [48]. The interaction between polar substrate/graphene phonons and electrons in graphene modifies substantially the graphene plasmon dispersion relation. The white dotted line in Figure 8a represents the plasma frequency of graphene. The dynamic polarizability

$$\chi(\mathbf{q}, i\omega_n) = -\frac{1}{A} \int_0^\beta d\tau e^{i\omega_n \tau} \langle \mathbf{T} \rho_{\mathbf{q}}(\tau) \rho_{-\mathbf{q}}(0) \rangle, \quad (18)$$

determines several important quantities, such as effective electron-electron interaction, plasmon and phonon spectra, and Friedel oscillations. $\omega_n = \frac{2\pi n}{\beta}$ are Matsubara frequencies, \mathbf{T} is time ordering operator, $\beta = 1/k_B T$, where k_B is the Boltzmann constant, and n is an integer number. $\rho_{\mathbf{q}}$ is the density operator in q-space and A denotes the area of the sample. This quantity is calculated in the canonical ensemble for both of the sub-lattice density operators ($\rho = \rho_a + \rho_b$) [185]. The dynamic polarizability in the RPA regime is given by

$$\chi^{\text{RPA}}(\mathbf{q}, \omega) = \frac{\chi^0(\mathbf{q}, \omega)}{\varepsilon^{\text{RPA}}(\mathbf{q}, \omega)}, \quad (19)$$

where $\chi^0(\mathbf{q}, \omega)$ is the non-interacting (zeroth order) polarizability (single pair bubble) and $\varepsilon^{\text{RPA}}(\mathbf{q}, \omega) = \varepsilon_m - v_c(\mathbf{q})\chi^0(\mathbf{q}, \omega)$, with ε_m being the permittivity of the environment and $v_c(\mathbf{q}) = e^2/2\varepsilon_0 q$ the Coulomb interaction between the carriers. The RPA method corresponds to the expansion of $1/\varepsilon^{\text{RPA}}(\mathbf{q}, \omega)$, leading to an infinite power series over the bubble diagrams. If optical phonons are also considered, the effective dielectric function in the RPA expansion takes the form [48, 186]

$$\varepsilon^{\text{RPA}}(\mathbf{q}, \omega) = \varepsilon_m - v_c(\mathbf{q})\chi^0(\mathbf{q}, \omega) - \varepsilon_m \sum_l v_{\text{sph},l}(\mathbf{q}, \omega)\chi^0(\mathbf{q}, \omega) - \varepsilon_m v_{\text{oph}}(\mathbf{q}, \omega)\chi_{j,j}^0(\mathbf{q}, \omega). \quad (20)$$

The third term is the effective dielectric function for different phonon modes (l) coming from the electron-electron interaction mediated by substrate optical phonons, which couple to the electrons by means of the Fröhlich interaction, $v_{sph,l}(\mathbf{q}, \omega) = |M_{sph}|^2 G_l^0(\omega)$, where $|M_{sph}|^2$ is the scattering and G_l^0 is the free phonon Green's function. The last term of Equation. (20) corresponds to graphene's optical phonon mediated electron-electron interaction, $v_{oph}(\mathbf{q}, \omega) = |M_{oph}|^2 G^o(\omega)$. Here $|M_{oph}|^2$ defines the scattering matrix element and $G^o(\omega)$ is the free phonon Green's function. In Equation. (20), $\chi_{j,j}^0(\mathbf{q}, \omega)$ is the current-current correlation function. By taking the decay rate $\omega \rightarrow \omega + i\tau^{-1}$ into account, the dynamic polarizability reduces to $\chi^0(\mathbf{q}, \omega) \approx E_F q^2 / \pi \hbar^2 (\omega + i\tau^{-1})^2$ [48, 185]. The momentum relaxation time can be derived by considering the impurity, electron-phonon interaction and the scattering related to nanostructure edges $\tau = \tau_{DC}^{-1} + \tau_{edge}^{-1} + \tau_{e-ph}^{-1}$ [35, 48], which determines the plasmon lifetime and the absorption spectrum bandwidth. It can be evaluated via the measured DC mobility μ of the graphene sample using $\tau_{DC} = \mu \hbar \sqrt{\pi \rho} / e v_F$, where $v_F \sim 10^6$ m/s is the Fermi velocity and $\rho = (E_F / \hbar v_F)^2 / \pi$ is the charge carrier density. $\tau_{edge} \approx (1 \times 10^6 / w - w_0)^{-1}$ is due to the scattering from the nanostructure edges, where w is the edge-to-edge distance of the holes, $w_0 \approx 7nm$ is the parameter that includes edge effects, and $\tau_{e-ph} = \hbar / 2 \text{Im}(\Sigma_{e-ph})$ is related to the scattering because of electron-phonon coupling. $\text{Im}(\Sigma_{e-ph}) = \gamma |\hbar \omega - \text{sgn}(\hbar \omega - E_F) \hbar \omega_{oph}|$, where Σ_{e-ph} is the electron self-energy, $\gamma = 18.3 \times 10^{-3}$ is a dimensionless constant describing the electron-phonon coupling coefficient, and $\hbar \omega_{oph} \approx 0.2eV$ is the graphene optical phonon energy [35]. From this it is evident that the plasmon lifetime is reduced due to the electron-phonon interaction and edge scattering, but the DC

conductivity which is used to calculate the dielectric function of graphene is invariant if the edge-to-edge distance of the pattern is more than the carrier mean free path ($L_{MFP} = v_F \tau_{DC}$).

The modified Drude model is not valid for a patterned graphene sheet only if the edge-to-edge distance is much smaller than the carrier mean free path of electrons and holes. For the chosen pattern and carrier mobility ($\mu = 960 \text{ cm}^2/\text{V.s}$), the carrier mean free path ($L_{MFP} = v_F \tau_{DC} < 42 \text{ nm}$) is smaller than the edge-to-edge distance ($=70 \text{ nm}$), which means that the modified Drude model is a good approximation for the dielectric function of this patterned graphene sheet. In presence of hard boundaries, atomic displacement vanishes at the boundaries, thereby modifying the acoustic and optical phonon dispersion. This means we need to consider a graphene nanoribbon (GNR) with zigzag-edge or armchair-edge and N periods (N is the number atoms between two edges) with several quantized vibration modes. This model is applied in the long wavelength limit; therefore only the lowest vibration modes up to $N/2$ appear. By applying the boundary conditions to the displacement equation, the longitudinal (LO) and transverse (TO) optical phonon branches are changed, i.e. $\omega_n^2 = \omega_{LO}^2 - \lambda^2(q_n^2 + q^2)^2 + \beta_L^2(q_n^2 + q^2)$ and $\omega_n^2 = \omega_{TO}^2 - \beta_T^2(q_n^2 + q^2)$. This means the optical phonon frequency, which is almost the same for both branches (LO and TO), shifts from $\omega_{op} \sim 1581 \text{ cm}^{-1}$ to $\omega_{op} \sim 1591 \text{ cm}^{-1}$ for both zigzag-edge and armchair-edge GNR [187-189]. I used this modified optical phonon frequency in Figure 8. The effect of this change is very small.

The coupling of plasmon and substrate/graphene phonon can be characterized through the loss function (Z), which is the imaginary part of inverse effective dielectric function calculated via the generalized RPA theory [47, 48]

$$Z \propto -\text{Im}\left(\frac{1}{\epsilon^{RPA}}\right). \quad (21)$$

The loss function represents the amount of energy dissipated by exciting the plasmon coupled to the substrate and optical phonons in graphene. The surface plasmons in graphene are damped through radiative and nonradiative processes [29]. Nonradiative damping transfers the plasmon energy to hot electron-hole excitation by means of intraband transition. Figure 8a shows the loss function for graphene with carrier mobility $\mu = 960 \text{ cm}^2/\text{V}\cdot\text{s}$ and $E_F = 1.0\text{eV}$. The thickness of the optical cavity is chosen to be $1.1 \text{ }\mu\text{m}$ such that the first (ω_0) and second (ω_2) modes lead to 44% and 33% light absorption, respectively. The plasmon assisted electron-hole pair generation in this structure lies outside the Landau intraband damping region, indicated by the shaded area in Figure 8a. A band gap in the plasmon-phonon dispersion relation is formed via Fröhlich interaction between graphene plasmons and optical phonons [190]. This coupling leads to the splitting of the energy into two distinct branches: surface plasmon phonon polaritons (SPPPs) and graphene plasmons (GPs) [39, 48, 185, 186, 190]. The horizontal branch line marked as ω_0 is the LSP mode in Figure 8a and is independent of the plasmon wavevector due to the localization of the LSP. The asymmetric line shape of the first band (ω_0) in Figure 8b, which is observed in experiments, is due to the merging of these two bands (LSP and SPPP). Figure 8a shows a clear blue shift in the GP band at a wavevector ($k_{\text{sp}} \approx 5.5 \times 10^5 \text{ cm}^{-1}$), corresponding to the edge-to-edge distance between the holes in presence of edge effect. Interestingly, there exists a discrepancy in the location of the second mode peak of the FDTD curve simulated without accounting for optical phonons (ω_1) from that of the experimental spectrum (ω_2) (Figure 8b). This is attributed to the plasmon-phonon coupling, and I show that by inserting the plasmon-phonon interaction as a perturbation and using $\varepsilon^{\text{RPA}}(\mathbf{q}, \omega)$ in Equation. (20) as effective graphene dielectric function in the FDTD simulations, one can recover the experimentally observed blue shift, as illustrated in Figure 8b by the green dotted line. The simple Drude model cannot capture the plasmon-phonon interactions which leads

to discrepancies between FDTD predictions and experimental measurements as can be observed in Figure 8b. In the long wavelength regime, by substituting $\chi^0(\mathbf{q}, \omega) \approx E_F q^2 / \pi \hbar^2 (\omega + i\tau^{-1})^2$ and v_c into Equation. (20), the second term on the right-hand side is reduced to the Drude model dielectric function

$$\varepsilon_{Drude} = -v_c(\mathbf{q})\chi^0(\mathbf{q}, \omega) = \frac{e^2 E_F q}{2\varepsilon_0 \pi \hbar^2 (\omega + i\tau^{-1})^2}. \quad (22)$$

According to Equation. (22), the in-plane momentum of the pristine graphene should be equal to $q = 2/t$. In Eq. (20), the phonon terms, which are small relative to ε^{Drude} , perturb the original system. In order to include the electron-phonon coupling in the simulation and to predict the experimental results with higher accuracy, Equation. (20) has been used as the input data in the FDTD simulations to generate the plasmon-phonon dispersion diagram of Figure. 8(b) with much improved correspondence between prediction and experimental observation. This analysis explains different processes involved in the experimental results and the physical optoelectronic phenomena and highlights the plasmon-phonon interaction leads to the hybridization of the plasmon dispersion relation, which gives rise to a blue shift in the propagating surface plasmon spectrum. However, the main absorption peak (ω_0), which originates from LSP, remains unperturbed due to frequency domain separation between the phonon and LSP resonances.

Conclusion

In conclusion, I have presented a scheme to increase the light-graphene interaction by the direct excitation of plasmons on patterned monolayer graphene coupled to an optical cavity. My design of a square lattice of holes on graphene, which is experimentally realized following a simple nanoimprinting technique, not only preserves material continuity for electronic conductivity,

which is essential for optoelectronic devices, but also leads to direct plasmon excitation that is independent of the incident light polarization. Therefore, my design outperforms other nanoribbon-based devices whose absorption is polarization-dependent, thereby reducing their performance for unpolarized light. This approach triggers the direct excitation of cavity-coupled plasmon in CVD grown monolayer graphene with a cavity thickness of $L = 1.1 \mu\text{m}$ and yields an experimentally observed absorption of $\sim 45\%$, which is the highest value reported so far in the $8 - 12 \mu\text{m}$ band. I showed that a reduction in carrier mobility of graphene decreases the absorption to $\sim 30\%$, which is nonetheless higher than previous studies. Furthermore, electronically controlled dynamic tunability ($\sim 2 \mu\text{m}$) is successfully demonstrated. I have shown experimentally and theoretically that the carrier mobility of graphene, which is influenced by the defect density, determines the enhanced absorption bandwidth and line-shape. Further, CVD grown graphene quality, pattern, gating optimizations, and alternative low-absorbance dielectrics as gating materials are needed in order to reach the theoretical maximum absorption of $\sim 60\%$ for a cavity thickness of $L = 1.6 \mu\text{m}$. Such voltage tunable high absorption in monolayer graphene will enable the development of various practical graphene based optoelectronic devices like photodetectors, sensors, modulators, *etc.*

CHAPTER 3: THE EFFECTS OF ANGLE OF INCIDENCE, POLARIZATION AND PATTERNING ON DIRAC PLASMONS

Published at <https://pubs.acs.org/doi/10.1021/acsnano.8b06601> on 7 December 2018 by ACS Nano. DOI: 10.1021/acsnano.8b06601, Alireza Safaei, Sayan Chandra, Michael N. Leuenberger, and Debashis Chanda

Introduction

Graphene is one of the most widely studied two dimensional materials due to its special electrical and optical properties. Various promising strategies and ideas are being proposed for optical, electrical and mechanical devices based on monolayer graphene by taking advantage of unique properties, such as high carrier mobility [74, 75, 141-143, 191], fast carrier relaxation time and electrostatic tunability in the devices such as transistors [144], photodetectors [33, 146], optical switches, nanolasers [148] and chemical sensors [192-194]. Compared to other two-dimensional materials, large scale monolayer graphene can be grown easily by using chemical vapor deposition (CVD) method with the carrier mobility lower than the mechanical exfoliated flakes and can be subsequently transferred to different substrates which makes real-world graphene based optoelectronic devices viable. However, a major bottleneck is the low light-matter interaction in graphene that needs to be enhanced. Graphene is an ultrathin semi-metal with a Dirac point in the band-structure where the conduction and valence bands cross, leading to a constant light absorption (~2.3%) in the visible regime [76] and low absorption (< 3%) in the mid-IR wavelength ranges [149]. Different strategies have been pursued to increase the interaction of the incident light with monolayer graphene, while preserving its inherent properties such as high carrier mobility and fast relaxation time. To establish the feasibility of graphene based infrared

absorbers and detectors, three critical aspects need to be considered, (i) dependence of absorption to the angle of incidence, (ii) spectral tunability and selectivity for wide band operation, and (iii) polarization dependence. Ideally, polarization and angle independent absorption are desirable properties of an absorber. Coupling the near-field of a metallic metasurface to graphene [16, 20, 22, 155-157] is an indirect solution to increase the light-graphene interaction, despite the high loss of the incident light as resistive ohmic loss in the metal. Additionally, owing to asymmetric metasurface designs most of the absorbers reported till date are sensitive to the polarization of incident light and exhibit limited spectral tunability [39, 47, 195]. In another approach, coupling a pristine [27, 159] and nanopatterned monolayer graphene to an optical cavity has been implemented to enhance absorption. Although, these recent works have experimentally demonstrated the enhancement of absorption for normal incident light [11, 39, 47, 50, 195], little is known about their absorption at higher angles of incidence, incident polarization or pattern edge states in combination with doping level.

In the infrared domain, exciting Dirac plasmons [1] on nanopatterned graphene has been adopted as a route to couple and concentrate the incident light directly on the surface thereby enhancing the infrared absorption [44, 50]. Depending on the nanopattern design, the Dirac plasmons on graphene can be propagating surface plasmon polaritons (SPP) or localized surface plasmons (LSPs) modes. Plasmons are qualitatively characterized by their lifetimes. Longer lifetime results in stronger electric field confinement, which manifests as higher and sharper absorption (lower FWHM) in the spectral response. It has been reported that nanopatterning of graphene introduces graphene edges, which play a vital role in modifying the light absorption spectrum. Edge scattering effects, radiative and non-radiative decay arising from Landau damping through interband and intraband transitions contribute collectively to increase the decay rates of

the plasmonic excitations [1, 11, 29, 48, 158, 163]. Therefore, the fundamental question that arises is how critical is the role of graphene edge on the localized surface plasmon (LSP) excitation, decay rate and overall absorption behavior of patterned graphene? Here, in order to investigate these aspects we identified complementary nanostructures, i.e. nanoholes and nanodisks, such that the qualitative nature of the edges are similar. A direct comparison of these complementary structures elucidates the differences in the plasmonic excitations, the degree of electrostatic spectral tunability and polarization dependences as a function of incident angle. We adopt a combinatorial investigation using theory and experiment to gain insight into the underlying physical phenomena [2, 166].

Here, in order to investigate these aspects I identified complementary nanostructures, *i.e.* nanoholes and nanodisks, such that the qualitative nature of the edges are similar. A direct comparison of these complementary structures elucidates the differences in the plasmonic excitations, the degree of electrostatic spectral tunability and polarization dependences as a function of incident angle. I adopt a combinatorial investigation using theory and experiment to gain insight into the underlying physical phenomena. Based on this, I demonstrate the effect of graphene nanopatterning and the edges on the plasmon lifetime and the light absorption. The maximum achieved light absorption is experimentally measured to be 90% (60%) for the cavity coupled graphene nanodisk (nanohole) array for the specified geometry and $E_F = -1\text{eV}$. This enhanced absorption is independent of the light polarization. An ideal strategy to enhance the light-graphene interaction should be independent of θ_i . I measure the dependence of the light absorption as a function of θ_i for s- and p-polarized light, which shows excellent agreement with the simulated results. The wide-angle absorption of unpolarized light by the patterned nanohole/nanodisk graphene devices are almost independent of the angle of incidence for $\theta_i < 50^\circ$.

Plasmonic resonances in the complementary arrays

Plasmon Lifetime

The architecture of the proposed graphene absorber is illustrated in Figure 9a. Pristine graphene grown on copper foil by CVD method was transferred on Si⁺⁺ (100 μm)/Al₂O₃ (15 nm)/ITO (10 nm) substrate. A layer of Ti/Au (5 nm/50 nm) was deposited on the transferred graphene to accumulate the electrical charge over the graphene sheet effectively.

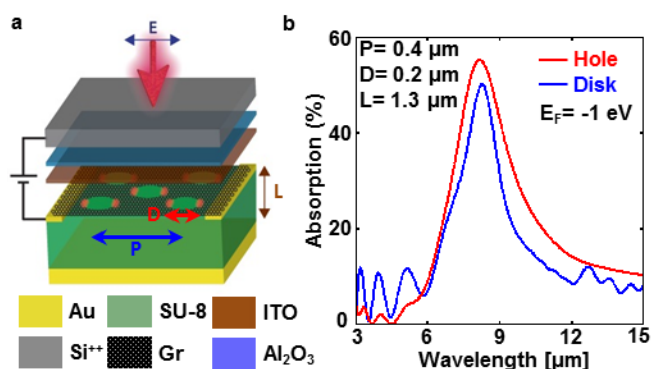


Figure 9: Comparison of cavity-coupled hole and disk arrays in graphene.

(a) Schematic of the optical cavity-coupled patterned graphene. The top layers are depicted separately to be distinguishable. (b) The light absorption spectra of the optical cavity-coupled graphene hole (red) and disk (blue) arrays with $P=400$ nm, $D=200$ nm, $L=1300$ nm and $E_F=-1$ eV.

The hole/disc diameter (D) and period (P) were varied to tune the LSPR at a desired wavelength whereby the cavity length was chosen to satisfy the quarter wavelength condition $L = m\lambda/4n_{\text{eff}}$. At this condition, constructive interference of the incident and reflected electric fields on graphene sheet intensifies the LSPs and enhances light-matter interaction, as shown in Figures 2 and 10. Here, L is the cavity thickness, n_{eff} is the effective refractive index of the optical cavity spacer, m is the m -th order of the cavity mode and λ is the light wavelength. The optical response

of the designed graphene absorber was simulated by FDTD approach. In these simulations, the mobility of graphene was chosen to be a modest $500 \text{ cm}^2/\text{V}\cdot\text{s}$ (scattering rate $\Gamma = 0.02 \text{ eV}$) to closely resemble the experimentally measured mobility, and the optical constants of graphene corresponding to different Fermi energies were calculated using the Drude model [11, 75].

The total light absorption spectra of the optical cavity-coupled nanopatterned graphene are different for the complementary graphene nanodisk and nanohole arrays with $P = 400 \text{ nm}$, $D = 200 \text{ nm}$ and $L = 1.3 \text{ }\mu\text{m}$, as shown in Figure 9b, such that the peak bandwidth of the graphene nanodisk is smaller than that of its complementary graphene nanohole array. Interestingly, while the plasmon lifetime, which is inversely proportional to the FWHM of the absorption peak in nanodisks is longer, it does not translate to a higher absorption. At resonance the extinction cross-section of any nanopattern exceeds the geometrical area by several factors, which scales differently for the complementary nanohole and nanodisk patterns. This in turn determines the effective absorption amplitude, which is higher in case of the nanohole pattern, in spite of shorter plasmon lifetimes. Therefore, the presence of surface plasmons breaks the symmetry of the complementary nanohole and nanodisk arrays due to their different plasmon decay rates, which suggests that maximum light absorption for respective patterns can be achieved by optimizing the geometrical area of the nanopattern such that the extinction cross-section is highest.

Geometrical Tunability

To obtain the maximum light absorption for the cavity-coupled graphene nanohole and nanodisk arrays, the optical response for different geometrical parameters (period and diameter) were simulated for a fixed Fermi energy ($E_F = -1 \text{ eV}$) at normal angle of incidence. For the

nanohole array, a reduction in edge-to-edge distance can be achieved by either increasing the diameter for a fixed period or decreasing the period for a given diameter.

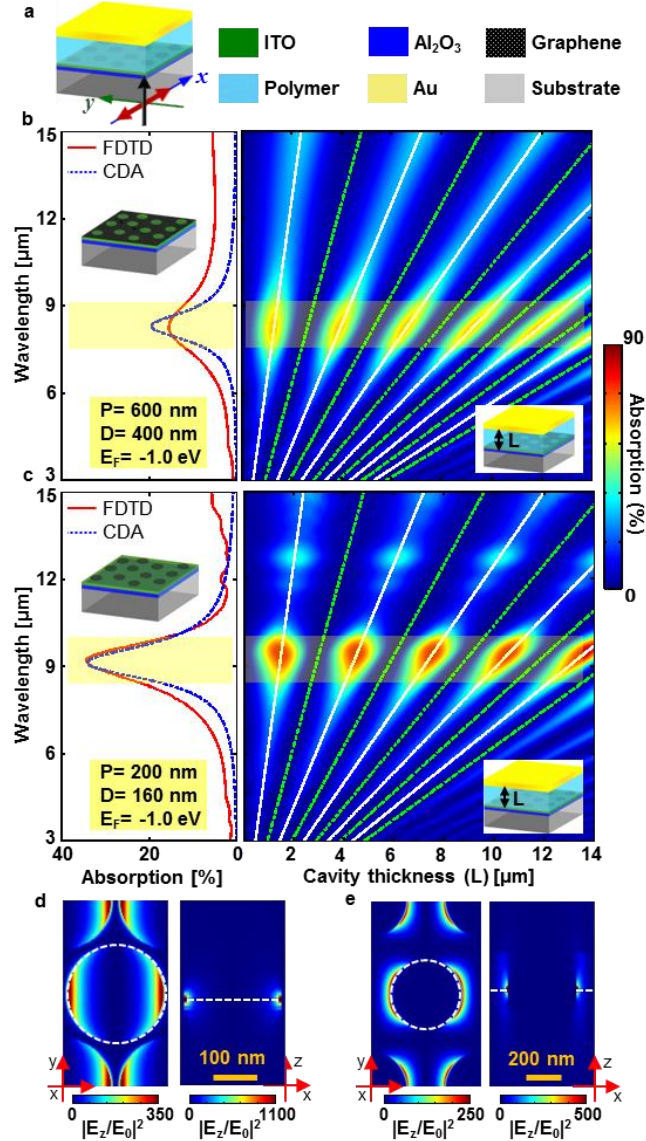


Figure 10: Exciting surface plasmon on graphene nanodisk and nanohole arrays.

(a) Schematic of the optical cavity-coupled patterned graphene. The light absorption spectra of the optical cavity-coupled graphene nanohole array with $P=600$ nm, $D=400$ nm, $E_F=-1$ eV (b) and nanodisk array with $P=200$ nm, $D=160$ nm and $E_F=-1$ eV (c) arrays. The left panels show the simulated light absorption spectra of the nanopatterned graphene arrays obtained by FDTD (solid red) and CDA (dashed blue) approaches. The top view and side view of the z-component electric field intensity of the graphene nanodisk (d) and nanohole (e) arrays.

By applying both strategies, I observed that the reduction in the edge-to-edge distance leads to a blue shift in the LSPR frequency, as predicted by Equations. (8) and (23) and shown in Figure 11a-b. In this case, the device parameters were optimized to obtain maximum absorption at $\lambda_{res} = 8\mu\text{m}$.

As explained by details in chapter 2, the LSPR frequency of the nanopatterned graphene is given by [11, 44, 50]

$$\omega_{res} = B\sqrt{\frac{\Im E_F}{d}}, \quad (23)$$

where B is a constant value, d is the edge-to-edge distance of the nanopattern and \Im is the eigenvalue of the self-consistent total electric potential equation. For the graphene nanodisk pattern, the increase in diameter for a constant period results in a red shift of the LSPR wavelength, as shown in Figure 11c-d and predicted by Equation. (23), while the decrease in the period for a constant diameter enhances the far-field and near-field coupling of the nanodisks, giving rise to a slight red shift. The amount of light absorption on the graphene nanodisk array depends on the density ratio (ρ_r), which is defined as the ratio of the graphene area to the unit cell area. The density ratio can be enhanced by increasing the diameter or decreasing the period. For a cavity thickness of $L= 1.5 \mu\text{m}$, the light absorption was found to be a continuous increasing function of the diameter and a decreasing function of period, as shown from Figure 11c-d.

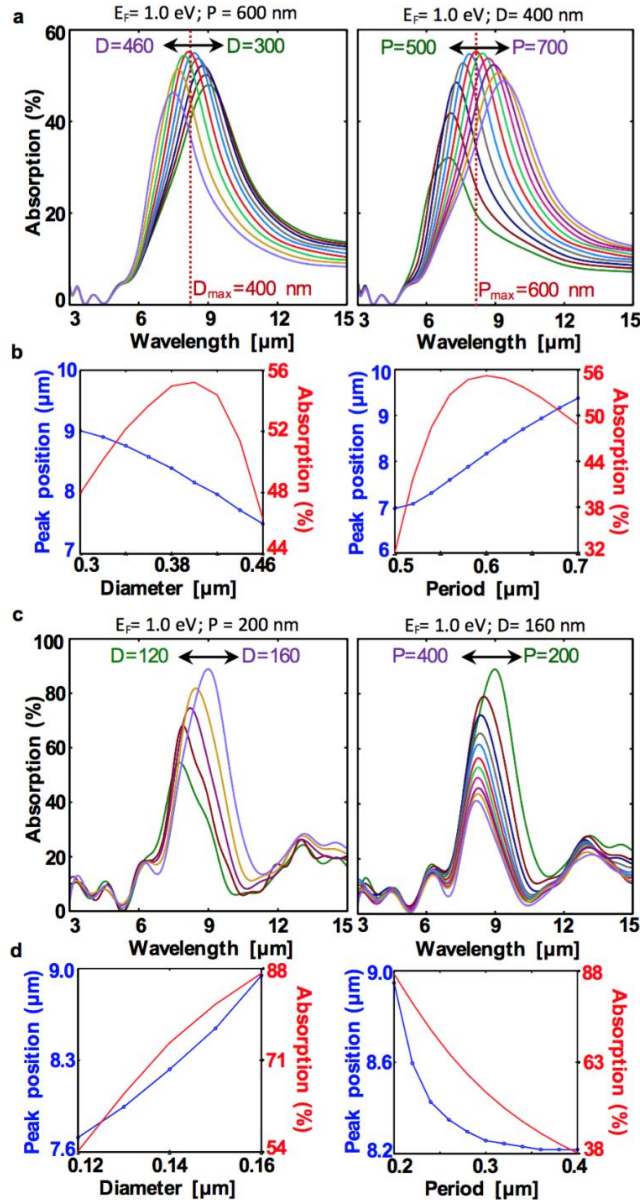


Figure 11: Geometrical tunability.

(a) The light absorption of the cavity-coupled nanohole graphene with the thickness $L=1.3 \mu\text{m}$ for different diameters in a constant period ($P=600 \text{ nm}$) (left) and different periods in a constant diameter ($D=400 \text{ nm}$) (right). (b) The peak position and the absorption for the graphene nanohole as a function of diameter (left) and period (right). (c) The light absorption of the cavity-coupled nanodisk graphene with the thickness $L=1.5 \mu\text{m}$ for different diameters in a constant period ($P=200 \text{ nm}$) (left) and different periods in a constant diameter ($D=160 \text{ nm}$) (right). (d) The peak position and the absorption for the graphene nanodisk as a function of diameter (left) and period (right).

Fabrication and characterization

Nanopatterning Monolayer Graphene

To validate the simulated results, absorber devices were fabricated using period and diameter values that yielded highest absorption for nanoholes and nanodisks respectively. The nanohole and nanodisk arrays are patterned on the transferred monolayer graphene by electron beam lithography (EBL) followed by oxygen RIE. The SEM images in Figure 12a shows the fabricated hole and disk arrays in the transferred graphene. A layer of semi-transparent SU-8 photoresist polymer was spun-coated on the patterned graphene to form the optical cavity followed by 2 hours UV-exposure and one-hour baking (95 °C). A hard layer of Al₂O₃ (50 nm) is deposited on SU-8 to protect SU-8 from metal deposition and an optically thick layer of gold (200 nm) was electron beam evaporated to form the back mirror. The Si⁺⁺ (100 μm) sheet used as the back gate has ~ 70% transmission in mid-IR range, as shown in Figure 13 and light is incident from the silicon side. During the transfer and fabrication process, the monolayer graphene was found to be chemically self-doped as p-type with $E_F \sim -0.6$ eV that can be attributed to residual polymer and presence of p-type Al₂O₃ dielectric layer [196, 197]. Electrostatic tunability of E_F was achieved by applying a voltage across the Al₂O₃ layer such that a negative voltage resulted in accumulation of positive charges (holes) thereby driving the system to a higher Fermi level. The Fermi energy of the nanopatterned graphene can be altered from -0.55 eV to -1.0 eV as shown in Figure 12b which is associated with a decrease in channel resistance by a factor of 3. The Fermi energies of the patterned graphene corresponding to the different gate-voltages are derived *via* the measured capacitance of the gate-dielectric and moreover, fitting to the theoretical conductivity. Increase in the Fermi energy of graphene to $|E_F| = 1.0$ eV is necessary to intensify the electric dipoles oscillations that allow more photons to couple to the patterned graphene edges. My choice of high-

k hard dielectric (Al_2O_3) for electrostatically doping graphene provides superior chemical stability in time over the more commonly used ion-gel and very low gate leakage, as shown in Figure 14.

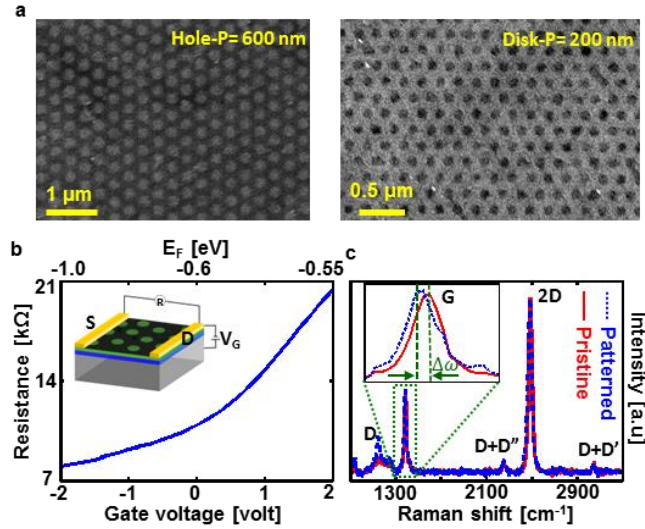


Figure 12: Fabrication and characterization.

(a) SEM image of the fabricated graphene nanohole (left) and nanodisk (right). (b) The electrical resistance of the patterned graphene as a function of the gate voltage. (c) The Raman spectroscopy of the pristine and patterned monolayer graphene ($E_F = -0.7$ eV). The electrical resistance and Raman measurements are done on the graphene hole array with $P = 600$ nm and $D = 400$ nm.

Raman spectroscopy was performed to confirm the quality of graphene before and after nanopatterning. As shown in Figure 12c, the characteristic 2D and G bands of graphene are visible for pristine and patterned graphene, however a red shift ($\Delta\omega \sim 7 \text{ cm}^{-1}$) in the spectrum for patterned graphene was observed which suggests a modification in the dispersion function of the acoustic and optical phonons due to the nanopatterning, as explained in chapter 2.

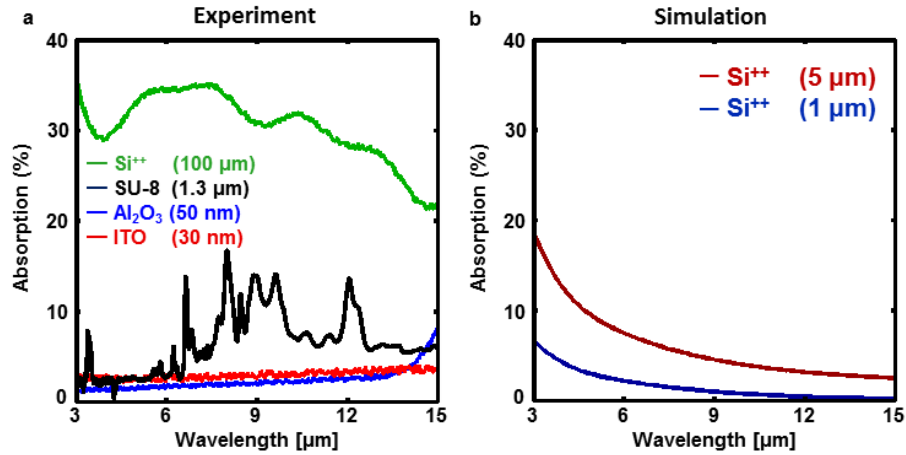


Figure 13: Light absorption of different layers.

(a) The measured optical absorption of the different layers used to fabricate the cavity-coupled nanopatterned graphene absorber device. (b) The simulated optical absorption of doped silicon with different thicknesses.

The Light Absorption of the Substrate

Since in the fabricated samples light is incident from the silicon side, the light transmission of silicon wafer with thickness of 100 μm should be high enough. The measured transmission spectrum shows that the average light transmission of the doped silicon substrate in mid infrared wavelength regime is $\sim 70\%$. To quantify the amount of incident power reaching the nanopatterned graphene layer, the optical absorption spectra of different layers are measured separately and shown in Figure 13. Based on these diagrams, the net amount of the light power reaching to the graphene layer is $\sim 60\%$ of the incident light power at $\lambda = 9 \mu\text{m}$. However, by reducing the silicon substrate thickness below 5 μm (Figure 13), the percentage of incident light power on the graphene layer can be increased to over 80%.

The Quality of the Gate Dielectric

The quality of the high-k gate-dielectric for electrostatic doping of graphene is an important factor for the usability of the designed device. The measured capacitance of the hard-dielectric layer which is 15 nm thick layer of Al_2O_3 is $C = 0.93 \mu\text{F}/\text{cm}^2$. Such gate dielectric can be used to electrostatically dope the Fermi level of the self-doped patterned graphene to $E_F = -1 \text{ eV}$. The high-k dielectric Al_2O_3 has more stability in time compared to the conventionally used soft-ion gel gate dielectric, as the measured light absorption spectra of the corresponding patterned graphene absorbers in a 6-month interval proves this (Figure S8a-b). The leakage current of the gate-dielectric is another important parameter in power usage which is very low ($\sim 10^{-11} \text{ A}$) for 15 nm thick layer of the grown Al_2O_3 , as shown in Figure 14.

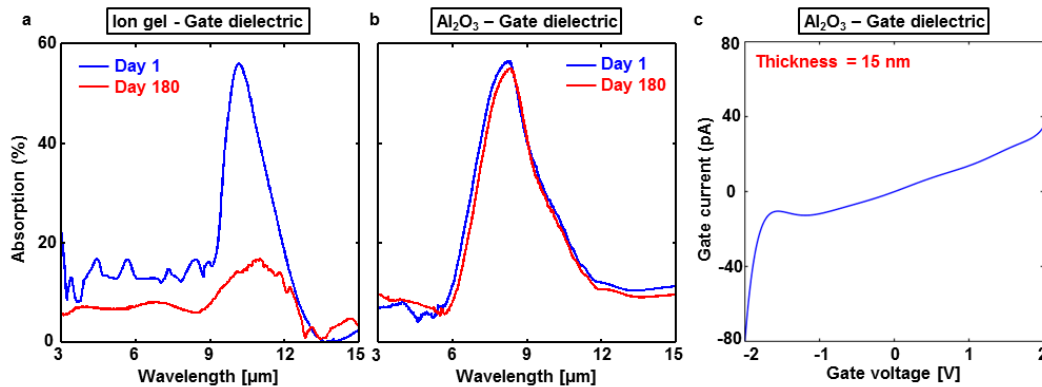


Figure 14: Characterization and comparison of the hard (Al_2O_3) and soft (ion-gel) gate dielectrics.

The light absorption spectra of the fabricated patterned graphene samples doped by ion gel (a) and Al_2O_3 (b) in a 6-month time interval. (c) The gate leakage electric current of the 15 nm thick layer of Al_2O_3 .

Finding the Carrier Mobility

To find the experimental value of the carrier mobility μ of the patterned graphene and its Fermi energy, the measured electrical resistance R of the patterned graphene is fitted to the theoretical formula ($R = R_0 + 1/\rho e\mu$), where R_0 is the minimum resistance at $V_G = -1$ V, $\rho = C\Delta V/e$ is the electron density and e is the Coulomb charge. Based on the diagrams in Figure 15, the carrier mobility of the patterned graphene is $\mu = 500 \text{ cm}^2/\text{V}\cdot\text{s}$. By using this diagram and the capacitance of the gate-dielectric, the graphene Fermi level corresponding to each gate voltage is derived.

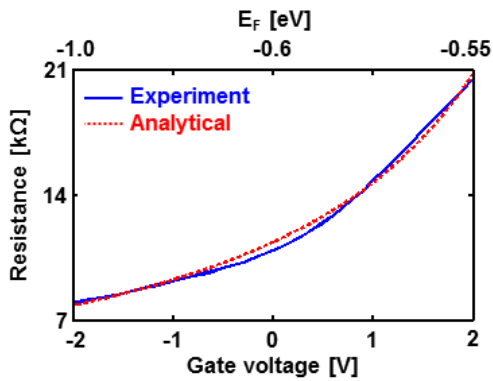


Figure 15: Electrostatic doping of graphene.

The experimental and analytical model diagrams are overlaid to find the carrier mobility of the patterned graphene sheet.

Geometric and electrostatic tunable absorption at normal incidence

The normal-angle reflection spectra of the fabricated cavity-coupled graphene nanohole and nanodisk absorbers were measured using a Bruker Vertex 80 Fourier transform infrared spectrometer (FTIR). The light reflection from the absorber stack without patterned graphene, *i.e.* Si⁺⁺ (100 μm)/Al₂O₃ (15 nm)/ITO (30 nm)/SU-8 (*L*)/Al₂O₃ (50 nm)/gold (200 nm) was taken as the reference and the light absorption spectra was calculated as $A=1-R$. As shown in Figure 16a, the light absorption of the graphene nanohole array reaches $\sim 60\%$ (at $E_F = -1$ eV), which is 35% higher than the previously reported maximum absorption in the 8 – 12 μm band in chapter 2. Electrostatic tunability of ~ 2.46 μm is observed by changing E_F from -0.55 eV to -1 eV.

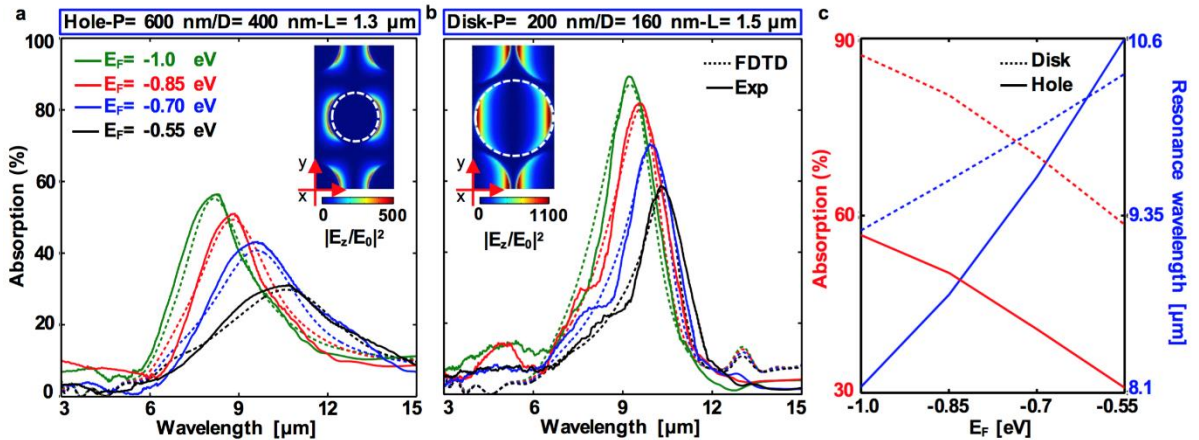


Figure 16: Experimental and simulated results of enhanced light-matter interaction in the cavity-coupled patterned graphene.

(a) The simulated and measured light absorption of the cavity-coupled graphene nanohole array with $P=600$ nm, $D=400$ nm and $L=1.3$ μm for different Fermi energies. (inset) The top view of the z-component near-field profile corresponds to the $E_F= -1.0$ eV. (b) The simulated and measured light absorption of the cavity-coupled graphene nanodisk array with $P=200$ nm, $D=160$ nm and $L=1.5$ μm for different Fermi energies. (inset) The top view of the z-component near-field profile corresponds to the $E_F= -1.0$ eV. (c) The resonance wavelength and corresponding light absorption of the cavity-coupled graphene nanodisk and nanohole arrays as a function of Fermi energy.

A near perfect absorption of 90% was recorded for the nanodisk array, which is electrostatically tunable over a spectral width of $\sim 1.11 \mu\text{m}$. There is in very good agreement with the simulated results. Increase in the Fermi energy to the negative values means more hole density and creation of stronger electric dipoles on the patterned graphene which results in enhanced light absorption along with a blue shift in the LSPR frequency as depicted in Figure 16c. The extraordinary near-field enhancement by factors of 500 and 1100 (inset of Figures 16a and 16b) for nanohole and nanodisk arrays, respectively, explain the high light-matter interaction and infrared absorption values recorded experimentally.

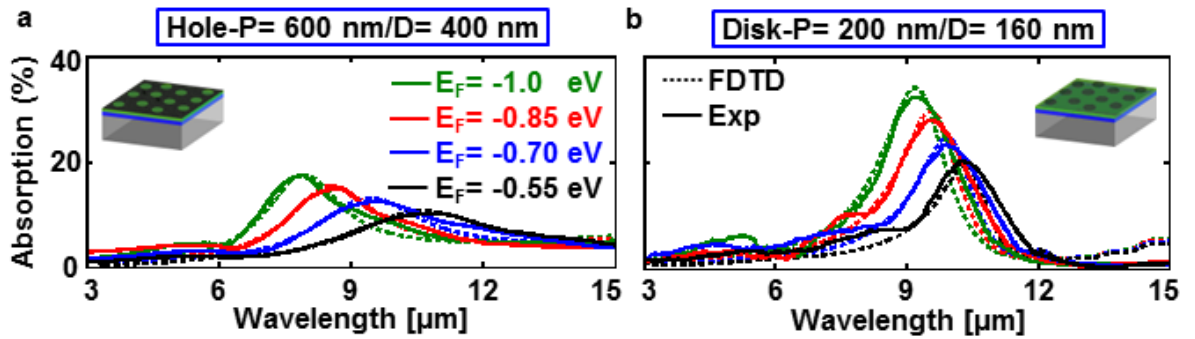


Figure 17: Experimental and simulated results of enhanced light-matter interaction in the patterned graphene without optical cavity.

(a) The simulated and measured light absorption of the patterned graphene nanohole array with $P=600 \text{ nm}$, $D=400 \text{ nm}$ for different Fermi energies. (b) The simulated and measured light absorption of the patterned graphene nanodisk array with $P=200 \text{ nm}$, $D=160 \text{ nm}$ for different Fermi energies.

The measured light absorption spectra of the patterned graphene without optical cavity is shown in Figure 17 along with simulated spectra ($A=1-T-R$) to further elucidate the excellent agreement between experiment and theory. This figure demonstrates the experimental and the corresponding simulated results for the light absorption spectra of the nanohole (Figure 17a) and nanodisk (Figure 17b) patterned graphene without optical cavity which were obtained by the

measured R and T spectra. The light reflection/transmission from the absorber stack without patterned graphene, *i.e.* Si⁺⁺ (100 μm)/Al₂O₃ (15 nm)/ITO (30 nm) was taken as the reference for the experimental measurement. The good agreement of simulated and measured spectra validates the experimental results.

Angle dependent infrared absorption

Effect of Angle of Incidence for the Cavity-coupled and Cavity-uncoupled Systems

To validate the operability of any absorber, it is critical to investigate its angular dependence to light. In the seminal work by Thongrattanasiri *et. al.*, it was analytically shown for periodically patterned graphene that under the condition of no transmission, the angular optical response to light, which depends on the polarization, is primarily determined by its mobility and extinction cross-section. Enhanced absorption would necessitate maximizing the extinction cross-section, which can be achieved by pattern optimization such that the decay rate (κ) is much higher than the radiative (κ_r) contribution ($\kappa \gg \kappa_r$). The decay rates along with the plasmon frequency ω_p determines the graphene polarizability given by

$$\alpha(\omega) = \frac{3c^3 \kappa_r}{2\omega_p^2} \frac{1}{\omega_p^2 - \omega^2 - i\kappa\omega^3/\omega_p^2}. \quad (24)$$

Under the assumption that the polarizabilities of monolayer graphene nanohole/nanodisk are almost independent of the angle of incidence, the LSPR frequency is expected to not be affected by change in incident angle of light. This is confirmed by the FDTD simulations where the LSPR frequency is found to be almost independent of θ_{inc} , for both nanohole and nanodisk array patterned graphene with and without optical cavity (See Figures 19 and 20). At higher angles of incidence,

the peak absorption of the system differs for the in-plane polarization (p-polarization) and the out-of-plane (s-polarization) light.

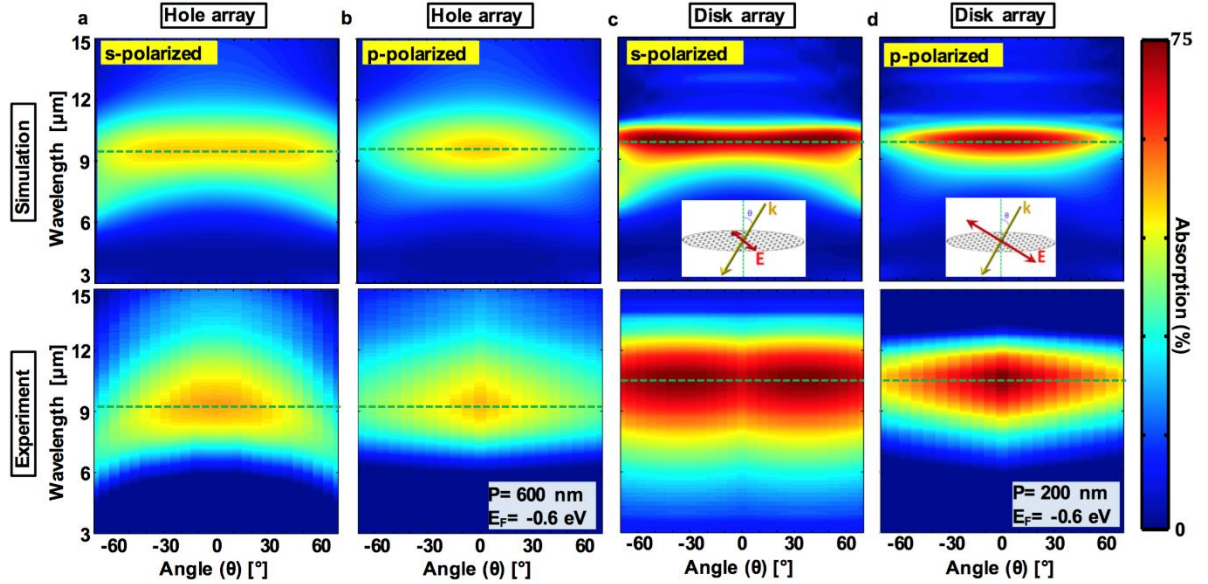


Figure 18: Angle dependent infrared absorption.

The simulation (top) and experimental (bottom) results for the angular light absorption of the cavity-coupled graphene nanohole (a-b) and nanodisk (c-d) arrays with $E_F = -0.6$ eV as a function of angle of incidence. Inset shows the schematic of the s- and p-polarized incident light. The polarized light measurements are normalized to the light intensity after the polarizer.

For p-polarized light, the absorption magnitude scales with the electric field component parallel to the surface, $E_i \cos \theta_i$ as the angle of incidence increases. In case of s-polarized light, the LSPR frequency is almost independent of the angle of incidence for the nanohole and nanodisk array devices in the cavity coupled (Figure 18) and no-cavity (Figures 19 and 20) systems. However, the magnitude of absorption increases with angle of incidence for s-polarized light in contrast to the results obtained for p-polarized light shown in Figures 19 and 20. While the magnitude of electric field parallel to graphene surface remain unaffected for all angles of incidence (see inset of Figure 18c), the scattering cross-section increases and scales as $E_i \sin \theta_i$.

This explains the enhancement in absorption as the angle of incidence increases (Figures 19 and 20). Unlike the no-cavity nanodisk array absorber, the cavity couple system exhibits an increase in absorption for $0^\circ < \theta_i < 50^\circ$ but for higher angles, the absorption drops (Figure 18).

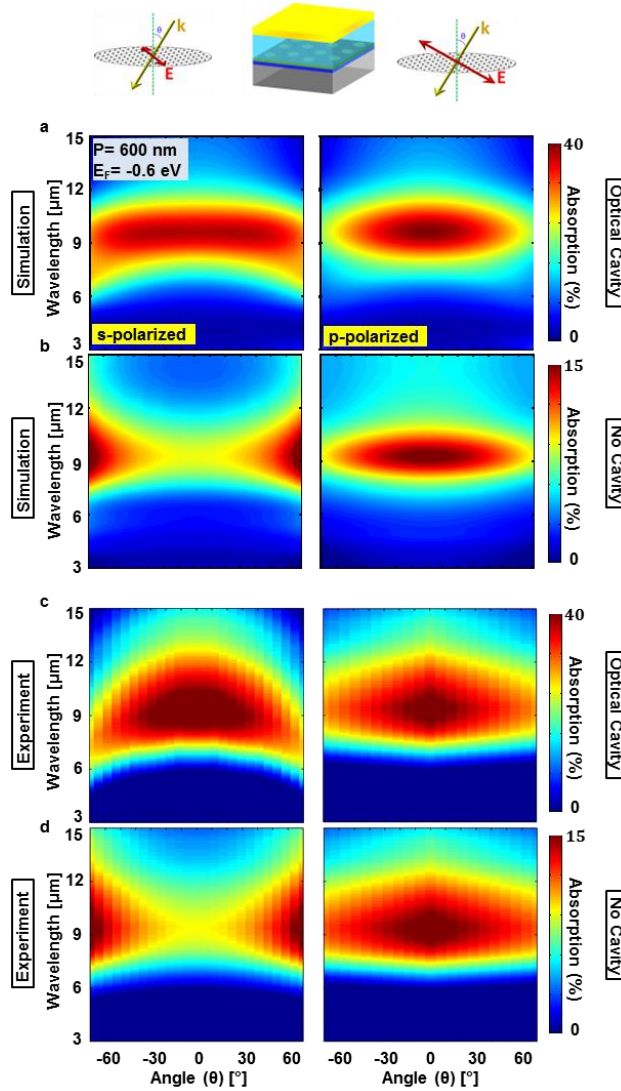


Figure 19: The absorption of angled incident light by the patterned graphene with nanohole array.

The simulated light absorption of s-polarized (left panel) and p-polarized (right panel) beam by the samples with (a) and without (b) cavity. The corresponding measured light absorption of s-polarized (left panel) and p-polarized (right panel) beam by the samples with (c) and without (d) cavity. The Fermi energy of the graphene samples is $E_F = -0.6 \text{ eV}$, $P = 600 \text{ nm}$ and $D = 400 \text{ nm}$.

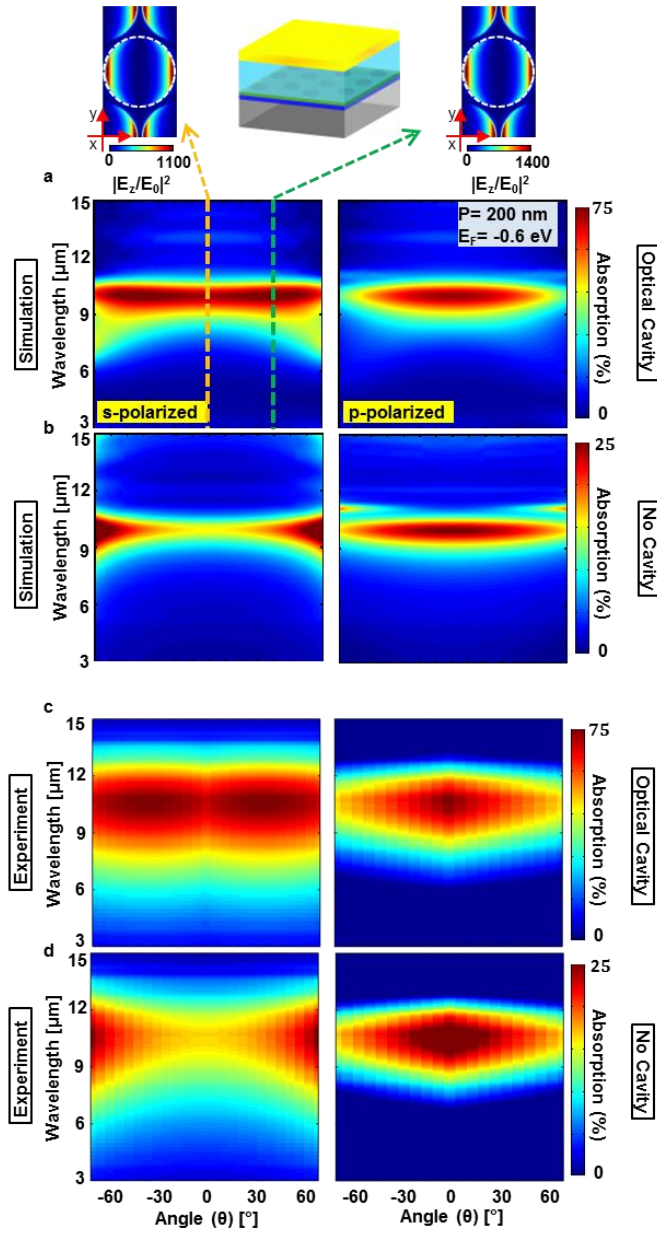


Figure 20: The absorption of angled incident light by the patterned graphene with nanodisk array.

The simulated light absorption of s-polarized (left panel) and p-polarized (right panel) beam by the samples with (a) and without (b) cavity. The z-component of the nearfield intensity at $\theta_i = 0^\circ$ (left) and $\theta_i = 50^\circ$ (right) of the s-polarized light are shown on top. The corresponding measured light absorption of s-polarized (left panel) and p-polarized (right panel) beam by the samples with (c) and without (d) cavity. The Fermi energy of the graphene samples is $E_F = -0.6 \text{ eV}$, $P = 600 \text{ nm}$ and $D = 400 \text{ nm}$.

The temporal and spatial interference between the optical cavity and the graphene plasmonic modes modifies the angular response such that for incident angles $\theta_i > 50^\circ$, destructive interference of the incident (\mathbf{E}_i) and reflected electric fields (\mathbf{E}_r) arising from phase difference lowers the light absorption, as shown in Figure 18c. Such behavior in the angular response of cavity-coupled absorbers for s-polarized light is not uncommon and was previously shown in a VO₂ based system [198]. The FDTD predictions are well supported by experimental data (shown in Figures 18-20) acquired using an integrating sphere coupled to a FTIR.

Effect of Light Polarization on the Angular Response

While the calculations by Thongrattanasiri *et. al.*, were done for ideal graphene with mobility of 10 000 cm²/Vs, I show that it can be extended to CVD grown low mobility graphene and successfully models the FDTD and experimental results discussed below. Using Equation. (24) to fit the FDTD results at normal incidence, I obtain $\hbar\kappa = 3.5 \times 10^{-2} eV / 6.9 \times 10^{-2} eV$ and $\hbar\kappa_r = 1.22 \times 10^{-4} eV / 4.5 \times 10^{-4} eV$ for the graphene nanodisk/nanohole array respectively (see Figure 22) which satisfies the criteria, $\kappa \gg \kappa_r$. Following that, the absorption of the patterned graphene for various incident angles can be calculated *via* the total light reflection coefficient ($\mathcal{R} = r_0 + \frac{r(1+r_0)^2}{(1-rr_0)}$) of the cavity-coupled patterned graphene ($A = 1 - |\mathcal{R}|^2$), where r_0 is the Fresnel reflection coefficient of the cavity spacer without graphene and the reflection coefficient of the patterned graphene is given by, $r = \pm iS/(\alpha^{-1} - G)$ for the arrays with periods much smaller than the wavelength ($P \ll \lambda$). The lattice sum for this condition is reduced to $G = 5.52/P^3 + i(S - 2(\omega/c)^3/3)$ for hexagonal array, where S is a polarization-dependent parameters, *i.e.* $S_s = 2\pi\omega/(cA \cos\theta_i)$, $S_p = 2\pi\omega \cos\theta_i/(cA)$ and A is the unit-cell area²⁷. The calculated peak absorption as a function of incident angle for s and p polarized light is overlaid on

the FDTD and experimentally obtained results as shown in Figure 21. Clearly a good agreement between the analytical, simulation and experimental data is evident. Figure 21 shows the maximum absorption for different incident angles at the resonance wavelength shown by the green dash line in Figure 18. The results of the unpolarized light (Figure 21-bottom) shows that the maximum light absorption of the graphene absorber is almost independent of the incident angle for $\theta_i \leq 50^\circ$.

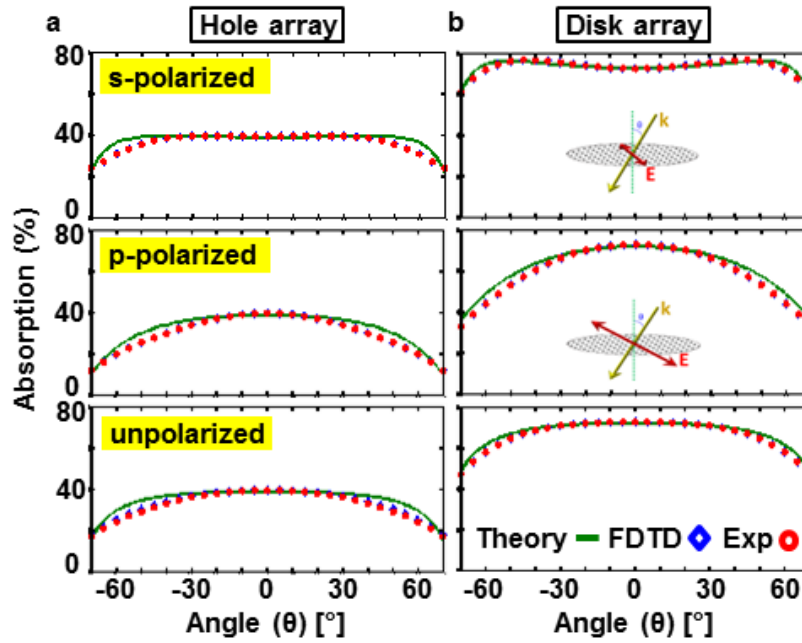


Figure 21: The angular response for the polarized and unpolarized lights.

Comparison of the analytical modeling, simulation and experimental results of s-polarized (top) and p-polarized (middle) and unpolarized (down) incident light for the graphene nanohole (a) and nanodisk (b) arrays with $E_F = -0.6$ eV. The polarized light measurements are normalized to the light intensity after the polarizer.

Plasmon Decay Rate

The decay rates which were used in the graphene polarizability α in Equation. (24) were extracted from the simulated extinction cross section per area for a single graphene nanodisk or nanohole and fitting the theoretical extinction cross-section $\sigma^{ext} = (4\pi\omega/c)Im\{\alpha(\omega)\}$ ⁹ to those curves, as shown in Figure 22. The plasmon decay rates show that the plasmon lifetime of the graphene nanodisk is higher than graphene nanohole.

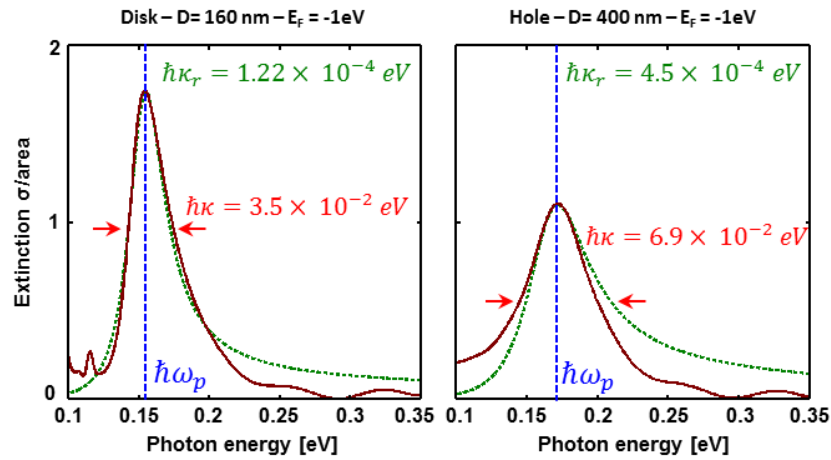


Figure 22: The plasmon decay rates.

The simulated extinction cross sections per area of a single graphene nanodisk with $D=160$ nm (a) and nanohole with $D=400$ nm at $E_F = -1$ eV were used to extract the radiative ($\hbar\kappa_r$) and total ($\hbar\kappa$) plasmon decay rates.

Conclusion

In conclusion, I have investigated infrared absorption in an optical cavity-coupled low carrier mobility ($\mu = 500$ cm²/V.s) CVD-grown graphene with hexagonal array of nanoholes and nanodisks in the infrared transparent 8 -12 μ m band. Due to the differences in the extinction cross-section of nanohole and nanodisks for the same diameter, the plasmonic excitation on their

respective edges are different, resulting in qualitatively dissimilar absorption peak profiles. A series of numerical simulations were performed to maximize infrared absorption by scanning over parameters like period and diameter for the hexagonal array of nanohole and nanodisks. The optimized devices exhibit an absorption of 60% for the nanohole array and up to 90% for nanodisk array when the Fermi level of graphene is increased to -1 eV by electrostatic p-doping. Such high absorption is attributed to strong plasmonic excitations at the patterned nano-edges where the localized electric field is amplified by factors of 500 for the nanohole and 1100 for the nanodisk arrays. For the Dirac plasmons excited by the incident light (8 -12 μm), the bulk states contribute mostly to the generation of hot carriers via Landau damping with little contribution from the edge states. The Fermi level of the patterned graphene is tuned by applying a voltage across a 15 nm thick layer of Al_2O_3 , which serves as a hard gate dielectric. The high-k Al_2O_3 is found to be more stable over time compared to the commonly used ionic-gel gate which tend to chemically degrade in few days. A dynamic spectral tunability of 2.46 μm for nanoholes and 1.11 μm for nanodisks is achieved. It is to be stressed that the use of industry standard Al_2O_3 for capacitive electrostatic gating in my devices makes it a potential candidate for integration with optical design boards unlike many previously reported device architectures that are bulky due to presence of ion-gel based components.

In my demonstration, I showed a 1 mm^2 area absorber which is considered large area, however, I believe that the total patterned area can be increased to centimeter scale by using techniques such as nanoimprint lithography. However, increase in the active area increases the gate leakage current resulting in inefficient electrostatic doping which is necessary to control the Fermi level for tunable absorption. Therefore, I envision an array of electrically isolated absorbers

spread over centimeter scale, each with reasonable ($< 1 \text{ mm}^2$) active area, operating in tandem similar to a pixelated detector array.

Finally, by using the optimal devices with highest absorption for nanoholes and nanodisks, I showed a systematic angle dependent ($0^\circ - 70^\circ$) optical study in the infrared domain. Although the LSPR frequency is independent of the incident angle of light, the evolution of peak absorption for s- and p-polarized light are qualitatively dissimilar, which is attributed to the different scattering cross-sections that the electric field of incident light interacts with on patterned graphene. However, the peak absorption for unpolarized light remains within 5% of its maximum up to $\theta_i \leq 50^\circ$, which suggests that both the nanoholes and nanodisk array can be operated over a wide range of angles. These angle dependent results provide experimental validation of the theoretical model for patterned graphene devices developed by Thongrattanasiri, *et al.* [46] based on coupled-dipole approximation. From an application point of view, the key difference between the nanohole/nanodisk arrays is the presence/absence of electrical continuity in graphene. Therefore, while the near perfect absorption of $\sim 90\%$ in the nanodisk array can be beneficial for application like wide angle optical modulators, tunable infrared camouflage, *etc.*, the nanohole array offers applicability in next generation wide band, wide angle photodetectors based on electron-hole pair generation by exciting electrostatically tunable plasmons.

The photodetection scheme based on the Dirac plasmon excitation is through non-radiative plasmon decay. Upon plasmonic excitation, there are different channels for non-radiative graphene plasmon decay which depends on the wavelength of the incident light. In the electromagnetic spectral region that the optical phonons of graphene and substrate are active, they can couple to the excited plasmon and transfer the energy of surface plasmon to the atomic lattices. This coupling increases the temperature of the device thereby making bolometric infrared detection possible.

Alternately, one can generate hot-carriers through phonon-assisted and boundary-assisted intraband Landau damping. The number of generated hot carrier which is a function of the Fermi energy of graphene and the perimeter of the holes/disks can be optimized to obtain enhanced electrical signal. Recent studies have attempted to utilize these approaches for detection, however, so far the measured output responsivities have suffered due to low optical absorption. I believe that the design for enhanced absorption presented in this study can help improve the detector performance significantly.

CHAPTER 4: INFRARED DETECTION BASED ON DIRAC PLASMON-ASSISTED HOT CARRIER GENERATION

Introduction

Two-dimensional (2D) materials like graphene has shown a lot of potential as a candidate material for photodetection. Several studies have demonstrated different routes to enhance spectrally tunable infrared light absorption in graphene [11, 12, 49, 195], however, attempts to realize infrared detection in the mid-wave infrared (MWIR 3- 5 μm) or the long-wave range (LWIR 8 -12 μm) have been poor compared to other commercial semiconductor-based detectors [31, 33, 70, 146, 199]. This low sensitivity is partly due to the inefficient conversion of the absorbed infrared light to electrical signal, which remains a major drawback due to the absence of bandgap and low thickness of monolayer graphene. Generally, bolometers rely on heating the graphene lattice which causes such detection processes slow and low sensitive [8, 33, 199-202]. In this view, a much faster (\sim ps) infrared detection process is to generate hot-carriers in absence of electron-phonon scattering [28, 30, 70] to rise up the electronic temperature of graphene for infrared sensing by using the photo-thermoelectric effect [48, 71, 72]. It is well-known that by shining light, the intrinsic electronic temperature of graphene increases (ΔT) by means of hot carrier generation that reveals as a Seebeck voltage (ΔV) [28, 30, 71, 203]. Despite the preliminary demonstrations, so far, because of the modest Seebeck coefficient of graphene $\sim 100\mu\text{V/K}$, it has not been possible to restrain this effect as an efficient approach that can rival current technologies [28, 70, 71].

The motivation of the present chapter is to identify new ways on how the temperature gradient (ΔT) of the graphene carriers can be engineered with negligible effect on the lattice

temperature in order to increase Seebeck voltage generation for high responsivity, spectrally tunable, ultrafast infrared detection in the long wavelength band at room temperature. The electronic temperature of graphene at a special spectral domain can be engineered by the plasmonic excitation of Dirac fermions which can be manipulated by electrostatic tuning of the Fermi energy. In the previous chapters, spectrally tunable infrared light absorption of ~60% in the 8 – 12 μm was shown for nanopatterned monolayer graphene coupled to an optical cavity [12]. By electrostatic doping of graphene, the permittivity is changed to shift the LSPR frequency [11, 37, 39, 44, 47, 195]. At resonance, because of the potent confinement of electric field at the discrete elements edges, the temperature of the electronic system of graphene rises by means of boundary-assisted intraband Landau damping to excite hot-carriers [48, 158]. Although, the hot-carrier generation leads to a change in the electrical conductance of graphene, the resultant photovoltage arising from the ΔT is restricted by the theoretical Seebeck coefficient of graphene. In this chapter, I present an unprecedented asymmetric plasmon-induced hot-carrier Seebeck photodetection strategy which overcomes the theoretical restrictions. In the asymmetric detector device, the active detector area contains a partially nanopatterned monolayer graphene, such that there exists a large temperature gradient between the hot carriers in the patterned and the unpatterned subregions, as shown in Figure 23. Apart from the temperature rise from intrinsic hot carrier generation in graphene through intraband transition, the plasmon-assisted hot carriers in the patterned region further increases the efficient ΔT across the source-drain contacts. The photodetector device performance is simulated using COMSOL which shows that there exists a large ΔT of 4.7K for the incident power of 155 nW that unveils as a high photo-thermoelectric voltage (0.44 mV) when combined with the ~ 60% infrared light absorption. Due to this record ΔT generation across a 10 μm asymmetrically nanopatterned graphene, the proposed LWIR detectors show a prominent room

temperature responsivity of 2900 V/W, D^* of 1.1×10^9 Jones together with an ultrafast time response of ~ 100 ns.

Plasmon assisted hot carrier generation

Asymmetric Photo-thermoelectric Effect

The plasmon assisted photo-thermoelectric (PTE) photodetector architecture and the basic electronic processes involved are schematically demonstrated in Figure 23. A monolayer graphene between the source and drain contacts creates the active detector area where a region of the graphene is patterned into a hexagonal array of holes. By doing this design, an asymmetry is inherently defined into the system that amplifies infrared detection as explained below. Selective patterning of graphene increases infrared absorption[11, 12] due to localized Dirac plasmon excitations from intraband transitions as shown in the band structure. The intraband transition for electrons above the Dirac point ($+\epsilon_F$) is same as the intraband transition for holes below the Dirac point ($-\epsilon_F$) due to the symmetry of the graphene linear band structure. As a result, a gradient is defined into the charge carrier density of the graphene channel along the source-drain contacts. This generates a temperature difference across the graphene channel that as I will discuss more in the next sections which plays the main role in infrared detection technique.

Applying the source-drain voltage (V_{SD}), henceforth named as bias voltage, and the gate voltage (V_G), generate multiple electronic processes act in favor or against each other that affect the detector response, as demonstrated by arrows in Figure 23a. The graphene channel width is selected to be $10 \mu\text{m}$ which is close to the diffusion length of the charge carriers[30]. However, in order to amplify carrier collection, the graphene channel width is increased to keep an effective active area of $2000 \mu\text{m}^2$ as represented in Figure 23b (left).

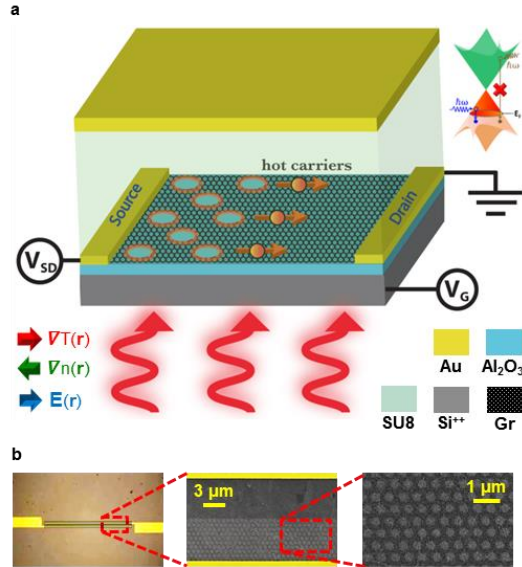


Figure 23: Graphene detector architecture.

(a) Schematic of the detector device architecture of the plasmon-assisted hot carrier creation on an asymmetrically nanopatterned graphene. Arrows at the bottom demonstrate different hot carrier diffusion processes. (b) The optical (left) and scanning electron microscope (middle and right) images of the half-patterned monolayer graphene device.

Comprehensive finite-difference time-domain (FDTD) simulations were done over varying period and hole diameter to magnify the infrared light absorption in the 8 – 12 μm band as can be seen in Figure 24 and explained in detail in the previous chapters. The optimized nanopattern geometry which was mentioned in chapter 3 [12], of period $P = 600 \text{ nm}$ and hole diameter $D = 400 \text{ nm}$ was selected in the detector designs.

Fabrication

The centimeter-scale monolayer graphene sheet grown by chemical vapor deposition (CVD) technique on copper flake was transferred on the Si^{++} (100 μm)/ Al_2O_3 (15 nm) substrate. The source and drain electrodes were fabricated by UV-lithography following by Ti/Au (3nm/60nm) deposition (Figure 23b-left). The EBL and oxygen-plasma etching approach were

used to nanopattern the half side of transferred monolayer graphene in a hexagonal array with period $P= 600$ nm and diameter $D= 400$ nm.

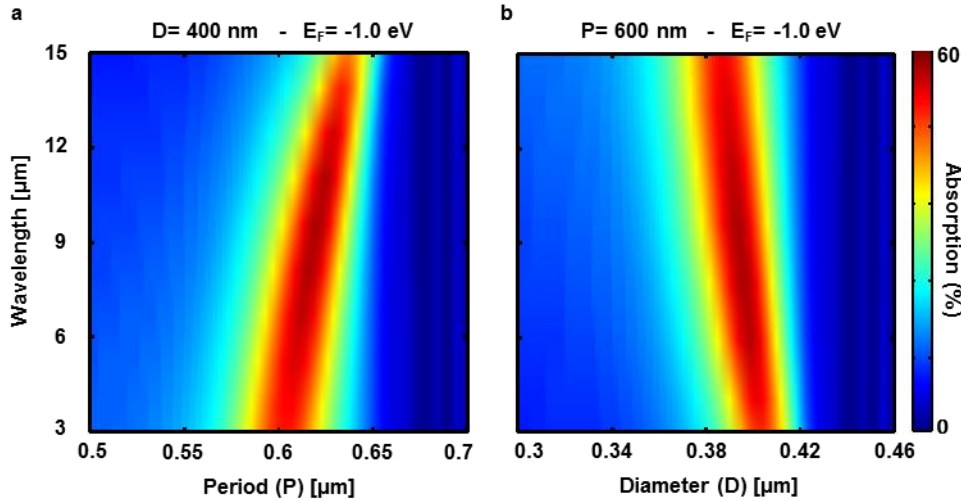


Figure 24: Light absorption maximization.

The light absorption spectra as a function period (a) diameter (b) for $E_F = -1.0$ eV.

Experimental Characterizations

The SEM images, shown in Figures 23b middle and right, demonstrate the hexagonal array of holes in the patterned region along the graphene channel. Raman spectroscopy was done on the transferred graphene to investigate if oxygen etching during the nanopatterning process changed the characteristic optical phonon peaks at ~ 1590 (the G peak) and ~ 2700 cm^{-1} (2D band) associated with monolayer graphene[204]. Figure 25 shows the Raman spectra of the pristine and nanopatterned graphene sheets which proves the absence of graphene oxide (GO) or reduced graphene oxide (RGO).

In the next step, the effect of nanopatterning on electrostatic doping was studied for half-patterned, full-patterned and unpatterned graphene channels. The changes of channel resistance as

a function of gate voltage was measured by a biasing electrical circuit for the three types of samples in Figure 26a.

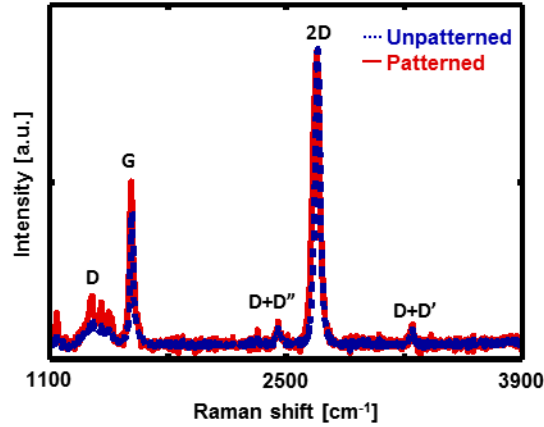


Figure 25: The Raman spectra of the graphene detectors.

The Raman spectra of the unpatterned and patterned monolayer graphene with zero gate voltage ($E_F = -0.6$ eV).

The Fermi level of graphene at 0V is determined to be 0.6 eV, as explained in chapter 3 which shows that the graphene sheet is self-doped to be p-type. Such self-doping effects have been reported in the other papers [196, 197] that happens due to the residual impurities on the graphene sheet. In addition, the Al_2O_3 gate dielectric is responsible to increase p-type doping in graphene [205, 206]. Therefore, as the gate voltage is altered from +1V to -2V, the hole density on graphene amplified consistent with a shift in Fermi energy from -0.55 eV to -1.0 eV. This results in a reduction in the channel resistance for all three cases (Figure 26a). The carrier mobility of graphene is found to be $500 \text{ cm}^2/\text{V}\cdot\text{s}$ for unpatterned channel, which reduces for the half-patterned case ($350 \text{ cm}^2/\text{V}\cdot\text{s}$) and is found to be the minimum for the full-patterned device ($250 \text{ cm}^2/\text{V}\cdot\text{s}$), as known for pattern-induced enhanced scattering. This clearly represents the role of nanopatterning on the electronic properties of graphene. Consequently, it is crucial to study how the thermoelectric

properties of graphene are changed due to nanopatterning. This will allow us to gain understanding into the fundamental process mechanism of the detector.

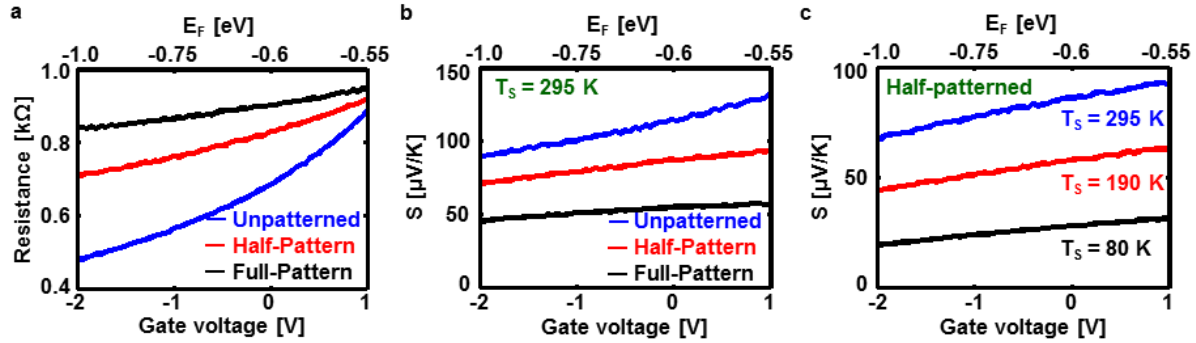


Figure 26: The electrical and thermoelectric properties of the graphene samples.

Electrical resistance (a) and Seebeck coefficient (b) of the unpatterned, half-patterned and full-patterned graphene samples ($P = 600$ nm and $D = 400$ nm) as a function of gate voltage (Fermi energy) at room temperature. (c) Seebeck coefficient of the half-patterned graphene sample as a function of gate voltage for different temperatures of the substrate.

Seebeck Coefficient Measurement

For 2D materials like graphene, it has been shown that the Seebeck coefficient (S) can be obtained using the Mott relation $S = (\pi^2 k_b^2 T / 3e) [d \ln(\sigma(E)) / dE]_{E=E_F}$ [30, 71], where K_b is the Boltzmann constant, T is the temperature and σ is the graphene electrical conductivity. By calculating the derivative of the electrical conductivity of the graphene channel from the experimentally measured curves ($[d \ln(\sigma(E)) / dE]_{E=E_F}$), the above equation was exploited to obtain the Seebeck coefficient for all three graphene samples (Figure 26b) as a function of Fermi level. The Seebeck coefficient for the full-patterned graphene sample is found to be the smallest while unpatterned graphene shows the highest Seebeck coefficient. It can be seen that by electronically enhancing the p-doping, as the Fermi level is lowered, the Seebeck coefficient

diminishes which is consistent with the other reports[69, 73] on graphene doped far from the CNP. At the end, I measure the temperature dependence of the Seebeck coefficient for the half-patterned graphene sample which is finally used for infrared detection. Figure 26c demonstrates the gate voltage dependence of S measured at different substrate temperatures in the range of 80 K – 300 K. The temperature dependent S of the half-patterned graphene sample follows a similar behavior to that reported for pristine graphene[69, 73], which proves that while the magnitude of S may have decreased as a result of nanopatterning (Figure 26b), the thermoelectric properties of the half-patterned graphene can be understood from the framework of pristine graphene. It can also be found that with decrease in temperature, S diminishes which makes the present detection mechanism more efficient at room temperature.

Photovoltage generation

Dirac Plasmon Decay

By illumination with infrared light, the electronic properties of the half-patterned graphene channel show contrasting electronic trend. When light is shined on the unpatterned region of the graphene channel coupled to an optical cavity (chapter 3), the light absorption is a low value of ~3%, however in the patterned area, due to Dirac LSP excitations, ~ 60% light is absorbed because of strong confinement of electric field near the nanohole edges (Figure 16)[12]. Figure 16 shows that the absorption peak wavelength was tunable over ~ 2.5 μm in the 8 – 12 μm band by electronical doping. Once excited, the LSPs loose energy through various damping pathways like phonon emission, bulk scattering or carrier-carrier edge scattering[1, 48, 158] that affect either the lattice or carrier temperature of graphene depending on which of the above-mentioned damping channels are predominant. Since the LSP resonances (115-155 meV) in our case happen at energies

lower than the optical phonon energy of graphene (200 meV)[204] and far from that of the substrate (~105 meV)[207], plasmon decay through emission of optical phonon has small effect[11, 30, 48, 208, 209]. Therefore, the probable pathway for the plasmon decay is by creation of hot carriers via edge scattering-assisted Landau damping and resistive loss due to plasmon-impurity scattering.

Nature of Generated Signal

Multiple processes now contribute to the asymmetric medium within the graphene channel that set the effective thermoelectric response of this complex device when illuminated with infrared light. First, there exists the photo-thermoelectric effect coming from the intrinsic Seebeck coefficient of graphene (S_I)[30, 70, 71, 73]. Second, the half-patterned graphene channel can be considered as a section consisting of two series connected thermoelectric materials with different Seebeck coefficients (Figure 2b) for the unpatterned (S_I) and patterned (S_2) regions which forces the system further into thermoelectric instability. The different Seebeck coefficients of the two sides enforce a directional photo-thermoelectric current assisted by the bias current. The consequent potential gradient can be described as a function of the channel width, $X_L - X_R$:

$$V_S = \int_{X_L}^{X_R} S(x) \frac{\partial T_{cr}(x)}{\partial x} dx,$$

where X_L and X_R are the locations of the left and right electrodes, respectively and T_{cr} is the temperature of the local carrier. Finally, the diversity in carrier mobilities of the patterned and unpatterned regions of the channel give rise to differential Joule heating during carrier transport, which more increases the thermal gradient in the system by enhancing the temperature-dependent Seebeck coefficients in the patterned and unpatterned sections.

FEM Simulation

The COMSOL Multiphysics 5.3a software was exploited to model the performance of the graphene detector by using finite element modeling (FEM). The final goal of simulations was to find the time dependent solution for the bias-dependent photo-thermoelectric current, which was further exploited to obtain the photo-thermoelectric voltage (V_{PTE}) and the responsivity $R=V_{PTE}/P_{inc}$. The built-in modules “Electric Currents” and “Heat Transfer in Solids” coupled with the multiphysics module “Thermoelectric Effect” were used to simulate the behavior of the detector.

The sample geometry in the simulations was same as the real detector except for the length of the simulated detector, which was reduced to $20\mu\text{m}$ as compared to $200\mu\text{m}$ in the experiment, in order to decrease the simulation time. The modeled detector was $20\mu\text{m}$ wide (electrodes and graphene sheet) and $20\mu\text{m}$ long. The channel width of detector was $10\mu\text{m}$ wide and $20\mu\text{m}$ long, where half of the width of the monolayer graphene sheet was nanopatterned, and the other half remained unpatterned. The gold electrodes were $5\mu\text{m}$ by $20\mu\text{m}$, and the thicknesses of graphene, gold electrodes, aluminum oxide, and silicon substrate were 0.5nm , 50nm , 15nm , and $3\mu\text{m}$, respectively. Gold, Silicon, and Aluminum oxide materials were directly inserted from COMSOL material library, while the experimentally obtained parameters were exploited for graphene. The electrical conductivity and Seebeck coefficient were gate voltage-dependent for graphene, obtained experimentally for both the patterned and unpatterned graphene, separately. The temperature independent electrical conductivity was exploited for all materials to remove the bolometric roles in the photoresponse.

The bias voltage was used across the gold electrodes; one side was set to ground, and the other side kept at high potential. Except gold contacts and graphene, everything was set electrically

insulated. The current conservation boundary condition was used for the whole structure, and the initial values were put to $V=0$. In order to consider the contact resistance, extra electrical contacts were defined between gold and graphene. The heat flux was used in the form of rectangular pulse of period 4ms, which means for the initial two milliseconds the heat flux was zero, corresponding to the dark mode in the experiment. For the next two milliseconds, nonzero heat flux was used on the patterned section of graphene through laser heating. A Gaussian light beam with the spot size $R_{\text{spot}} = 2\text{mm}$ and the incident power $P_{\text{inc}}=153 \text{ nW}$ was applied. The absorbed heat flux depended on the light absorption at different Fermi energies. The gate voltage dependence of the light absorption was obtained by using the Lumerical FDTD software, which changed from $A=34\%$ at $E_F = -0.55\text{eV}$ to $A=60\%$ at $E_F = -1.0\text{eV}$ for the patterned graphene, as discussed by details in chapter 3.

The bottom part of the detector device was kept at a constant temperature using the boundary condition “temperature” in the software. The initial value of the temperature was put to $T_0=293.15\text{K}$, and the boundary condition “open boundary” was applied across all the sides of the detector device, except the top and bottom surfaces which means the heat flux can flow inside or outside across the cross-sectional boundary depending on the medium temperature. Thermal contacts were put between graphene, aluminum oxide, and silicon to engineer the heat transfer in the vertical direction. The free tetrahedral meshing for gold and the free triangular meshing for the graphene sheet were applied, which were swept in the vertical direction for the entire geometry.

The time dependent solver with very low relative tolerance of 10^{-5} was exploited to simulate the time dependent thermoelectric photovoltage across the electrodes for different Fermi levels. The dark and light thermoelectric voltages $V_{\text{TE,D}}$ and $V_{\text{TE,L}}$ were obtained in absence and presence of the incident light, respectively. The photo-thermoelectric voltage V_{PTE} was then obtained by

subtracting the dark from the light voltage, i.e. $V_{PTE} = V_{TE, L} - V_{TE, D}$. As seen from Figure 27, the COMSOL simulation results are in excellent agreement with the experimentally derived Seebeck voltage V_{PTE} as a function of gate voltage and bias voltage.

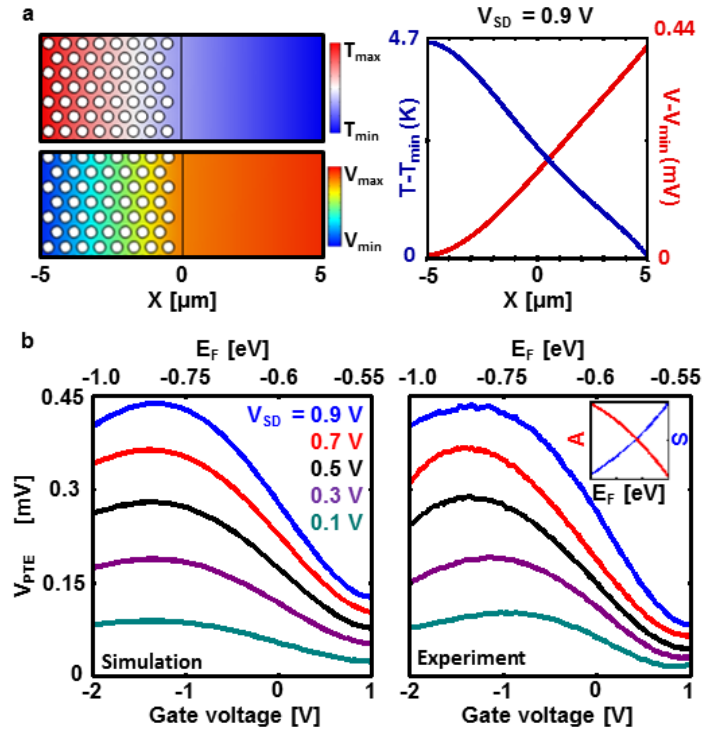


Figure 27: FEM simulation results.

(a) The simulated temperature (top-left) and electrical potential (bottom-left) profiles of the graphene detector at $E_F = -0.85$ eV, $\lambda_{res} = 8.15$ μm and $V_{SD} = 0.9$ V. (Right) The temperature and potential as a function of position (X) at a constant Y position. (b) The simulated (left) and measured (right) D.C responsivity of the graphene detector device as a function of Fermi energy for the different bias voltages. (Inset) The light absorption (A) and Seebeck coefficient (S) as a function of Fermi level.

Comparison of FEM Simulation and Experimental Results

Taking the mentioned factors into consideration, FEM was used at 295 K using COMSOL software that showed that a net temperature difference of $\Delta T \sim 4.7\text{K}$ (for the incident light power of 155 nW) where the patterned region has enhanced temperature as can be observed in Fig. 27a.

This ΔT across the graphene channel gave a photo-thermoelectric voltage V_{PTE} of ~ 0.44 mV. During the modeling, the Fermi energy of graphene was kept at -0.8 eV, and a bias voltage $V_{SD} = 0.9$ V was used. Due to the biasing, both plasmon-assisted thermoelectric and bolometric effects play a part in to the resultant D.C photoresponse of the graphene channel. In order to investigate only the photo-thermoelectric voltage, a specific measurement strategy was exploited that removed bolometric effects from the signal.

Figure 27a-right shows the simulated profile of ΔT and V_{PTE} acquired across the graphene channel. It is to be noted that creation of such a large position-dependent ΔT at room temperature exceeds previously reported numbers by an order of magnitude[28, 70, 71], thereby providing the novelty of the proposed detection concept. A series of FEM simulations were done to probe the effect of Fermi energy and bias voltage on the photo-thermoelectric signal (Figure 27b-left). It can be seen that by enhancing the bias voltage, the hot-carriers transport increases substantially such that V_{PTE} amplifies due to efficient carrier collection at the contacts. However, the maximum amount of this bias voltage is restricted by the breakdown electrical current density of graphene[210] which in this case is 12 A/cm², hence, 0.9 V was selected as the upper limit for the bias voltage for an active graphene detector area of 2000 μm^2 . Interestingly, for any bias voltage, as the Fermi level of the graphene channel is enhanced from -0.55 eV to -0.8 eV, the photo-thermoelectric voltage amplified and then reduces for higher Fermi energies. This can be interpreted as follows: as demonstrated in Figure 27b-right (inset), the dependence of the light absorption $A(E_F)$ and Seebeck coefficient $S(E_F)$ as a function of Fermi level show opposite behaviors that finally dictates the value of V_{PTE} . As explained earlier, increase in the Fermi level amplifies the light absorption due to the expansion of available states for intraband transition which enhances hot-carrier creation, or ΔT , and also amplifies the electrical conductivity of graphene,

which enhances the Seebeck voltage V_{PTE} ; however, the resultant V_{PTE} is in addition a function of Seebeck coefficient ($V_{PTE} = S(E_F) \Delta T$) which monotonically reduces with E_F . Considering these competing processes effects, there is a trade-off where after a threshold Fermi level (~ -0.8 eV), the role of increased ΔT on V_{PTE} is negatively impacted by the smaller Seebeck coefficient that results in a reduction in V_{PTE} . Therefore, there is an optimized interval of gate (V_G) and bias voltage (V_{SD}) for the best efficiency of the graphene detector associated with maximum V_{PTE} at a favorite spectral wavelength which can be seen from Figure 27b. The results of the FEM simulations were confirmed by doing experimental measurements to quantify the photo-thermoelectric voltage produced as a function of bias and gate voltages (Figure 27b-right). Photoresponse of the graphene detector was measured by shining the active area with a broadband light source. An optical bandpass filter is exploited to remove other wavelengths outside of the 8-12 μm region from the broadband incident light. In addition, due to the fact that the Fermi energies of the patterned and unpatterned graphene are approximately same, the contribution from the photovoltaic effect to the photoresponse is negligible [51]. The experimental diagrams are in a very good agreement with the simulated results, which proves that the measured signal generates from the Seebeck effect.

D.C photoresponse

D.C Photo-thermoelectric Voltage Measurement

For a constant gate voltage, a D.C bias voltage (V_{SD}) was used across the source-drain (SD) electrodes and the resultant current $I_1 = I_B + I_{TE}$ and $I_2 = -I_B + I_{TE}$ were measured for applied voltage $\pm V_{SD}$, where I_B is the electrical current created by the bias voltage and I_{TE} is the thermoelectric current ($I_{TE} = (I_1 + I_2)/2$). This thermoelectric current was obtained in dark (I_{TE-D}) and in the presence of mid-IR light (I_{TE-L}). Any contribution related to the bolometric effect is

independent of the polarity of the applied bias voltage, which was thereby omitted in the I_{TE-L} calculation. Therefore, the photo-thermoelectric current and voltage can be obtained as $I_{PTE} = I_{TE-L} - I_{TE-D}$ and, $V_{PTE} = R_G I_{PTE}$ where R_G is the graphene channel electrical resistance, respectively. The circuit diagram is shown in Figure 28.

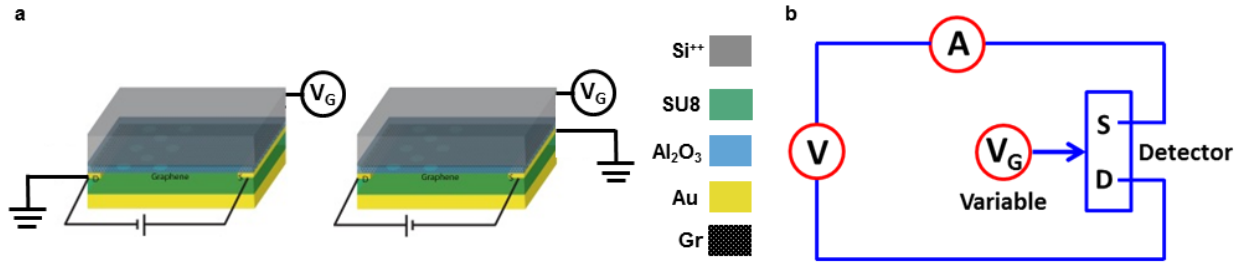


Figure 28: Circuit diagram of the D.C measurement.

(a) The schematic of the circuits used to measure the D.C currents correspond to the bias voltages with opposite polarities. (b) The circuit used to measure D.C response.

Functionality of the D.C Responsivity

The room temperature D.C behavior of the detector was determined by the responsivity ($\mathcal{R}_{D.C} = V_{PTE} / P_{inc}$) for different bias voltages (V_{SD}) and substrate temperatures (T_s), where P_{inc} is the incident IR power after bandpass filter. So far, the largest reported responsivity at room temperature for the graphene-based detectors is 10V/W [71], where a photo-thermoelectric process was excited by applying different metal electrodes on monolayer graphene. In comparison, the largest responsivity obtained in my work is 2.9×10^3 V/W, as shown in Figure 29, which is more than two orders of magnitude higher than the previous reports. Figure 29a demonstrates the combined bolometric and the photo-thermoelectric response where the total responsivity enhances by 30% above the photo-thermoelectric mechanism alone. The responsivity follows the identical

behavior as V_{PTE} and scales linearly with the inserted bias voltage for both thermoelectric and combined thermoelectric-bolometric photoresponses (Figure 29b).

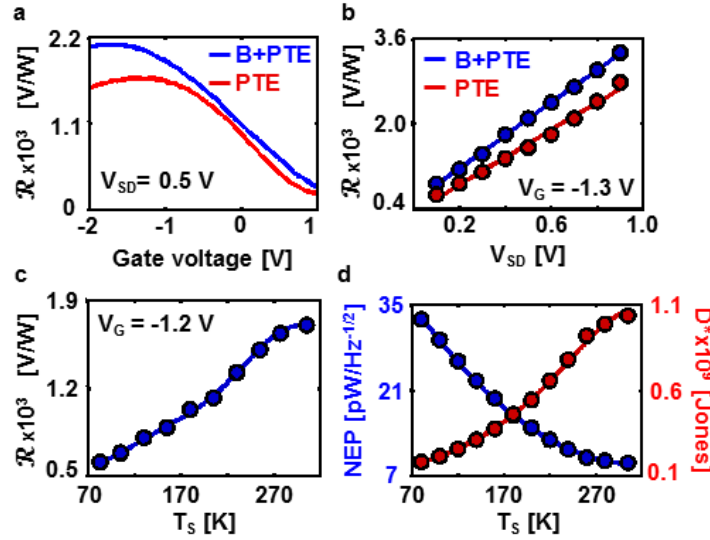


Figure 29: The trend of D.C responsivity.

(a) D.C responsivity resulted from photo-thermoelectric (red) and combined photo-thermoelectric and bolometric (blue) effects as a function of gate voltage (Fermi energy) at room temperature and $V_{SD} = 0.5$ V. (b) D.C responsivity of the detector as a function of bias voltage for gate voltage, $V_G = -1.3$ V. (c) D.C responsivity as a function of detector temperature for gate voltage, $V_G = -1.2$ V. (d) The figure of merits, noise equivalent power (NEP) and specific detectivity (D^*) of the half-patterned graphene detector as a function of the detector temperature. (B stands for Bolometric, and PTE means Photo-thermoelectric)

Next, the role of ambient temperature on the photoresponse of the photodetector was probed, where $\mathcal{R}(V_G)$ curves were measured at normal temperature intervals within the range of 80 – 320 K. As the temperature is lowered, the responsivity diminishes as demonstrated in Figures 29c. This is opposite to the bolometers where cooling enhances responsivity[21, 70, 202]. In the proposed detector device, the light absorption is approximately independent of temperature, in other words, the hot-carrier production and subsequent generation of ΔT remains unaffected by the temperature of the detector. However, the Seebeck coefficient of graphene reduces as the

temperature is decreased (Figure 29c); as a result, for the same ΔT , the value of V_{PTE} diminishes gradually from 320 K to 80 K. Therefore, the responsivity of the detector weakens as the temperature is decreased which provides additional proof that Seebeck effect is certainly the predominant phenomenon in the proposed detection mechanism.

Noise Equivalent Power

NEP is another important factor of a photodetector where a smaller NEP value is attributed to larger sensitivity of a detector [67, 68]. NEP is obtained by measuring the noise spectral density (S_n) and the responsivity ($NEP = S_n / \mathcal{R}$) of the photodetector for different sample temperatures (Figure 29d). Usually, thermal photodetectors suffer from large NEP at room temperature which is the reason they are cooled for better efficiency [21]. In contrast, as demonstrated in Figure 29d the proposed photodetector shows the lowest NEP at room temperature and an enhance in NEP is observed upon decreasing the sample temperature. The NEP of the present photodetector (~ 7 pW/Hz^{-1/2}) is more than one order of magnitude smaller than thermal photodetectors[21, 70] which demonstrates its superiority as an uncooled, room-temperature mid-IR photodetector. The specific detectivity (D^*) is obtained by the NEP and the detector active area (A) as $D^* = \sqrt{A}/NEP$ [$cm \sqrt{HZ}/W$] or [Jones]. The maximum D^* at $E_F = -0.8$ eV and $V_{SD} = 0.9$ V is found to be 1.1×10^9 Jones (Figure 29d) which clearly surpass all graphene-based MIR photodetectors reported earlier [20, 21, 28, 31, 33, 70-72, 146, 199-203, 211].

A.C photoresponse

A.C Photoresponse Measurement

The circuit design for A.C photoresponse is demonstrated in Figure 30. In the measurement setup the detector device was put in front of a broadband blackbody source with a 8 – 12 μm

bandpass filter in between. The Fermi energy of graphene was kept constant by applying a fixed gate voltage. First, a sinusoidal bias voltage with a positive offset of 0.25 V was used in the dark mode to the source – drain electrodes. Due to this time dependent bias, an A.C voltage was induced across resistor R_2 that was at the same frequency as the inserted bias voltage [$V_{SD+}^{dark} = 0.25 + \sin(2\pi f)$].

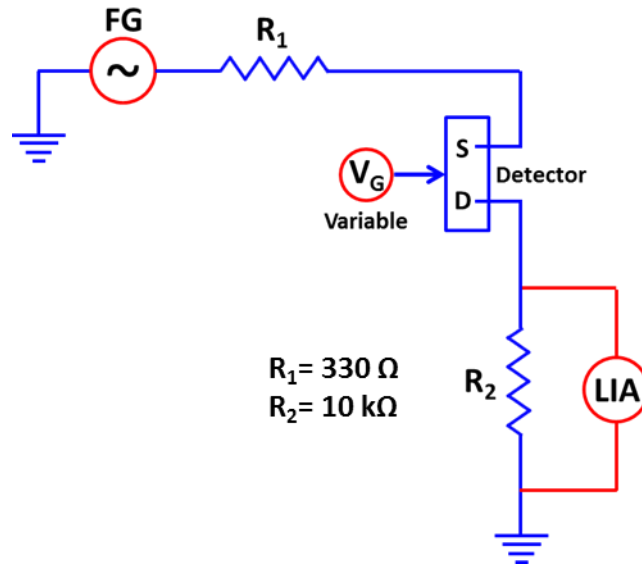


Figure 30: Circuit design of the AC measurement.

The voltage across R_2 was measured by using a lock-in-amplifier. In the next step, in the presence of incident light, the voltage across R_2 [V_{SD+}^{light}] was recorded. The A.C photovoltage was obtained by taking the difference [$V_{SD+}^{PV} = V_{SD+}^{light} - V_{SD+}^{dark}$]. The voltage V_{SD+}^{PV} comprises the photoresponse from both photo-thermoelectric and photoconductive processes. Therefore, similar to the D.C responsivity measurement mechanism, in order to remove the photoconductive contribution the A.C photovoltage (V_{SD-}^{PV}) was recorded for a negative offset bias voltage and the subtraction $V_{SD+}^{PV} - V_{SD-}^{PV}$ gives the A.C photo-thermoelectric voltage which is shown in Figure 31.

Nanopatterning Effects on the Photoresponse

To further illustrate the effect of LSPs in hot carrier generation and how the proposed asymmetric system excels in producing a high responsivity detector, I compare the A.C photoresponse of three detectors that were designed with (i) half-patterned, (ii) full-patterned and (iii) unpatterned graphene channels, respectively.

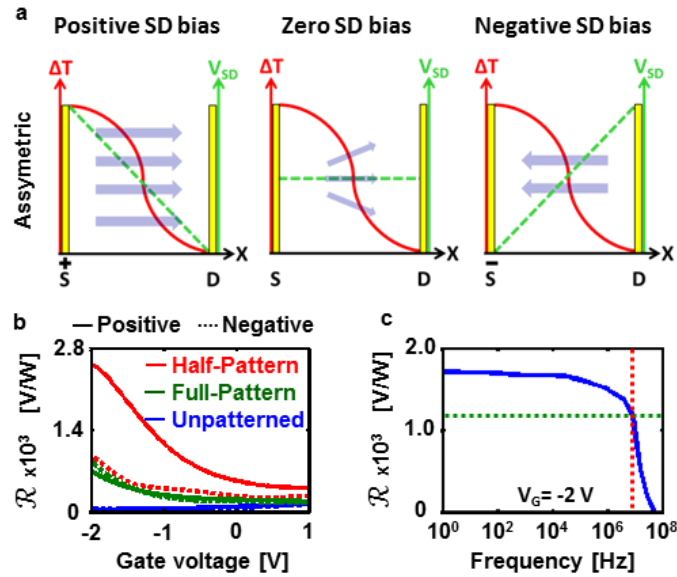


Figure 31: The effect of nanopatterning and the response time.

(a) The schematic demonstrates the A.C photocurrent for different measurement cases. (b) A.C responsivity values of the half-patterned (red), full-patterned (green) and unpatterned (blue) graphene photodetectors for the positive (solid) and negative (dashed) offsets (0.25 V) at circuit frequency $f = 20$ Hz. (c) A.C responsivity values as a function of circuit frequency for $V_G = -2$ V. The crosshair demonstrated in dashed lines corresponds to the cut-off frequency.

I claim that for the unpatterned and full-patterned detectors, the photoresponse essentially generated from the bolometric effect. In addition, due to the symmetric design of the unpatterned and full-patterned detectors, it is predicted that the polarity of bias voltage should not change the photoresponse. In the opposite way, due to the asymmetric design of the half-patterned detector, a

bias voltage in the direction of ΔT supports the collection of hot-carriers compared to the opposite direction bias. For the zero-bias situation, the asymmetric case is predicted to generate a finite photoresponse, however, the symmetric devices should give zero photoresponse due to the omnidirectional scattering of hot carriers. Figure 31a schematically shows my hypotheses that were examined by the following measurements. The experimentally recorded responsivity at $f = 20\text{Hz}$ demonstrated in Figure 31b proves the working hypothesis. The full-patterned detector device demonstrated larger responsivity than the unpatterned case, which is attributed to the amplified infrared absorption. On the other hand, the half-patterned device generated significantly larger responsivity created from higher ΔT across the graphene channel. Moreover, it can be found that the polarity of bias voltage has essential role on the responsivity of the half-patterned detector device unlike the symmetric full-patterned and unpatterned devices. As mentioned earlier, the positive bias condition (source voltage: 0 to 0.5V) helps the drift of the hot-carriers (holes) generated on the patterned region towards the drain (ground), whereas in the negative bias mode (source voltage: 0 to -0.5 V), the flow of holes unto the drain (ground) is banned gives rise to lowered responsivity as shown in Figure 31b.

Response Time

The time response of the half-patterned detector was recorded to characterize the operational bandwidth. Due to the ultrafast Dirac plasmonic excitation and moreover charge transport in monolayer graphene, an ultrafast photoresponse is predicted [48]. Since, light modulation by using a mechanical chopping mechanism was not a doable technique for high speed measurements, I pursued an alternate approach to study the A.C photoresponse by electronic modulation of the source-drain bias voltage, as discussed in the previous section with a circuit frequency from 200 Hz to 100 MHz. The corresponding A.C responsivity as a function of circuit

frequency is demonstrated in Figure 31c. I observed a steady responsivity up to 8 MHz corresponding to a 3dB cut-off response time of $\tau_{\text{res}}=125$ ns. It is important to mention that the measured response time is larger than the Dirac plasmon lifetime ($\sim 10^{-15}$ sec) and is restricted by the capacitance of the external measurement circuitry [67].

Single-pixel imaging

The proposed asymmetric graphene detector device is a multispectral gate voltage tunable infrared detector. This opens up the possibility for making an uncooled multi-pixel infrared camera with a performance comparable to the commercial cooled cameras. To demonstrate the real performance of the photodetector, a single-pixel imaging method [212] was exploited to image a Pegasus and UCF logo made on a sapphire substrate. A special measurement setup was used for the single-pixel imaging, as shown in Figure . The results in greyscale are demonstrated in Figure 33 for different gate voltages. As mentioned earlier, the photo-thermoelectric voltage is a decreasing function of gate voltage ($V_G > -1.5$ V) or E_F ($E_F > -0.8$ V). The resultant image contrast from the single-pixel photodetector is a function of the gate voltage, as shown in Figure 33 that validates the active tuning ability of the proposed graphene photodetector.

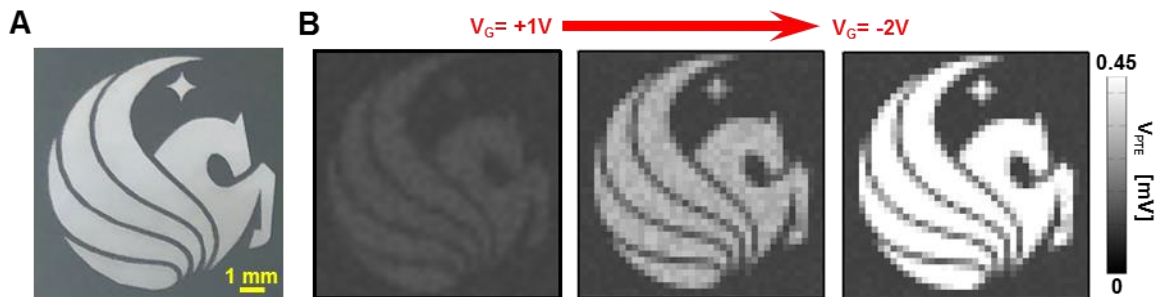


Figure 32: Single-pixel imaging.

(a) The schematic of the single-pixel imaging setup. (b) The results of imaging.

Conclusion

In conclusion, this chapter demonstrates a distinguished room temperature photodetection mechanism using 2D monolayer graphene that is feasible by the interaction between several physical phenomena: (i) tunable amplified infrared absorption provided by localized Dirac plasmonic excitations, (ii) graphene carrier mobility engineering and (iii) excitation of asymmetric hot carriers and resultant electronic photo-thermoelectric process. The unprecedented asymmetric graphene channel design made generation of high temperature gradient possible ($\Delta T \sim 4.7\text{K}$, $P_{\text{in}} = 155 \text{ nW}$) which is essential to the notable photoresponse. I recognized different processes contributing to the photoresponse and mentioned conclusive proofs that the ultrafast ($\tau_{\text{res}} \sim 100 \text{ ns}$), high responsivity (2900 V/W) and high $D^* \sim 1.1 \times 10^9 \text{ Jones}$ are attributed to the photo-thermoelectric effect. The usage of CVD-grown monolayer graphene as the active material of the infrared detector, provides scalability to focal plane arrays vital for lightweight, high responsivity, uncooled and low cost LWIR infrared cameras. In addition, my photodetector design and selection of constituent materials favor direct integration with the developed silicon based ROIC, unlike other mechanisms using polymers or materials that require heterojunction epitaxial growth on specific substrates for working. The proposed frequency-tunable graphene photodetector not only presents spectroscopic detection but also pave the path towards dynamic multi-spectral imaging in the infrared region, which is absent in the present infrared imaging technologies.

CHAPTER 5: SURFACE PLASMON EXCITATION ON QUASI-3D NANOSTRUCTURES

Published at <https://www.osapublishing.org/ol/abstract.cfm?uri=ol-43-24-6001> on 11 December 2018 by Optics Letters. DOI: <https://doi.org/10.1364/OL.43.006001>, Alireza Safaei, Sushrut Modak, Abraham Vázquez-Guardado, Daniel Franklin, Debashis Chanda

Introduction

Subwavelength metal-dielectric resonators are excellent tools to enhance the light-matter interaction or control the phase of forward or backward scattering via local plasma oscillations [10, 17] This is a direct result of enhancement of electric field at the surface plasmon resonance frequency which inherently depends on metal and dielectric optical properties and the geometry of the system [1, 24]. Such a unique properties offer a rich and broad gamut of applications, such as surface enhanced Raman spectroscopy (SERS) [161], biosensing [213] and flat optics [10, 17]. Furthermore, these systems also allow fundamental physics study and understanding, such as cavity quantum electrodynamics [214, 215], energy transfer [216] and superchiral light generation [217]. One of the disadvantages of surface plasmons is the inherent short lifetime resulted in broad resonance spectrum due to the damped electron oscillations in the metals [158, 218]. Coupling of plasmonic structures to the systems with narrow resonances is one route to reduce the resonance bandwidth which has been achieved by optical cavity coupling [6, 11, 23, 161], free space coupling [219, 220], higher order plasmon resonance coupling [221], and coupling to Fano resonances [222].

Out of these methods, the photonic cavity resonant coupling has shown many interesting phenomena such as amplified spontaneous emission [223], plasmon-cavity mode splitting [6, 7, 224], narrowband infrared radiation source [225], and efficient light trapping for solar cells [226, 227]. All of

these were based on excitation of natural plasmon resonance and its coherent interaction with the cavity. Prior works theoretically showed perfect absorption in coupled metal/dielectric systems [228-230].

Here, a cavity-assisted surface plasmon excitation on hole/disk array has been used to trap the incident photons which subsequently get absorbed as plasma loss. We show that the extraordinary transmission through the hole-disk system leads to ‘funneling’ of photons when coupled with an optical cavity. The cavity-induced and geometrically tunable funneling of photons through a subwavelength aperture ($\lambda \gg \text{diameter}(D)$) leads to complete light absorption. This cavity-coupled hole-disk array behaves as a multi-resonance system in the other two wavelength regimes ($\lambda \sim D$ and $\lambda \ll D$) as reported in our earlier works [6, 161] which was based on excitation of natural plasmon resonance in the visible spectral range (0.5-1.2 μm) and its coherent interaction with the cavity, the physics of which is completely different compared to the present manuscript. However, in the subwavelength regime ($\lambda \gg D$) the complimentary aperture pair, a hole and disk, when driven in-phase by the cavity to excite cavity-induced hybrid surface plasmons funnels $\sim 100\%$ of the incident photons through the subwavelength aperture. For given disk and aperture dimensions, the peak absorption wavelength is tunable across a wide spectral range with the cavity phase.

There are two types of interaction between the optical cavity mode and the plasmonic mode. The first interaction type is related to the natural plasmonic modes of the hole-disk array which happens in the visible-near infrared wavelength regime where LSPR depends solely on the geometrical parameters of the array. The coherent interaction of the plasmonic and cavity modes hybridizes resonance mode and splits the absorption peak frequency [6, 11, 12, 161]. Another interaction happens far from the natural LSPR, imposed by the fundamental cavity resonant mode which depends on the cavity phase [217]. Placing the disk array in the antinodes locations of the cavity excites the surface plasmon via the spatial coupling between these two modes. Since the frequency of the trapped light excites the localized surface plasmon

on the disk array, the LSP mode temporally coupled in-phase to the cavity mode. This strong coupling of the cavity and LSP mode and the very narrow bandwidth of the fundamental cavity resonance induces spectral narrowing of the perfect absorption of light [3].

At present all cooled and uncooled mid-IR detectors being “bucket” detectors generate integrated spectral images in binary color formats (choices of any two pseudo colors) eliminating the spectral information. Also, the narrowband infrared absorption spectroscopy has proven to be a very important tool in the detection and identification of airborne chemicals where pattern recognition is used as a post processing step to compare the infrared spectrum of library molecules against the infrared spectra of airborne contaminants [8, 231]. Present broadband detectors are not sensitive enough to perform low concentration chemical detection from IR radiation. In particular, detection sensitivity of microbolometer arrays operating in the mid-IR region is limited by the black-body radiation limit. To date very little research work has been performed on frequency selective uncooled devices. In this context the proposed narrowband absorber paves the path for frequency selective detection of infrared radiation. In order to demonstrate the feasibility, we designed and fabricated 3 spectrally de-tuned detectors and reported as a separate publication [9, 232].

Light coupling

Quasi-3D Nanostructure Design

A 3D cartoon of the cavity-coupled hole-disk system is shown in Figure 33a. The square array of hole-disk has a period P , diameter D and the separation between the hole-array and disk-array is RD (relief-depth). The height of the cavity, measured from the surface of mirror at the bottom to the top hole-array is C . The thickness of gold for the hole and disk array is kept constant at 30 nm, and for back mirror it is kept constant (200 nm) as shown in Figure 33b. The cavity spacer dielectric has refractive index of 1.56. The absorption spectrum of the tri-layer system is shown in Figure 33c for the parameters $P = 1.14$

μm , $D = 0.76 \mu\text{m}$, $RD = 280 \text{ nm}$ and $C = 0.87 \mu\text{m}$. A cross-sectional electric field in the structure at the resonance wavelength ($\lambda = 4.4 \mu\text{m}$) is shown in the inset of Figure 33c. The underlying mechanism of absorption can be understood by analyzing the resonant coupling between the constituents in the structure, namely hole-disk coupling, disk-disk coupling and moreover, the cavity and disk-array coupling. Cavity-coupled disk array absorbs less than 10% of incident light, as shown in Figure 33c which highlights the role of hole-disk coupling in the photon trapping. The angular response of the absorber using rigorous coupled wave analysis (RCWA) approach and experimental measurement shows the perfect absorption up to $\theta_{\text{inc}} = 45^\circ$ has less than 20% change [232].

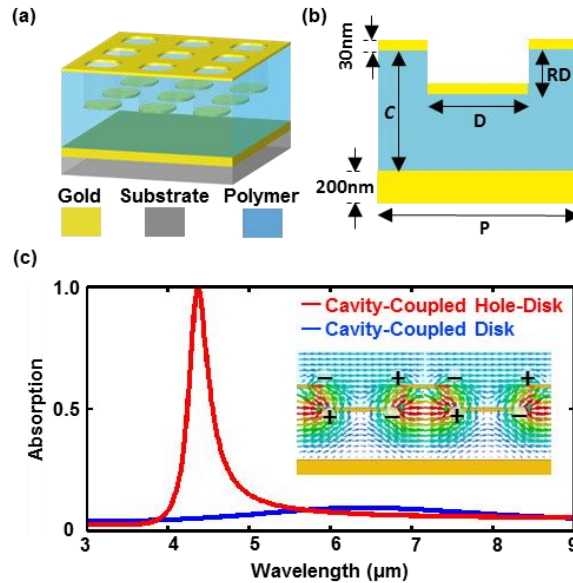


Figure 33: The light absorption of the quasi-3D nanostructure.

(a) 3D (b) cross-sectional (unit cell) schematics of the cavity-coupled hole-disk system. (c) Simulated (FDTD) light absorption in the cavity-coupled hole-disk array of period $P = 1.14 \mu\text{m}$, side $D = 0.76 \mu\text{m}$, $C = 870 \text{ nm}$ and relief depth $RD = 280 \text{ nm}$. Inset: Computed electric field distribution inside the structure at resonance.

The Effect of Quality Factor of the Optical Cavity

Since the surface plasmon on the disk array is excited by the fundamental cavity resonant mode, its spectral bandwidth depends on the FWHM of the optical cavity. Higher Q-factor of the cavity induces narrower absorption bandwidth. To show the role of cavity in the narrowing of the bandwidth, we simulated the absorber system for different back mirror thicknesses (0-20 nm). As shown in Figures 34a-c, with the decrease in the back-mirror thickness, the Q of the cavity reduces, resulting in both higher FWHM and reflection.

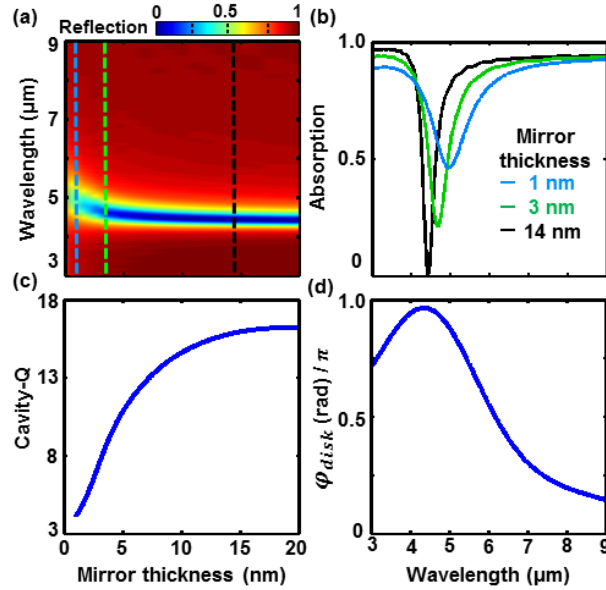


Figure 34: The optical properties of the cavity and metasurface.

(a) The reflection spectra as a function of wavelength and thickness of back mirror. (b) The reflection spectra for different back-mirror thicknesses as indicated in (a) by the dashed lines. (c) The Q factor of the cavity-coupled absorber as a function of the back-mirror thickness. (d) The phase shift of the transmitted electric field through the disk array.

Figure 34d shows the phase shift of the transmitted light imposed by the disk array from FDTD simulation. Most of the radiated energy from the disk in the upward direction is reflected back from the hole-array, due to the subwavelength hole diameter, which acquires a phase shift of

$\Delta\varphi \approx \pi$ during reflection [6]. The reflected field by passing through the disk array gathers another phase shift (φ_{disk}) like Figure 34d. It means the reflected field acquires a total phase of $\varphi_{ref} = 2\varphi_{disk} + \pi$ which is in-phase with the downward radiation ($\varphi_{trans} = \varphi_{disk}$) over the spectral bandwidth $\lambda = 3 \mu m - 5 \mu m$, $\varphi_{disk} \approx \pi$ resulting in constructive interference ($\varphi_{ref} = \varphi_{disk} + 2\pi$) and the transmission peak (blue) as seen in Figure 35a.

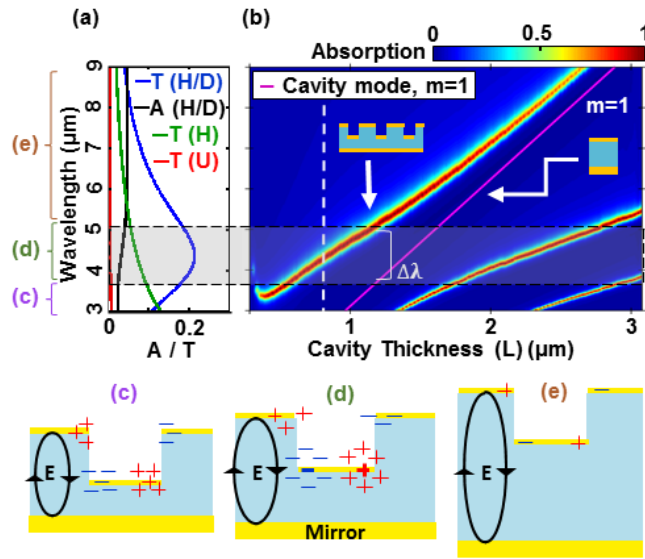


Figure 35: The dispersion of the optical cavity.

(a) The light transmission of a 30 nm thick film without pattern (red), with subwavelength hole (green) and coupled hole-disk (blue) arrays. The black diagram shows the absorption of coupled hole-disk array. (b) FDTD predicted change in absorption as a function of wavelength and cavity length of the system for same system parameters as given in (a). The line cut (white, dotted line) represents the plot in Fig.1(c). (c, d, e) Cartoons depict the reason for red-shift of resonant absorption peak as a function of cavity height. Strength of excited charges on the disk as a function of its depth in the cavity, excitation is strongest at the antinode (shown in d) in the center of the optical cavity corresponding to first cavity mode. [T –Transmission and A – Absorption, H-Hole Array, D-Disk Array, H/D-Hole-Disk Array, U-Unpatterned]

The Dispersion of the Optical Cavity

To understand the origin of the narrow band absorption in the cavity-coupled hole-disk array, first, it is imperative to understand the mechanism of light funneling into the cavity through the cavity-

uncoupled subwavelength hole-disk array. The light transmission of unpatterned gold film (red), the hole array (green), the light transmission (blue) and absorption (black) of the hole-disk array is shown in Figure 35a. While the light transmission of a 30 nm thick flat gold film is less than 1% and for hole array is 7% at 3-9 μm , the hole-disk array has a transmission peak of 23 % at 4.4 μm and absorption stays constant ~5% throughout the chosen wavelength range. It is well-known that an array of subwavelength holes has an intrinsic extraordinary transmission of light compared to apertures of same dimensions predicted by aperture theory and larger than planar metal film of same thickness, which is attributed to the excitation of surface plasmons on the edges of the holes and subsequent reradiation on the other side [233, 234]. In mid-IR spectral region, in absence of natural plasmons, a perforated metal surface supports bounded surface waves or spoof plasmons to couple the incident light to the metal and create localized charges around the holes [235, 236]. In this coupled hole/disk system these localized charges on the hole create complimentary charge oscillations on the disk which can radiate light more efficiently compared to the hole. This is a direct result of electric dipole moment of the disk-array at resonance wavelength which is stronger than hole-array due to the higher charge concentration and longer lifetime of plasmons on the isolated disks (hence less number of channels for radiation and resistive loss decay) [1, 24, 237].

The extraordinary transmission of the hole-disk array when coupled to a photonic cavity enables efficient coupling of light further. The simulated (FDTD) absorption spectrum as a function of cavity length and wavelength is shown in Figure 35b for parameters $P = 1.140 \mu\text{m}$, $D = 0.760 \mu\text{m}$ and $RD = 280 \text{ nm}$. The predicted first order ($m = 1$) Fabry-Perot cavity mode ($C = m\lambda/2n_{\text{eff}}$) corresponding to a simple planar cavity (magenta) has been plotted on top of the FDTD simulation. The presence of the disk array in the cavity not only adds an extra phase to the original cavity response, but also enhances the coupling of incident light even further. These roles of the hole-array are explained in detail below.

The deviation of the resonant absorption wavelength of the cavity-coupled hole-disk array from that of a simple cavity (Figure 35a magenta plot) is due to the accrued extra phase-shift in presence of the disk-array inside the cavity [10, 23].

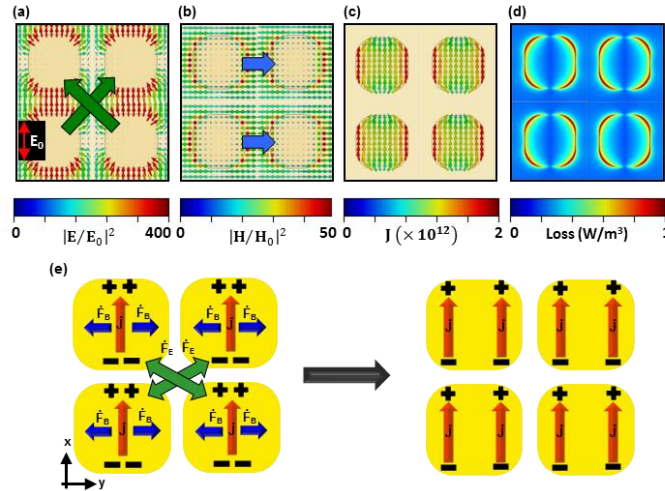


Figure 36: Loss process in the cavity-coupled hole-disk system.

FDTD predicted (a) E-field, (b) H-field, (c) current distribution on the disk clearly shows the current drift towards the edges due to the electric (FE) and magnetic (FB) forces and (d) power loss distribution. (e) Schematic of charge distribution on the disk and corresponding electric (FE) and magnetic (FB) forces due to the coupling and the resultant shift of the charges to the edges of the disks.

For the cavity resonance to exist, there must be an electric field antinode at $C_0/2$ or $\lambda/(4n_{\text{eff}})$ height in the cavity, where n_{eff} is the effective refractive index of the cavity spacer in presence of surface plasmon sets the optical cavity length (C_0) shorter than the length of physical cavity (C). In this position, there is cavity-assisted surface plasmon excitation on the disk array [217]. For a constant RD, when the cavity length is increased, the disk-array passes through the position of enhanced electric field in the center of the cavity, introducing large phase shift due to stronger electron plasma oscillations and red-shifts the total response. As the cavity height becomes much larger than RD, this phase shift becomes comparatively low and the response of the two systems asymptotically converges (in Figure 35b for $C > 2\mu\text{m}$). This is pictorially represented in Figure 35c-e. The light absorption of the cavity-coupled hole-disk array is near unity in the

shaded region (Figure 35a-b), which corresponds to the resonance wavelength of the hole-disk array. As mentioned above, the presence of the disk-array in the cavity red-shifts the resonance by excitation of charge oscillations on the surface. These oscillations are further enhanced when the position of disk-array is close to $C_0/2$ (antinode). This enhancement in the excited surface charges is coupled back to the upper hole-array strengthening the charge oscillations that are already present. This effect leads to artificial enhancement of the light coupling into the cavity. The presence of the cavity also dictates strict phase-matching condition for the complete absorption of light and hence the resulting bandwidth is very narrow ($\Delta\lambda/\lambda_{\text{res}} \sim 0.062$, FWHM=270 nm at $\lambda_{\text{res}} = 4.4 \mu\text{m}$).

Loss Mechanism

To understand the location of the losses in the cavity-coupled hole-disk array, full-vectorial simulation of Maxwell's equations is carried out and the electric field, magnetic field and current distribution on the surface of disk array are shown in Figures 36a-c, respectively for x-polarized light. As shown in these figures, due to the small lattice constant of disk array and edge-to-edge distance, charges on any disk element experience diagonal electric and adjacent magnetic forces. In addition, the charge oscillations on the disk also experience the charge oscillations on the hole due to strong hole-disk coupling as seen from the electric field distribution in Figure 33c (inset). This combination of in-phase forces split the excited micro-currents on the disks to the edges. The surface plasma oscillations decay due to the resistive loss and hot-carrier generation due to Landau damping [1, 29, 158, 218] which are responsible for the complete absorption of the incident light. The coupled hole-disk array functions like a two-element optical antenna and induces extraordinary transmission through the sub-wavelength hole/disk array where the transmission efficiency depends on the coupling strength. The hole/disk coupling strength enhances further in presence of the cavity inducing 100% coupling of the incident photons to the coupled system and zero back reflection. The edge current density on the hole-disk (\mathbf{J}) array generates an Ohmic loss $P = \mathbf{J} \cdot \mathbf{E}$,

where \mathbf{E} is the electric field and P is the power loss. This power loss is responsible for the light absorption, as shown in Figure 36d. Figure 36e pictorially demonstrates the creation of microcurrent.

Experimental results

Due to the plasmonic nature of the resonance, the resonant absorption wavelength scales as a function of hole/disk size, as shown in Figure 37.

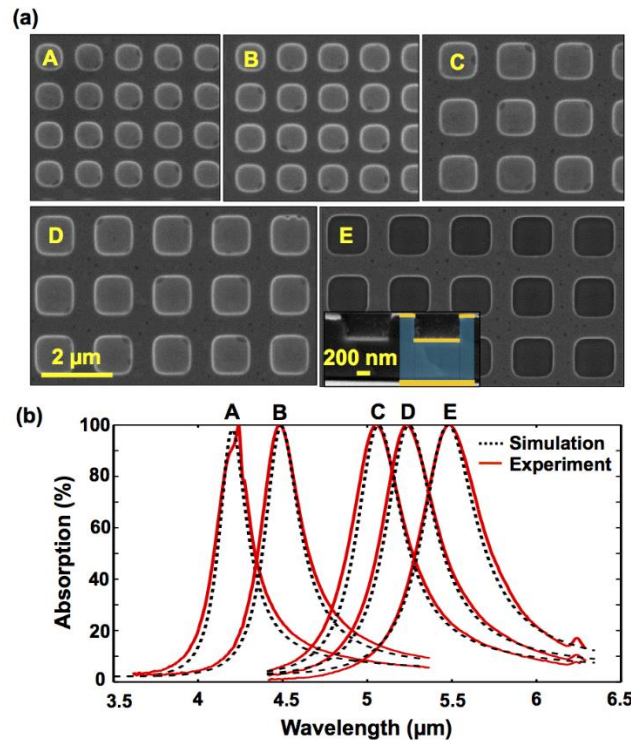


Figure 37: Characterization and measurement results

(a) SEM images for five cavity-coupled absorbers with periods ($P = 1.1, 1.14, 1.6, 1.66$ and $1.74\mu\text{m}$ in frames A-E) with diameter to period ratio is kept constant ($D/P = 0.6$). Inset shows the cross section of the quasi-3D structure. (b) Measured absorption spectra for the periods shown in part (a) along with simulated spectra for each pattern.

The proposed system is fabricated following a simple large area nanoimprinting technique. A PDMS stamp is embossed against a photoresist (SU-8) layer spin coated on a glass substrate coated with optically thick (200 nm) gold mirror and followed by 2 hours UV-exposure and one-hour post exposure bake ($T=95^\circ\text{C}$). This step forms the hole-array impression on SU-8 which further serves as the dielectric spacer ($C=870\text{nm}$)

in the cavity. The blanket e-beam deposition of thin layer (30 nm) of gold completes the simple fabrication process. The deposited gold forms the top perforated hole pattern on the raised region of the polymer imprint and the bottom disk array in the recessed region. Figure 37a shows the SEM images of five such representative systems with varied hole/disk diameter for constant $D/P = (0.60-0.66)$. The corresponding optical photon capture via absorption measurements using a microscope-coupled FTIR (Hyperion 1000-Vertex 80, Bruker Inc.) along with FDTD simulation predictions appear in Figure 37b. As predicted, near 100% of the incident radiation is captured which is geometrically tunable.

Conclusion

In conclusion, this chapter demonstrates a unique cavity phase driven perfect absorption based on hybrid plasmons induced extraordinary transmission through a subwavelength complementary aperture array producing a light funneling effect for three-dimensional noble metals. Photonic microcavity coupling of a subwavelength hole-disk array, a two-element metal/dielectric composite structure with enhanced extraordinary transmission, leads to 100% coupling of incident light to the cavity system and subsequent absorption. This light-funneling process arises from the temporal and spatial coupling of the broadband localized surface plasmon resonance on the coupled hole-disk array and the photonic modes of the optical cavity, which induces spectral narrowing of the perfect absorption of light. The cavity-phase driven and geometrically tunable photon capture and absorption when couple with a large area nanoimprinting based low cost fabrication process, opens up a new way of enhancing light-matter interactions for practical applications like frequency selective infrared detection, bio-sensing, light harvesting, etc.

CHAPTER 6: PLASMON-ASSISTED MID-INFRARED PHOTODETECTION USING 3D NOBLE METALS

Published at <https://www.osapublishing.org/oe/abstract.cfm?uri=oe-26-25-32931> on 3 December 2018 by Optics Express. DOI: <https://doi.org/10.1364/OE.26.032931>, Alireza Safaei, Sushrut Modak, Jonathan Lee, Sayan Chandra, Daniel Franklin, Abraham Vázquez-Guardado, Debashis Chanda

Introduction

As mentioned in the previous chapters, surface plasmon is collective oscillation of electrons on metal-insulator interface excited by an electromagnetic wave; the surface plasmons can be either in the SPP or LSP mode [238, 239]. The fundamental order of LSP, the dipolar excitation, has the highest strength and its properties, i.e. resonance frequency and lifetime, are determined by the particle polarizability and lattice sum which depend on the metal/insulator dielectric functions and the geometrical parameters [12, 237, 240, 241]. This dependence gives a way to control and tailor the surface plasmon resonances to desired frequencies. Surface plasmons have the potential to be used in integrated photonic circuits [238, 242], SERS measurements [237], flat optics [10], hot-electron injected sensors [238, 242] and metamaterials with properties such as near-zero [243], negative [244] and hyperbolic [245] index of refraction. The prime difficulty in bringing these concepts to full-fledged applications is the large plasmon decay rate mainly due to the finite metal conductivity that decreases the lifetime of the excited surface plasmon and induce losses in the form of heat dissipation [246, 247]. For a long time, this loss was considered to be a major limiting factor in realization of plasmonic devices but later this very loss is used as a benefit. The narrowband perfect light absorption has been shown theoretically and experimentally through critical coupling by resonant plasmonic systems [7, 229, 248-256]. Devices, which use narrowband

plasmonic absorbers, were demonstrated for perfect metamaterial absorbers [257], spatial modulators [240, 258] and narrowband infrared detection [8, 9, 65, 66, 259-267].

In this chapter, I extend further on to the use of lossy plasmons as a mechanism of “color” sensing in infrared frequency domain by virtue of bolometric principle [65, 66]. I propose quasi 3D plasmonic crystal consisting of vertically-separated complementary nanohole and nanodisk arrays coupled to an optical cavity. The general behavior of this complex system is determined by the interaction of optical cavity modes, spoof plasmonic excitation on the perforated film [235, 236], hybrid plasmonic excitation on the disk array and vertical/horizontal coupling of the metallic dipolar elements, as explained by details in our previous work [240]. The purpose of exploiting mid-IR plasmon is increasing the absorption in a very small volume (low thermal mass) of the device, resulted in lower noise and higher output signal [236, 268]. The geometric nature of this plasmonic crystal “funnels” the light through the subwavelength holes coupled to the disk array by exciting hybrid plasmon, which is dissipated in the form of resistive loss resulting from induced micro-currents on the edge of dipole elements (holes and disks). Surface patterning with a superlattice to sense the power dissipation with external biasing circuitry show promising results with very high spectral selectivity and response time. A 3 dB response time of 100 μ s is measured, which outperforms present microbolometer’s typical response time of 10-15 ms [266, 267, 269]. The frequency selective infrared absorption spectroscopy has proven to be a very important tool in the detection and identification of airborne chemicals by comparing infrared light absorption in presence and absence of airborne contaminants. The geometrical tunability and narrow bandwidth of the light absorption not only determines the contaminants, but also their concentration. At present both cooled and uncooled mid-IR detectors are being broadband “bucket” detectors generate integrated spectral response. Such broadband detectors are not accurate enough to

perform narrow-band low concentration chemical detection from IR radiation [266, 270-273]. There are quite a few IR detector concepts at the research level which are potential candidates for frequency selective detectors [252, 274, 275]. The proposed quasi-3D plasmonic absorber possesses inherent frequency selective detection capability paving the path towards low cost room temperature infrared “color” photon detection with high signal to noise ratio when packaged into a commercial detector architecture. The optical response of the proposed nanodevice is independent of the light polarization and angle of incidence; moreover, nanoimprinting based simple, large area and low-cost fabrication technique makes this detector realizable for the practical applications [4, 9].

Quasi-3D plasmonic crystal “light funnel”

Nanostructure Design

Figure 38a-top schematically illustrates the proposed plasmonic crystal and the corresponding light funneling phenomenon. The quasi-3D imprinted surface is composed of a sub-wavelength perforated film and its complementary disk array with period P and diameter D , separated from the film by RD coupled to an optical cavity with thickness L . The composite system functions like a “light funnel” as can be observed from the 3D FDTD simulation of energy flow, represented by the Poynting vector in Fig. 1(a-bottom). The simulation results show that the plane-wave incident on the top surface collapses into the subwavelength aperture like a liquid flow through a mechanical funnel, resulting in perfect capture of the incident photons at the resonance wavelength $\lambda_{res} = 4.4 \mu\text{m}$ for $P = 1.14 \mu\text{m}$, $D = 0.760 \mu\text{m}$, $RD = 0.28 \mu\text{m}$ and $L = 0.87 \mu\text{m}$. A close correlation is observed between the simulated (solid black) and measured (solid purple) absorption spectra shown in Figure 38b. In order to understand the origin of the light funneling, transmission

spectra of the constituent perforated film (dashed blue) and the coupled hole-disk arrays (solid blue) are overlaid in Figure 38b. Further, analytical CDA (black dashed line) is plotted in Figure 38b. The good agreement of the experiment, FDTD simulation and CDA approach validates the underlying physics of the light absorption spectrum which is the temporal and spatial interaction of the coupled electric dipole arrays and the Fabry-Perot modes of the cavity as described in detailed in our separate publication [240, 276].

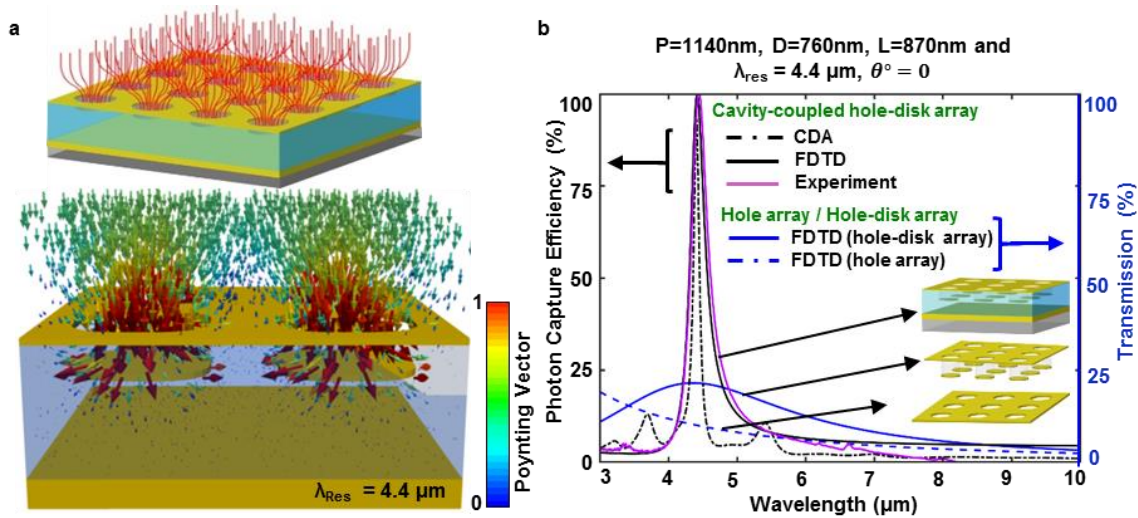


Figure 38: Cavity-coupled quasi-3D plasmonic crystal “Light Funnel”.

(a) schematic illustration (top) and computed (bottom) 3D pointing vector of the incident radiation ($\lambda_{res} = 4.4 \mu\text{m}$). (b) Predicted transmission of the hole-array (dashed-blue) and hole-disk array (blue) through the subwavelength hole and hole-disk array of period $P = 1.14 \mu\text{m}$, diameter $D = 0.76 \mu\text{m}$ and relief depth $RD = 280 \text{ nm}$. The absorption with full-wave electromagnetic simulation (black) of the cavity-coupled system along with the analytical coupled dipole approximation (CDA) prediction (black-dotted) have been overlaid for comparison for cavity thickness $L = 0.87 \mu\text{m}$ ($\lambda_{res}=4.4 \mu\text{m}$). The corresponding experimental verification of absorption is plotted in (purple).

Angular Optical Response

The light funneling effect is almost angle independent over a wide angle of incident which can be seen from the RCWA simulation as well as experimental measurement in Figure 39a (top and bottom respectively). The angle dependent absorption measurement is carried out in an IR integrating sphere setup which is susceptible to noise and requires long integration times for reliable data collection. Hence, a sample with larger cavity thickness ($L = 1.040 \mu\text{m}$, $\lambda_{\text{res}} = 4.8 \mu\text{m}$) is chosen so the resonance is away from the carbon dioxide absorption line ($\lambda_{\text{CO}_2} \sim 4.4 \mu\text{m}$) to remove a major noise source by design.

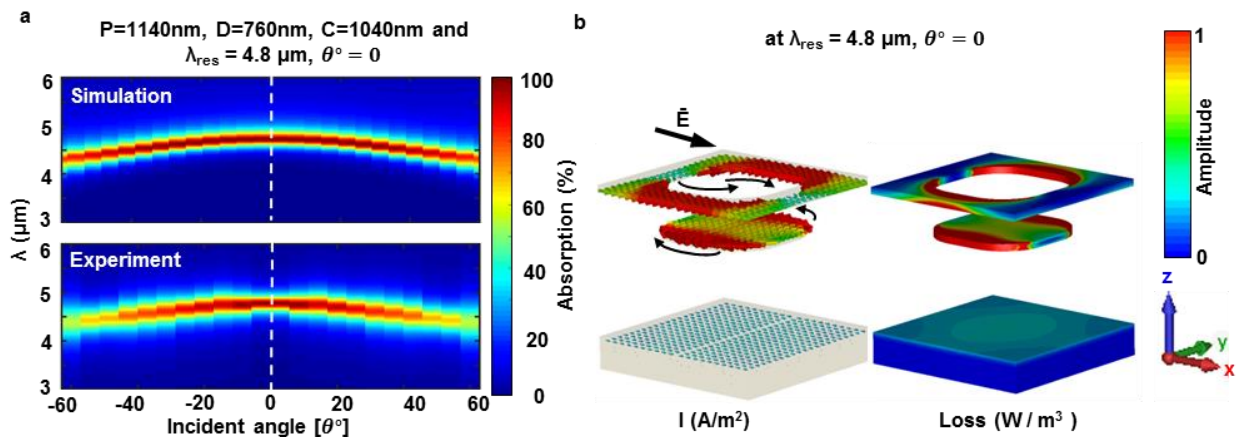


Figure 39: Angular optical response and power loss.

Structural parameters for study of angle dependence of resonance wavelength: $P=1140\text{nm}$, $D=760\text{nm}$, $RD=280\text{nm}$ and $L=1040\text{nm}$ with resonance wavelength = $4.8\mu\text{m}$. (a) (top) Rigorous coupled wave analysis (RCWA) prediction and (bottom) experimentally measured angular absorption of the plasmonic crystal (b) Current density (J) (left) and loss profile of the metal (right) at resonance wavelength.

The plasmonic crystal captures energy with close to 100% efficiency across a wide angular span like a “light funnel”. Beyond a steep angular range ($> 60^\circ$), due to the change of dipole polarizability and the coupling between elements, a shift in the plasmon excitation wavelength of

the two complementary arrays is observed. Moreover, the change in the effective cavity length detunes the combined resonance and diminishes absorption as analytically and numerically demonstrated in our earlier findings[240]. The good agreement between RCWA prediction and experimental measurement in Figure 39a strongly supports the effectiveness of light funneling over wide angles of incidence.

CST Microwave Studio and FDTD, Lumerical inc. were used for electromagnetic simulations. Dispersion for gold is obtained by fitting Palik's experimental data [277] with Drude model, and refractive index of SU-8 is considered as 1.56. To accurately perform simulations for the samples, which were fabricated, exact values of diameter and the rounding radius of hole is obtained from SEM images. Angle dependent RCWA simulations were conducted with a custom-built MATLAB script to understand the angle dependent behavior of the structure due to the limitations of FDTD method for oblique angles of incidence. To measure the absorption spectra of the sample for the normal incident light, a 2.5x, 0.07 numerical aperture IR transparent ZnSe objective lens on an optical microscope (Hyperion 1000) coupled to a Fourier transform infrared (FTIR) spectrometer (Vertex 80, Bruker Corp.) and a mercury cadmium telluride (MCT) photodetector was used. Since the MCT photodetector is cryogenically cooled, it offers much higher signal to noise ratio and hence needs lower integration time. This setup is designed just for characterization of normal angle of incidence. In order to quantify the wavelength dependent absorption for non-normal angle of incidence a special gold coated integrating sphere (Bruker Inc.) coupled to a FTIR spectrometer is used. The integrating sphere has its own room temperature bolometer to detect the scattered photons. Since bolometer has higher noise compared to the cryogenic detector, we increased the integration time (10 min) to obtain reflection spectrum with lower noise. Reflection spectra were normalized to a gold mirror with 96% reflectivity over the wavelengths examined.

Plasmon Loss Mechanism

An analysis of the fields inside the composite structure reveals the absorption and subsequent dissipation mechanisms, as shown in Figure 39b. The incident plane-wave induces in-phase charge oscillations, LSP, in the direction of the electric field around the edges of the holes on the top surface, as seen from Figure 39b-left. The near-field coupling induces complementary charge oscillations (coupled LSP) in the disc concentrated around the edges. In the presence of a mirror at a distance L the charge oscillations and the electric dipole magnitude on the disk array are reinforced due to the electric field antinode in the center of the cavity ($L_{\text{eff}} = (2m + 1) \lambda / 2n_{\text{eff}}$). The reinforced charge oscillations on the disc-array in turn increase the near field coupling with the hole-array (positive feedback) leading to the transmission enhancement with 100% coupling efficiency and the funneling behavior of the structure. The strength of the positive feedback depends on two factors- the strength of near field coupling between holes and disk (hence the distance between them) and the position of the disk array in the cavity, i.e., the intensity of electric field ‘seen’ by the disc array. Moreover, the lateral coupling between the disk and hole-array is also important for the high amplitude of absorption. Increase in the distance between elements decreases the coupling between them, which in turn reduces the total absorption in the structure. Increasing the angle effectively reduces the effective pattern period and red shifts the resonance. At the same time, the effective distance between the hole and disk is increased compared to the period, which in turn blue shifts the resonance (dominant effect) and the overall coupling strength diminishes as well. This is verified in Figure 39a-top (angular measurements) and bottom (angle dependent RCWA simulation).

The bulk of the light is absorbed along the edges of hole and disc array as seen from Figure 39b-right and it is important to understand the reason behind this phenomenon. The discs

are part of a lattice composed of discrete elements and the Coulomb interaction with the neighboring discs force the induced charges on the discs to move to the edges but more predominantly to the corners. Counter-propagating LSP on the edges of hole and disk form a magnetic dipole and one pair of hole-disk supports two such magnetic dipoles on opposite edges, as shown in Figure 39b-left. The localized nature of the current density on hole-disk is responsible for the paired magnetic dipoles to incur high Ohmic losses $P = \mathbf{J} \cdot \mathbf{E}$, where \mathbf{J} is the current density; \mathbf{E} is the electric field and P is the loss power density). The simulated 3D current distribution is shown in Figure 39b-left which clearly verifies the origin of the photon capture and dissipation on the edges of the hole-disk as observed in Figure 39b-right.

Light detection

Detection Circuit

Ideal surface plasmons with zero damping have many interesting properties like near-zero index and infinite phase velocity which are theoretically predicted [278-280] but the translation of these ideas into practical realm is limited due to the inherent losses in metals that are used to fabricate such structures. In most applications, the presence of metal is not desirable due to the loss; however, sensing applications can take advantage of the plasmon damping and plasmon-phonon coupling to sense change in the electrical conductivity. In this proposed system, the change in resistance of the plasmonic crystal due to the absorbed electromagnetic radiation is measured with the help of a DC biasing circuit. Schematic illustration of the circuit is shown in Figures 40a-b. The scanning electron microscopy image of the fabricated super-lattice is shown in Figure 40c. The circuit uses a simple voltage divider scheme to bias the detector, as shown in Figure 40d. The plasmonic film absorbs the incident radiation and produces thermal energy which

in turn manifests in the form of resistance change. The continuous perforated film enables electronic probing of the induced “micro-current” plasmon loss on each nanohole via the weak bias current (I_B). The input impedance is increased from a few ohms to kilo-ohm range with the superposition of a serpentine super-lattice pattern to amplify the resistive change ($\Delta R \approx R_D \alpha \Delta T$, where R_D is the detector resistance at room temperature, α is the thermal coefficient of resistance and ΔT is the induced temperature change due to absorbed radiation) and reduce the background heating (Joule heating [65, 260, 266, 267]) due to the bias current.

Detector Fabrication

As seen from the SEM images in Figure 40c, the device consists of the gold serpentine absorber with hole-disk nanopattern supported by a polymer base (SU-8 2000.5). A gold mirror on glass substrate supports the polymer. In this manner, the polymer acts as the cavity dielectric, moreover, the polymer curing process minimizes and makes the absorption in the polymer negligible. Large area (4 mm x 4 mm) square arrays of subwavelength cylindrical depressions were molded onto the surface of a thin layer of a photo curable epoxy (SU-8 2000.5, MicroChem), by pressing the substrate against a polydimethylsiloxane (PDMS, 10:1 Sylgard 184) mold containing the inverse pattern. The thickness of the epoxy was controlled through the spin-coating process. A gold-coated microscope glass slide served as the substrate. To form the detector super-lattice serpentine pattern, after imprinting, a prolonged UV exposure (30 min) and post exposure bake (95 deg for 60 min) was conducted to make SU-8 fully cross-linked to make it resistant to acetone during subsequent liftoff process. A UV lithography step was performed on top of this imprinted array of holes followed by blanket deposition of gold (~30 nm) and lift-off process to form serpentine layout with contact pads to facilitate electrical measurements. The size of serpentine pattern is 1 mm x 1 mm and width of each line in the serpentine

pattern is $25\ \mu\text{m}$ for the present design. A conductive silver epoxy is used to attach wires to the contact pads for electrical interfacing with measurement setup.

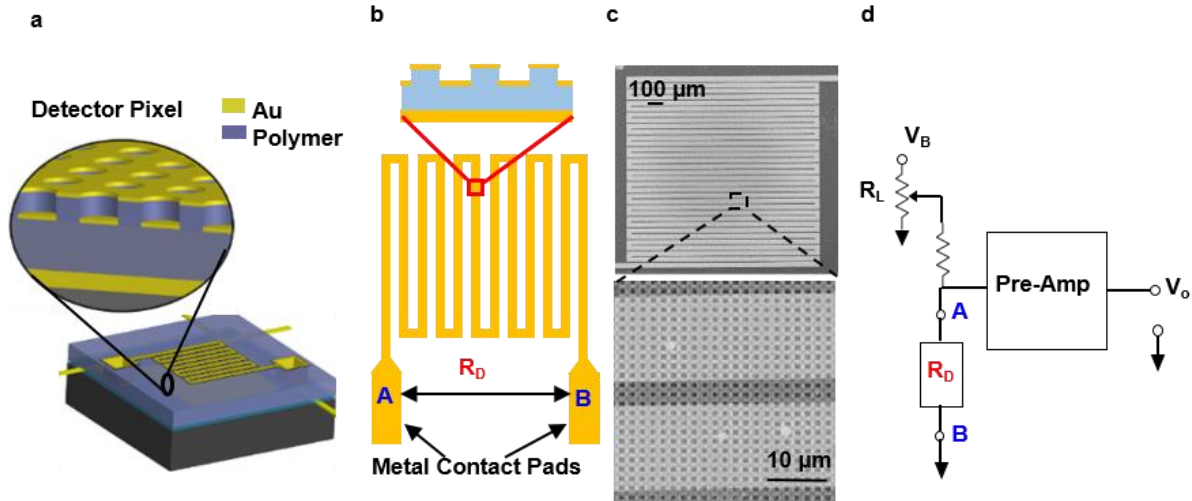


Figure 40: Photodetection mechanism.

(a) 3D cartoon depicting the structure of the detector, (b) upper gold film formatted in the form of a serpentine pattern (superlattice) to form a path with significant resistance and contact pads for interfacing with external biasing circuit (c) SEM image of the fabricated detector with hole-disk nano-pattern and gold film in the form of serpentine pattern and (d) interfacing circuit in voltage divider bias mode (right) as used in the experiments.

The super-lattice pattern plays the important role of enhancing the signal to noise ratio albeit bit reduction ($\sim 5\%$) in overall photon capture efficiency due to the reduction in active area. The plasmonic surface with $D = 0.760\ \mu\text{m}$, $P = 1.14\ \mu\text{m}$ and the gold thickness of $30\ \text{nm}$ results in $\sim 4\ \text{ohm}/\text{mm}^2$ resistance which is increased to $\sim 7\text{k}\ \text{ohm}/\text{mm}^2$ with the serpentine pattern with $25\ \mu\text{m}$ width and 85% duty cycle. The schematic of the measurement circuit is shown in Figure 40b.

Bolometer performance

Responsivity

The measured photon capture/absorption spectra of three fabricated spectrally selective plasmonic infrared detectors are plotted along with the normalized black body radiation at $T = 1200^\circ \text{C}$ in Figure 41a. The spectral detuning of detectors ($\lambda_1 = 4.2 \mu\text{m}$, $\lambda_2 = 4.5 \mu\text{m}$ and $\lambda_3 = 4.8 \mu\text{m}$) is achieved through cavity thickness variation ($L_1 = 0.760 \mu\text{m}$, $L_2 = 0.920 \mu\text{m}$ and $L_3 = 1.040 \mu\text{m}$) for constant diameter, $D = 0.760 \mu\text{m}$ and period, $P = 1.14 \mu\text{m}$. The corresponding measured voltage change (ΔV_o) divided by the respective detector electrical resistance $\Delta V_o/R_m$ as a function of bias current for the three narrowband (FWHM $\sim 300 \text{ nm}$) frequency selective plasmonic detectors at ambient temperature and pressure are shown in Figure 41b. The signal voltage is normalized with respect to the detector resistance to remove the effect of detector-to-detector resistance variation from the results. The normalized voltage scales according to the absorbed incident power at the absorption wavelength for a given source temperature. Such spectrally resolved detection is not possible with the conventional broadband bucket detectors. A measure of the sensitivity of a radiation sensor is calculated from its NEP. Out of the various noise sources such as photon noise, thermal fluctuation noise, $1/f$ noise and thermal noise; resistive detector like this one have thermal noise (Johnson noise) as the dominant source of noise which is directly proportional to the square root of the resistance of the sensor [270, 273].

The figure of merit of a detector that considers NEP, detector area (A) and bandwidth (Δf) of operation is specific detectivity D_{FS}^* ($D^* = \sqrt{A\Delta f}/NEP \text{ cm}\sqrt{\text{Hz/W}}$, the suffix ‘ FS ’ stands for frequency selective in order to distinguish it from the traditional D^* of broadband detectors). A Simulink model is developed to solve the heat equations for the current device

architecture to understand its theoretical performance limits and emulate the thermal equations for a given device geometry. It takes geometric parameters of the device, thermal and electrical constants of the constituent materials, incident radiation power and the chopping frequency as the input parameters to generate the time dependent voltage response and time constant.

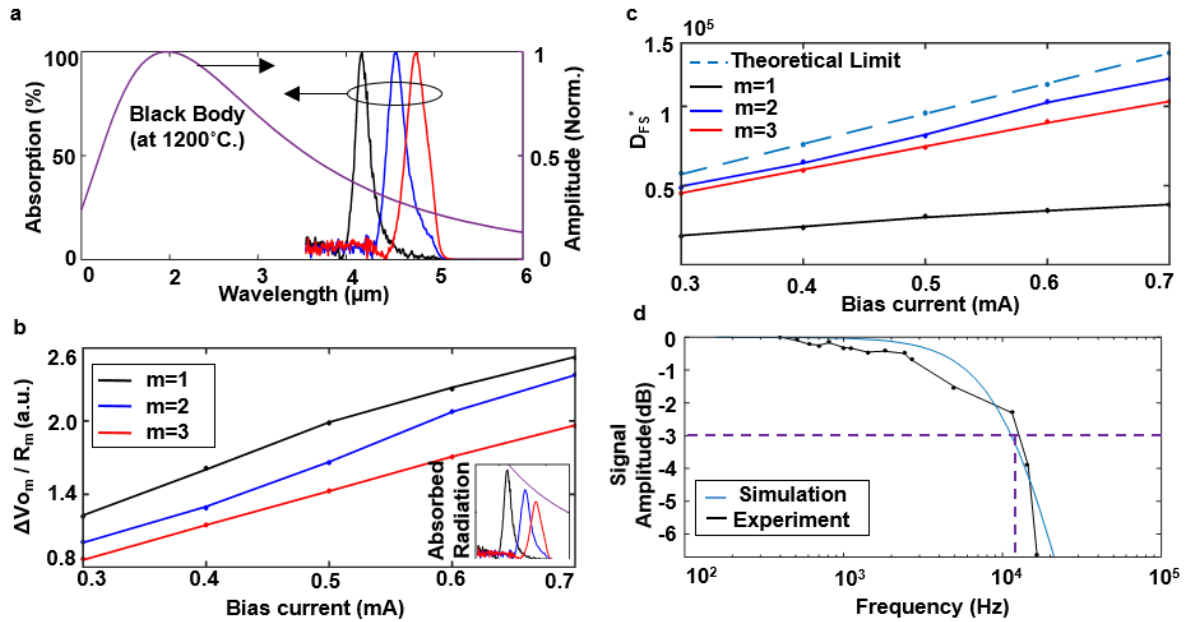


Figure 41: The bolometer performance.

(a) Normalized black-body spectrum along with frequency selective absorption spectra of three detectors at $4.2 \mu\text{m}$ ($m=1$), $4.5 \mu\text{m}$ ($m=2$) and $4.8 \mu\text{m}$ ($m=3$). (b) Normalized detector output $\Delta V_m / R_m$ for $m = 1$ to 3. Inset shows the absorbed incident power of the detectors at a constant source temperature of 1200°C . The individual detector response follows the absorbed incident power. (c) Predicted (with Simulink model) and measured specific detectivity of the frequency selective detectors. (d) Simulated (dotted blue) and measured (with 3ω method) detector frequency response. The measured 3 dB roll-off indicates a response time of $100 \mu\text{s}$.

Detectivity and Response Time

The simulated detectivity and time response are plotted in Figures 41c and 41d, respectively. Thermal noise limited measured detectivity of three detectors as a function of bias current is plotted in Figure 41c. The measured D_{FS}^* of the three frequency-selective plasmonic

detectors closely follow the theoretical limit. The measured frequency selective D^* for the present case is not directly comparable to cooled or uncooled broadband IR detectors due to their broadband energy absorption, as the signal and the noise generation processes both depend on the bandwidth [265]. Further, the frequency response of the detector is measured with AC electrical 3ω method [260, 281-283] and is plotted in Figure 41d. A 3 dB response time of 100 μ s is measured which outperforms present microbolometers response time of 10-15 ms [266, 267, 269].

Present commercially available suspended Vanadium Oxide (VO_x) based microbolometers response time ranges between 6-20 ms (European space agency; FLIR) with the responsivity of 600 mV/W . In addition, ULIS Inc. reported a time response of 2.5 ms which is the record for the commercial high-sensitive room temperature microbolometers. The short surface plasmon life time ($\sim 10^{-15}$ s) [238] and extremely fast thermal dissipation ($\sim 10^{-9}$ s) [247] due to the ultra-low thermal mass makes plasmonic detectors on the faster side compared to bulk absorption based thermal detectors. Further design optimization with reduction in thermal conductivity based on a suspended detector architecture, partial vacuum seal and electrical noise reduction following well-known commercial IR detector fabrication procedures will drastically improve the present frequency selective plasmonic detector signal to noise ratio ($D^* \sim 10^8 - 10^9 \text{ cm}\cdot\sqrt{\text{Hz}}/\text{W}$) [270, 271, 273]. The bolometers made from perforated gold on ZnO can reach to the maximum responsivity of $R_{\text{max}}=10 \text{ mV/W}$ which is smaller than our value ($R_{\text{max}}\approx 15 \text{ mV/W}$) [249]. Single nanowire-based infrared bolometer is reported to possess the responsivity of $R_{\text{max}}=70 \text{ mV/W}$, but it lacked the spectral tunability. Excitation of plasmon on gold nanowire sitting on SiO_2 can increase the R_{max} to 400 mV/W , at the cost of polarization dependency and complex fabrication steps [284]. The proposed detector when fabricated in a suspended architecture can reach to higher responsivity and D^* . The predicted responsivity of the suspended proposed microbolometer working at room

temperature is $R_{\max} \approx 1 \text{ kV/W} - 10 \text{ kV/W}$, $D^* \approx 5 \times 10^7 \text{ cmHz}^{1/2}\text{W}^{-1} - 2 \times 10^9 \text{ cmHz}^{1/2}\text{W}^{-1}$, while the time constant is $\tau = 0.5 \text{ ms} - 1 \text{ s}$ for a similar pixel dimension [68, 285, 286].

Conclusion

Frequency selective detection of low energy photons is a scientific challenge using natural materials. A hypothetical surface which functions like a light funnel with very low thermal mass in order to enhance photon collection and suppress background thermal noise is the ideal solution to address both low temperature and frequency selective detection limitations of present detection systems. In this chapter, I presented a cavity-coupled quasi-three dimensional plasmonic crystal which induces impedance matching to the free space giving rise to extraordinary transmission through the sub-wavelength aperture array like a “light funnel” in coupling low energy incident photons resulting in frequency selective perfect ($\sim 100\%$) absorption of the incident radiation and zero back reflection. The peak wavelength of absorption of the incident light is almost independent of the angle of incidence and remains within 20% of its maximum (100%) up to $\theta_i \leq 45^\circ$. This perfect absorption results from the incident light-driven localized edge “micro-plasma” currents on the lossy metallic surfaces. The wide-angle light funneling is validated with experimental measurements. Further, a super-lattice based electronic biasing circuit converts the absorbed narrow linewidth ($\Delta\lambda/\lambda_0 < 0.075$) photon energy inside the sub-wavelength thick film ($< \lambda/100$) to voltage output with high signal to noise ratio close to the theoretical limit.

Metal based plasmonic nanostructures suffer from metallic loss, but here I took advantage of such a high resistive loss for the detection of photons. Such controlled infrared absorption when implemented in conjunction with simple large area imprinting techniques leads to development of a new class of frequency selective, low cost, uncooled infrared detectors. My initial studies presented above have shown that a frequency selective plasmonic surface can

alleviate some of the limitations of present IR detectors and offer significant improvements in frequency selective detection paving the path towards IR “color” imaging by pixel/sub-pixel formation with plasmonic surfaces tuned to various IR bands.

CHAPTER 7: PLASMON-ASSISTED LIGHT FOCUSING

Published at <https://onlinelibrary.wiley.com/doi/full/10.1002/adom.201800216> on 19 April 2018 by Advanced Optical Materials. DOI: <https://doi.org/10.1002/adom.201800216>, Alireza Safaei, Abraham Vázquez-Guardado, Daniel Franklin, Michael N. Leuenberger, Debashis Chanda

Introduction

Conventional optical elements such as lenses, waveplates and polarizers function by adding gradual phase delays to the propagating light. The accumulated phase by propagating light through a lens is defined as $\Delta\varphi = \Delta n |\mathbf{k}| \Delta l$, where Δn is the refractive index difference between the surrounding medium and the lens, $|\mathbf{k}|$ is the magnitude of the wavenumber and Δl is the propagation distance. For conventional refractive lenses Δn is small, which means that the thicknesses of these dielectric optical components need to be much larger than the wavelength of incoming light to accumulate 0 to π phase shifts. That means sub-wavelength compact planar geometry is not possible in conventional lenses making optical systems bulky. Furthermore, conventional lenses are limited by optical aberrations (e.g. spherical and chromatic) and diffraction limit [77]. The Abbe-Rayleigh diffraction limit is a natural obstacle in conventional optical lenses due to the far-field interference and absence of near-field [78]. Various planar lenses have been demonstrated following the diffractive optics concept of phase control based on dielectric scatterers on a 2D plane [17, 96, 97, 116, 287-289]. However, in the mid-infrared wavelength range (3-16 μm) such engineered dielectric surfaces are elusive due to the low spectral bandwidth [288, 289] and high thermal noise in long wavelengths [290, 291].

In contrast, plasmonic nanoantennas [92, 108, 109, 124, 292, 293] enable abrupt change in phase, amplitude and polarization of the incident light using sub-wavelength optical scatterers on a planar surface. Such control of phase according to the Huygens principle [79] allows the formation of arbitrary wavefront shapes enabling sub-wavelength focusing [17, 96, 97]. Spatially distributed plasmonic nanoantennas suppress higher diffraction orders and concentrate the incident light beam beyond the Abbe-Rayleigh diffraction limited focal point [90, 91, 94, 122]. In addition, possibility of the optical impedance matching with the free space by the patterned plasmonic interface reduces back scattering, leading to higher transmission efficiency [6, 17]. Going beyond the Abbe-Rayleigh diffraction limit requires the involvement of evanescent fields with large spatial frequency components which is possible by plasmonic nanoantennas, enabling sub-wavelength resolution capability going beyond the current imaging technologies [78, 104, 122-124].

In this chapter, I propose and experimentally demonstrate an ultrathin flat lens working in the mid-IR spectral range with geometrically tunable focal length and sub-wavelength focusing ability. The transmission efficiency of this flat lens is substantially higher compared to other reported plasmonic lenses due to the low metallic fill-fraction and the geometry [108, 109, 124, 294, 295]. The biggest limitation of dielectric as well as metallic flat lenses is the bandwidth of operation due to the inherent narrowband resonance [288, 289]. Previously, reported plasmonic flat lenses were limited to $\lambda \sim 1.0 \mu\text{m} - 1.9 \mu\text{m}$ [108], $\lambda \sim 5.2 \mu\text{m} - 9.9 \mu\text{m}$ [109], and $\lambda \sim 5 \mu\text{m} - 10 \mu\text{m}$ [124] operation bandwidths in the infrared spectral range. None of these works reported the most critical lens parameter transmission efficiency. In contrast, my proposed lens offers a wide operation bandwidth due to its gradient design. For the optimum design the experimentally measured transmission remained $> 70\%$ over the entire $4 - 10 \mu\text{m}$ mid-IR spectral range, which

promises further improvement in broadband transmission efficiency with improved fabrication procedures. Single (polarization dependent) and bi-layer (polarization independent) designs enable the polarization degree of freedom as well as tunable line and point focusing, respectively. Furthermore, such geometry defined tunable optical response overcomes the challenges associated with the unavailability of mid-infrared transparent materials for low footprint planar integration with thermal imaging systems [10, 296].

Controlling phase response on a 2D plane based on polar dielectric scatterers is well known in the literature as diffractive optics [17, 94, 96, 97, 101, 287]. However, as pointed out earlier, in the mid-IR spectral range most dielectrics are non-transparent. I demonstrate coupled gradient gold disk arrays as low loss broadband focusing element with a plasmon resonance in the mid infrared spectral range, far away from the natural plasmon resonance of gold. My proposed gold arrays work as follows. The incident light beam excites surface plasmons on the metallic nanostructure with a specified diameter (L_{res}), leading to coupling of the incident light beam to the array like an optical antenna. Strong interaction between the incident light beam and surface plasmon leads to an abrupt phase change of the scattered electric field [1, 11, 17, 87, 89, 90, 92, 93, 102, 108, 109, 113, 114, 125, 126]. Excitation of surface plasmons is due to the charge oscillation on the on the metallic elements driven by the incident electric field, and at the plasmon resonance frequency the driving optical field is in phase with the induced current. The change in the length of the nanostructure gives rise to the change in the resonance frequency and consequently the excited current leads or lags the incident field. A 2D pattern comprised of gradient gold disks with optimum diameter ratio creates a spatially varying phase response, which enables the modulation of the optical wavefront such that the energy is focused in forward direction [17, 124].

Focusing mechanism

Spatially Varying Gradient Phase Response

Figure 42a shows the proposed plasmonic lens, which is composed of an adiabatically tapered ultra-thin (45 nm) gold nanodisk array along one direction. Such a discrete gradient sub-wavelength gold disk array functions like an optical antenna array by concentrating the electromagnetic energy to a given direction based on the excitation of surface plasmons.

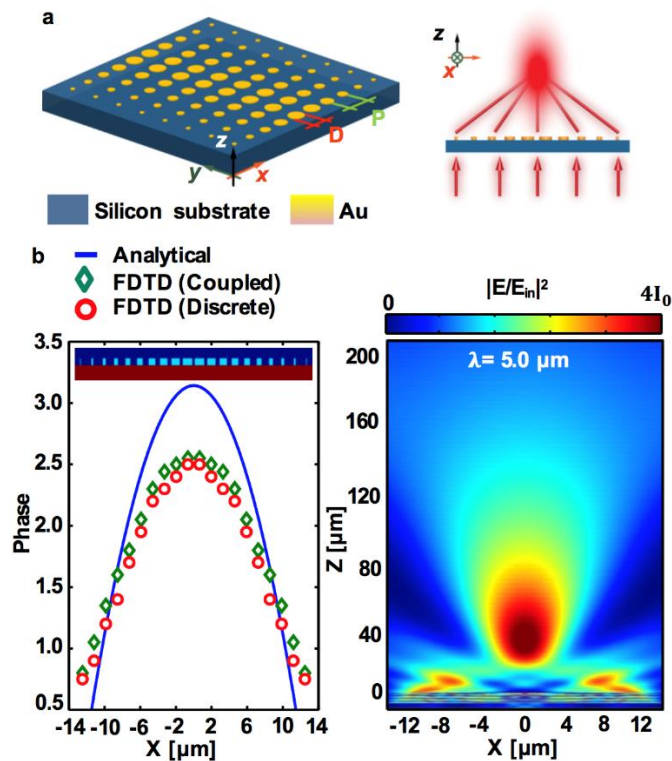


Figure 42: Gradient phase shift and focusing.

(a) (left) Schematic of the polarization-dependent plasmonic lens. The period (P) is constant and disk diameters (D) are variable. (right) Schematic of position dependent phase shifts by different disk arrays which leads to curved phase front. (b) (left) Phase shift of the incident light by coupled and detached disk arrays. The solid blue line shows the analytical phase shift for $F=40 \mu\text{m}$ and $\lambda=5.0 \mu\text{m}$ derived from Eq. (1). Top inset is the side view of the simulated nanostructure. (right) FDTD result of the focusing effect for Y-polarized light incident from bottom side of plasmonic lens with $P=1.3 \mu\text{m}$, $D_0=1.0 \mu\text{m}$ and $\Delta D=0.1 \mu\text{m}$ at $\lambda=5.0 \mu\text{m}$.

The abrupt phase shift originates from the excitation of two nondegenerate eigenmodes on the asymmetric pattern. The change in the in-plane size of the nanodisk elements for a constant period P changes the phase of the scattered optical field, thus enabling the creation of a curved phase front. For the line focus, the disk is arranged in a 2D array with a gradual change in diameter only in one direction, as shown in Figure 42a-left. The central 1D disk array adds the maximum phase shift to the scattered electromagnetic wave due to the excitation of the surface plasmon at the resonance wavelength (λ_{res}). The gradual decrease in the size of elements along the orthogonal direction gives rise to a weaker driving current and a lower phase delay, leading to the creation of a cylindrical wavefront. It means that in order to have a perfect optical flat lens operating at a specified wavelength (λ_m), the central arrays should be designed such that $\lambda_{\text{res}} = \lambda_m$. Such a gradient pattern creates a spatially varying phase response, giving rise to the focusing effect, as shown schematically in Figure 42a-right.

Cylindrical Optical Lens Phase Distribution

This single layer design acts as a far-field cylindrical optical flat lens at mid-IR frequencies for the polarization perpendicular to the direction of the diameter variation if the spatial distribution of the optical phase response (φ) follows [17, 94, 98]

$$\varphi(x) = 2n\pi + \frac{2\pi f}{\lambda} - \frac{2\pi\sqrt{f^2 + x^2}}{\lambda}, \quad (25)$$

where x is position, n is an integer, f denotes the focal length and λ stands for the wavelength of the incident light. To study the behavior of such a lens on-resonance and off-resonance, two flat lenses with different periods ($P = 1.3 \mu\text{m}$ and $P = 2 \mu\text{m}$) for a constant diameter difference of $\Delta D = (D_2 - D_1) = 100 \text{ nm}$ and constant central disk diameter of $D_0 = 1 \mu\text{m}$ are designed. The flat lens

with period $P = 1.3 \mu\text{m}$ has a resonance wavelength at $\lambda = 4.56 \mu\text{m}$, and the one with period $P = 2.0 \mu\text{m}$ at $\lambda = 6.5 \mu\text{m}$. The resonance wavelength of a lens pattern corresponds to the dip in the far-field transmission spectra which is same as the dip in the transmission efficiency at the focal point ($\lambda_{\text{res}} = 4.56 \mu\text{m}$ for $P = 1.3 \mu\text{m}$ and $\lambda_{\text{res}} = 6.5 \mu\text{m}$ for $P = 2.0 \mu\text{m}$), as shown with a dashed line in Figure 52a. Figure 42b-left compares the required phase defined by Equation. (25) with the extracted phase shift of the flat lens with period $P = 1.3 \mu\text{m}$. FDTD simulation is used to estimate the phase from the z-component of the electric field for both the 1D coupled array (in the direction of diameter variation) and the 2D coupled array. From this FDTD phase prediction, it can be concluded that the coupling is negligible along the direction perpendicular to the diameter variation. The focal length f used in Equation. (25) for this design is derived from the FDTD simulation. To calculate the phase response corresponding to each array element analytically, the Lippmann-Schwinger equation [32, 177, 297-299] along with the geometry-dependent polarizability of each element (α) [300] can be used to derive the radiated electric field and consequently the phase shift. The FDTD predicted field intensity distribution demonstrating focusing as predicted is shown in Figure 42b -right. The slight mismatch between the ideal phase distribution and the numerically simulated phase due to the nanostructure diameter and the location variation, which do not exactly follow Equation. (25), result in smaller side lobes in the focal volume, as can be seen in Figure 42b -right.

Lens design parameters

Figure of Merit of Optical Lenses

The figure of merit of any lens is defined by bandwidth, efficiency, focal length and depth of focus. The resistive plasma loss and adiabatic shape variation of this low-Q system makes

the proposed design broadband in nature, which enables the lens to operate across a wide wavelength range as predicted by the FDTD simulation in Figure 43a.

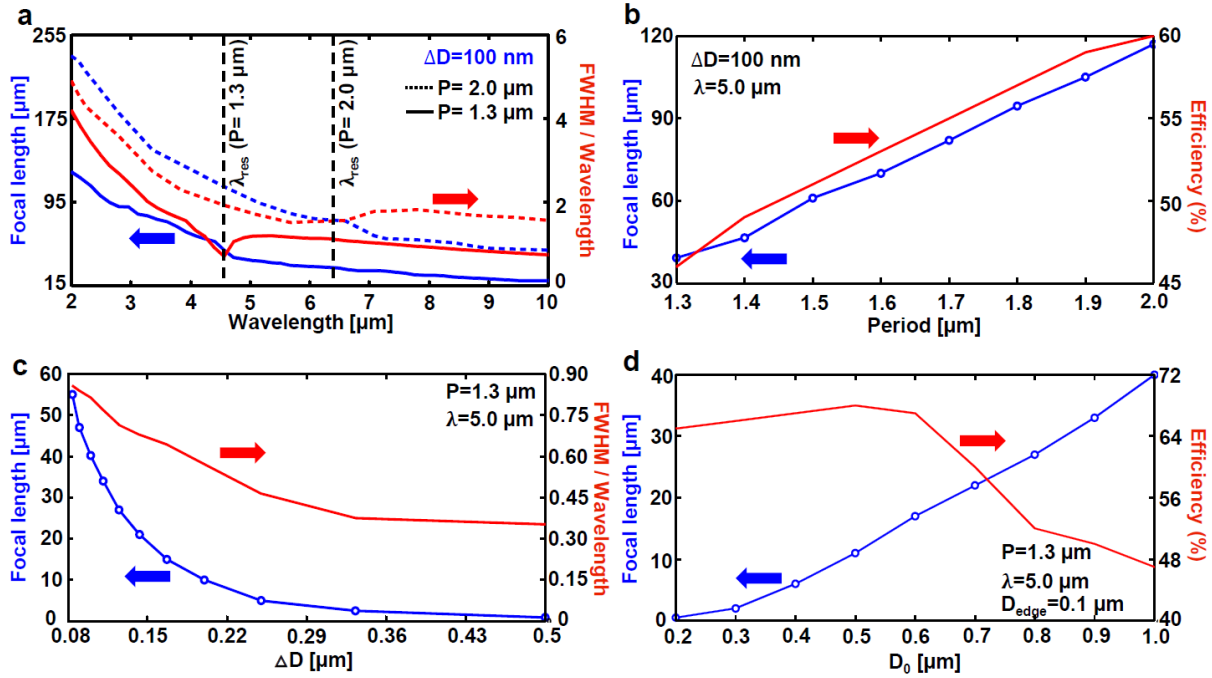


Figure 43: Focal length and efficiency variation.

(a) Focal length (blue line-circle) and FWHM/Wavelength (red line) as functions of the wavelength of the incident light for $P = 1.3 \mu\text{m}$, $\Delta D = 0.1 \mu\text{m}$ and $D_0 = 1 \mu\text{m}$. (b) Focal length (blue line-circle) and efficiency (red line) as functions of the pattern period for $\Delta D = 0.1 \mu\text{m}$, $D_0 = 1 \mu\text{m}$ and $\lambda = 5.0 \mu\text{m}$. (c) Focal length (blue line-circle) and FWHM/Wavelength (red line) as functions of the diameter difference for $P = 1.3 \mu\text{m}$, $D_0 = 1 \mu\text{m}$ and $\lambda = 5.0 \mu\text{m}$. (d) Focal length (blue line-circle) and efficiency (red line) as functions of the central diameter (D_0) for $P = 1.3 \mu\text{m}$, $D_{\text{edge}} = 0.1 \mu\text{m}$ and $\lambda = 5.0 \mu\text{m}$.

The plasmonic surface possesses the unique ability to impedance match with the free-space which reduces back reflection and consequently increases the transmission efficiency. In addition, the efficiency of the designed lens depends on the metallic plasma loss, the period, the diameter and the thickness of metallic elements of the 2D pattern.

Volume of Focal Point

The size of the focal point is characterized by the full width half maximum with respect to the wavelength (FWHM/wavelength), which plays the crucial role in energy concentration at that point and consequently the resolving power of our proposed plasmonic lens. For the present design the FWHM/wavelength is a decaying function of wavelength, reaching the minimum value at the resonance wavelength ($\lambda_{\text{res}} = 4.56 \mu\text{m}$) of the nanostructure and becomes less than 1, sub-wavelength concentration, for higher wavelengths, as shown in Figure 43a. Figure 43a further shows that our proposed flat lens has chromatic aberration for lower wavelengths ($< \lambda_{\text{res}}$), but has almost constant focal length at higher wavelengths ($> \lambda_{\text{res}}$), thereby minimizing the chromatic aberration. These aberrations are much smaller compared to other reported flat lenses [112, 301].

Efficiency of the Flat Lens

Figure 43b shows the predicted efficiency of the flat lens as a function of period P for a fixed differential diameter $\Delta D = 100 \text{ nm}$. The increase in period P of this 2D array not only enhances the efficiency, but also increases the focal length linearly. The larger the period P , the lower is the metallic fill-fraction for a constant ΔD , which reduces loss and hence leads to a higher transmission efficiency. On the other hand, an increase in ΔD at fixed period P and wavelength ($\lambda = 5.0 \mu\text{m}$) leads to a sharper change in the diameter and the phase, giving rise to sub-wavelength concentration FWHM/wavelength (< 1) due to involvement of near-field interference and shorter focal length, as can be seen from Figure 43c. The increase in the central diameter (D_0) at fixed period ($P = 1.3 \mu\text{m}$), wavelength ($\lambda = 5.0 \mu\text{m}$) and the edge diameter (diameter of the last disk, $D_{\text{edge}} = 100 \text{ nm}$) gives rise to larger focal length and lower transmission efficiency, as can be seen

from Figure 43d. To evaluate the chromatic aberration in Figure 43a, a fixed image plane position at the focal point of the resonance wavelength λ_{res} is used as the reference and the FWHMs corresponding to the different wavelengths are calculated at this plane. But in Figure 43c, the FWHM/Wavelength are calculated at the focal point correspond to each ΔD at $\lambda_m = 5\mu\text{m}$.

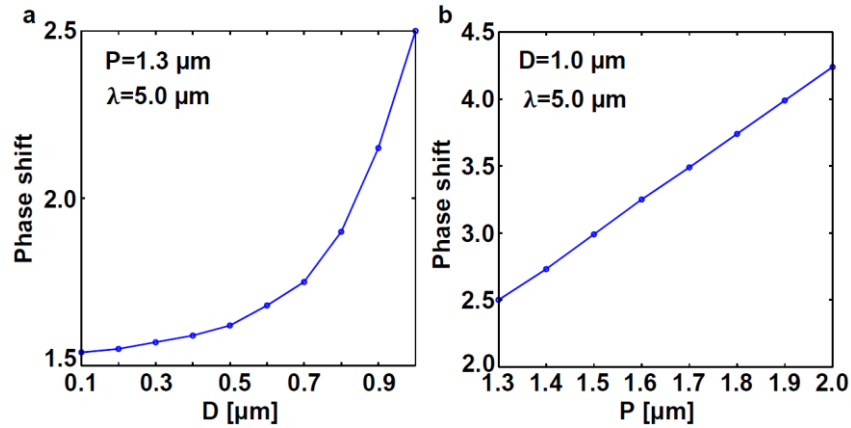


Figure 44: Phase shift.

The phase shift of the nanoantenna element as a function of diameter D in a constant period P (a) and period in a constant diameter D (b).

Focal Length Trend

From Figure 43 it can be concluded that the focal length is a linear function of the period P (Figure 43b), a power function of ΔD (Figure 43c) and a power function of D_0 (Figure 43d), which can be combined into: $F = 113 (P) - 109.6$, $F = 0.9071(\Delta D)^{-1.676} - 3.032$ and $F = 44.13(D_0)^{-1.522} - 4.193$. This set of equations can be easily used to design flat lenses with variable focal length. Based on limitations of the lithography, if we assume $\Delta D_{\text{min}} = 10 \text{ nm}$ and $D_{\text{edge}} = 100 \text{ nm}$, the largest flat lens size for $P = 1.3 \mu\text{m}$ is $\sim 300 \mu\text{m}$ and for $P = 2.0 \mu\text{m}$ is $\sim 800 \mu\text{m}$. Increasing the period P and D_0 gives larger lens sizes, and the corresponding focal length can be calculated using the above-mentioned set of equations.

According to Equation. (25), the focal length depends on the phase shift profile, means $\varphi(x)$ versus x . The phase shift of a nanoantenna element is a linear function of period P and nonlinear function of diameter D , as seen from Figure 44 which is extracted from FDTD simulation. Varying the period while keeping other parameters constant means only the positions of the nanoantenna elements are varying linearly ($x \propto P$), but the number and size of elements are constant. It means according to Equation. (25) and Figure 44, for the zeroth-order ($n = 0$), the focal length should be a linear function of period P , too ($f \propto P$). Unlike the period, as shown in Figure 44b, the phase change is a non-linear function of diameter D . Changing D_0 and ΔD for constant period P , means the number and the size of nanoantenna elements are being changed, while x profile is constant. So, according to Equation. (25) the focal length f is a non-linear function of D_0 and ΔD .

Polarization dependent flat lens

The Effect of Periodicity

To study experimentally the effect of the period P , transmission efficiency and field intensity profile, two flat lenses with different periods ($P = 1.3 \mu\text{m}$ and $P = 2.0 \mu\text{m}$) are fabricated and measured. To increase the overall size of the lens, there can be more than one nanoantenna element with the same diameter instead of gradual decrease in the diameters while maintaining small periods ($P < 2\mu\text{m}$) for sufficient near-field interactions. The SEM images of these two lenses with $D_0 = 1 \mu\text{m}$, $D_{\text{edge}} = 100 \text{ nm}$, $\Delta D = 100 \text{ nm}$ and gold thickness of 45 nm are shown in Figures 45a-left ($P = 1.3 \mu\text{m}$) and 45a-right ($P = 2 \mu\text{m}$). The diffraction-limited confocal measurement technique is used to scan the spatial field intensity. A plane wave light beam with large spot size and uniform power after passing through a linear polarizer, band pass filter ($\lambda_c = 5.0 \mu\text{m}$ with

bandwidth of 70.0 nm) and a pinhole impinges on the sample and a high numerical aperture objective lens (NA~0.9) is coupled to a FTIR spectrometer to collect photons. A 3D automatic stage is used to change the position of the flat lens sample to scan the focal point, and the light is collected using an objective lens and a mercury cadmium telluride (MCT) photodetector, as schematically shown in Figure 46.

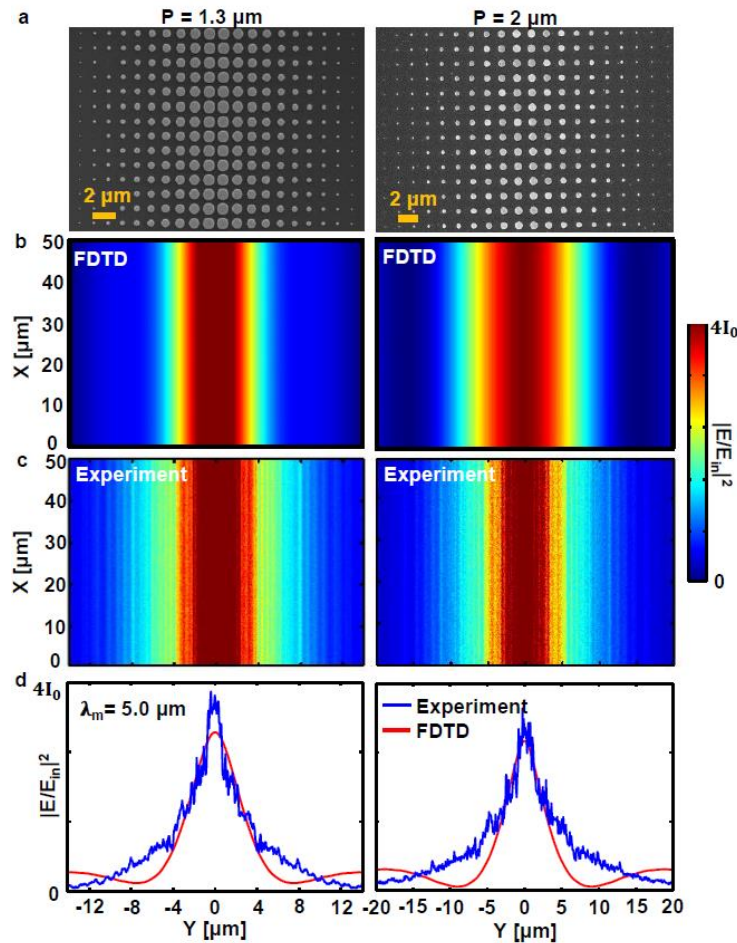


Figure 45: SEM image and top view of electric field intensity at focus of the single layer flat lens.

(a) SEM image of the plasmonic lens with the period of $P = 1.3 \mu\text{m}$ (left) and $P = 2.0 \mu\text{m}$ (right). (b-c) The simulated (b) and the measured (c) cross sections of the light field intensities in X-Y plane for the plasmonic lenses with $P = 1.3 \mu\text{m}$ (left) and $P = 2.0 \mu\text{m}$ (right). (d) Comparison of the simulated (red) and measured (blue) of the cross sections of the light intensities along Y-axis for the patterns with $P = 1.3 \mu\text{m}$ (left) and $P = 2.0 \mu\text{m}$ (right). The operating wavelength is $\lambda_m = 5.0 \mu\text{m}$.

The applied mesh in FDTD simulation is 10 nm in x-y direction and 5 nm in z direction. The intensity accuracy is 0.01 ($1/100 I_0$). In the measurement, the focal spot of the objective lens is $\sim 6 \mu\text{m}$ and the step size of the 3D stage is 100 nm. A high sensitive MCT photodetector working at $77 \text{ }^\circ\text{C}$ is used for photon collection.

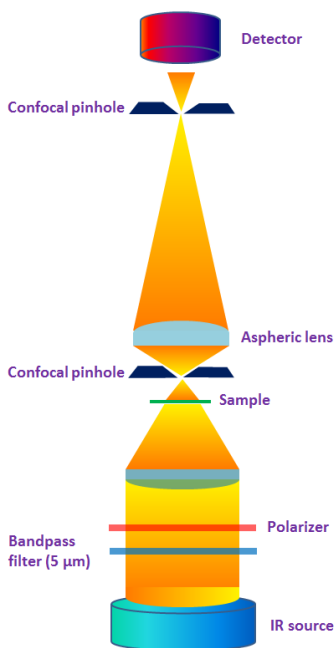


Figure 46: Schematic of the confocal measurement method.

Confocal Measurement

In the confocal measurement, the 3-dimensional field intensity of the focal point is scanned by using a 3D automatic motor. A bandpass filter for $\lambda = 5.0 \mu\text{m}$ with the bandwidth of 70 nm along with a linear polarizer is located in front of the infrared source of FTIR. An aspheric lens with low numerical aperture ($\text{NA} = 0.2$) is used to focus the light beam uniformly on the sample which is attached to a 3D automatic motor. A high NA aspheric lens ($\text{NA} = 0.9$) between two

confocal pinholes is utilized to collect the transmitted photons and send them to a cooled MCT. The scanning, measurement and motor motion are controlled by a Labview program.

Field Intensity of the Focal Line

Figures 45b and 45c compare the FDTD predicted and the measured field intensity in the cross-section of the focal volume at the x-y plane (top view) for the two lenses, respectively. Since the single layer flat lens can only focus the TE mode light, there is a focal line instead of focal point, and the results show very good agreement between the FDTD prediction and experimental measurement. From these plots it can also be observed that the larger period P gives rise to larger FWHM. The increase in the period P decreases the metallic fill-fraction and consequently the plasmonic light-matter interactions. This in turn reduces the amount of transmitted light which accumulates phase shift, leading to a larger focal volume or FWHM.

For quantitative comparison, the simulated and measured field intensity in the cross-section of the focal line along y-axis are overlaid in Figs. 45d-left ($P = 1.3 \mu\text{m}$) and 45d-right ($P = 2.0 \mu\text{m}$), which show a good match between simulation and measurement for both lenses. In order to reveal the focal volume, the cross-section of the focal line in the y-z plane (side view) is scanned and compared with the FDTD-predictions, as shown in Figures 47a-b for both patterns ($P = 1.3 \mu\text{m}$ and $P = 2.0 \mu\text{m}$).

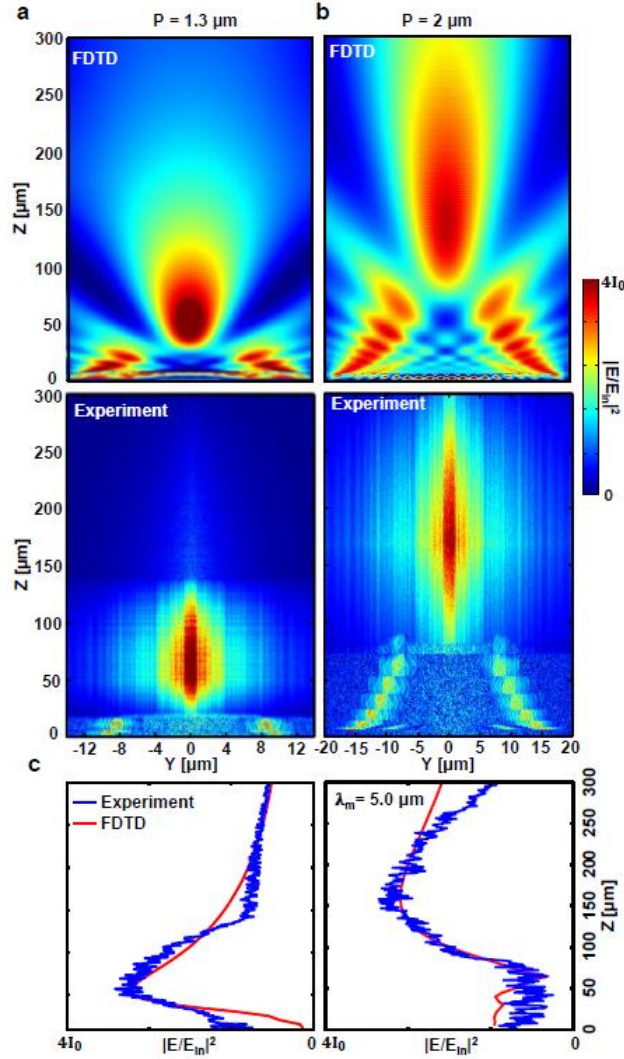


Figure 47: Focal point measurement of the single layer flat lens.

(a-b) The simulated (a) and the measured (b) cross section of the light field intensity in Y-Z plane for the plasmonic lens with $P = 1.3 \mu\text{m}$ (left) and $P = 2.0 \mu\text{m}$ (right). (c) Comparison of the simulated (red) and measured (blue) cross section of the light intensity along Z-axis for the patterns with $P = 1.3 \mu\text{m}$ (left) and $P = 2.0 \mu\text{m}$ (right). The operating wavelength is $\lambda_m = 5.0 \mu\text{m}$.

The presence of side lobes is due to the mismatch between the ideal phase predicted by Equation (25) and the actual phase response of the designed plasmonic pattern. Similar to the cross-section of the field intensity in y-direction (Figure 45), the simulated and measured field intensity along z-axis are overlaid in Figures 47c-left ($P = 1.3 \mu\text{m}$) and 47c-right ($P = 2.0 \mu\text{m}$) with good agreement

for both periods. Minor discrepancies are mainly due to the fabrication tolerances, finite diffraction-limited confocal measurement and the IR detector shot noise.

Polarization independent flat lens

The Advantages of Double-layer Flat Lens

The unique feature of the proposed design is that when two such lenses are stacked together with an optimum spacing between them, as schematically shown in Figure 48a-top, the resulting bi-layer flat lens with 90° rotated layers functions as a polarization independent point focusing lens with the ability of funneling both TE and TM modes of the incident light. The double-layer lens has two main advantages compared to concentric design. The first one is that it makes it possible to control the focal length for each polarization, independently, which gives a great degree of freedom to design novel polarization-dependent flat lens. Possibility of removing oblique and coma aberrations is another advantage of this design. The second layer can be designed such that the rays coming from off-axis light source do not directed away from the optical axis.

Fabrication

The one-layer flat lens is patterned on a bilayer electron resist (MMA/PMMA) spin-coated on silicon wafer (100 μm thickness), which has more than 70% transmission in mid-IR wavelengths, using electron beam lithography, developed in MIBK/IPA (3:1) following by deposition of Ti/Au (3 nm/45 nm) and lift-off process.

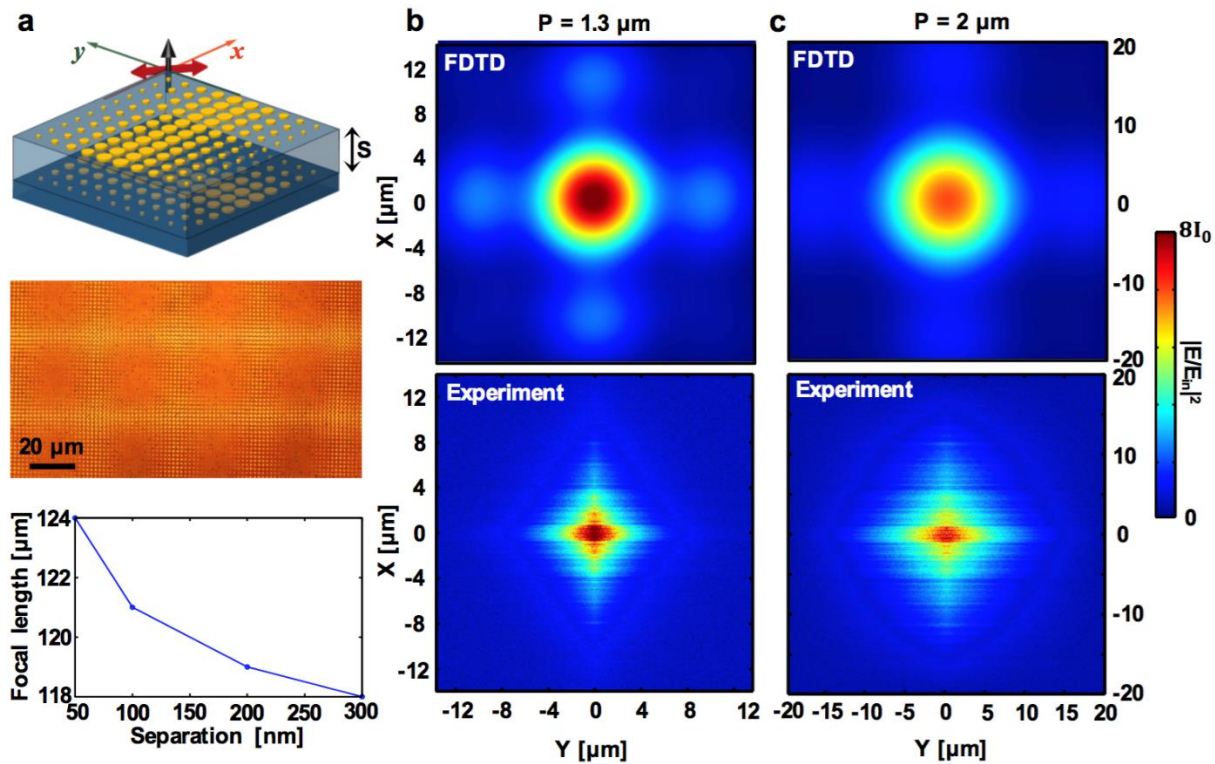


Figure 48: Focal point measurement of the polarization independent bilayer flat lens.

(a) (top) The schematic of the bilayer plasmonic lens in presence of incident linear 45°-polarized light. (middle) The optical image of the fabricated bilayer plasmonic lens. (bottom) Focal length as function of the separation distance of bilayer plasmonic lens for $P = 2.0 \mu\text{m}$, $\Delta D = 0.1 \mu\text{m}$ and $D_0 = 1 \mu\text{m}$ at $\lambda = 5.0 \mu\text{m}$. The simulated (top) and the measured (bottom) cross section of the light field intensity in X-Y plane for the bilayer flat lens with the period of $P = 1.3 \mu\text{m}$ (b) and $P = 2.0 \mu\text{m}$ (c).

Using a bilayer electron resist helps to lift-off the remaining resist without sonication and damaging the nanostructure. To fabricate the bilayer flat lens, after patterning MMA/PMMA on silicon (100 μm) substrate by EBL, following by Ti/Au (3 nm/45 nm) deposition and lift-off process, a layer of SU-8 polymer with thickness of 200 nm which has low light absorption in mid-IR is spin-coated on the fabricated layer following by 2 hours UV exposure and one-hour baking (95°C) to become hard enough against polymer solvent (acetone) and decrease light absorption. A

thin layer of Al_2O_3 (20 nm) is deposited on this layer to spin-coat a uniform layer of MMA/PMMA on that and patterning it with EBL.

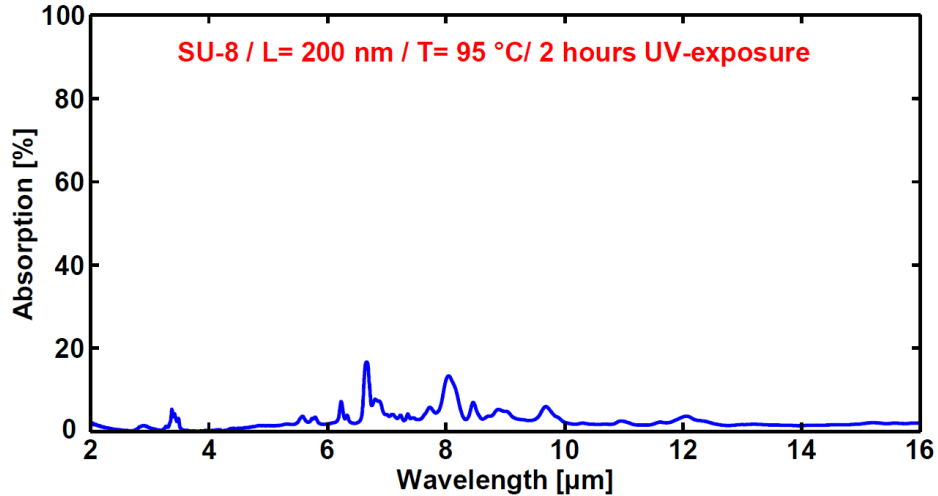


Figure 49: The light absorption spectrum of SU-8 polymer.

Due to the ease of interface finding, silicon wafer is used to fabricate the pattern using electron-beam lithography. But it is possible to use an IR transparent substrate such as sapphire instead to increase the light transmission to more than 95%. To fabricate the pattern on top of that, the nanoimprint lithography can be used to decrease the cost and increase throughput. Four markers are used to write the next layer exactly 90° rotated with respect to the first layer. Another Ti/Au (3 nm/45 nm) deposition and lift-off process is done to prepare the bilayer flat lens.

The optical image of the fabricated bi-layer lens is shown in Figure 48a-middle. Since the separation distance between these two layers is 200 nm, their focal lengths are almost the same, which leads to the creation of a single focal point for an arbitrary linearly polarized light. Furthermore, the decrease in the separation distance does not have a prominent effect on the focal length, which means that the far-field coupling between these layers does not change their focal

lengths substantially, but enhances the transmission efficiency a bit, as can be seen from Figures 48a-bottom and 49.

Filed Intensity of the Focal Point

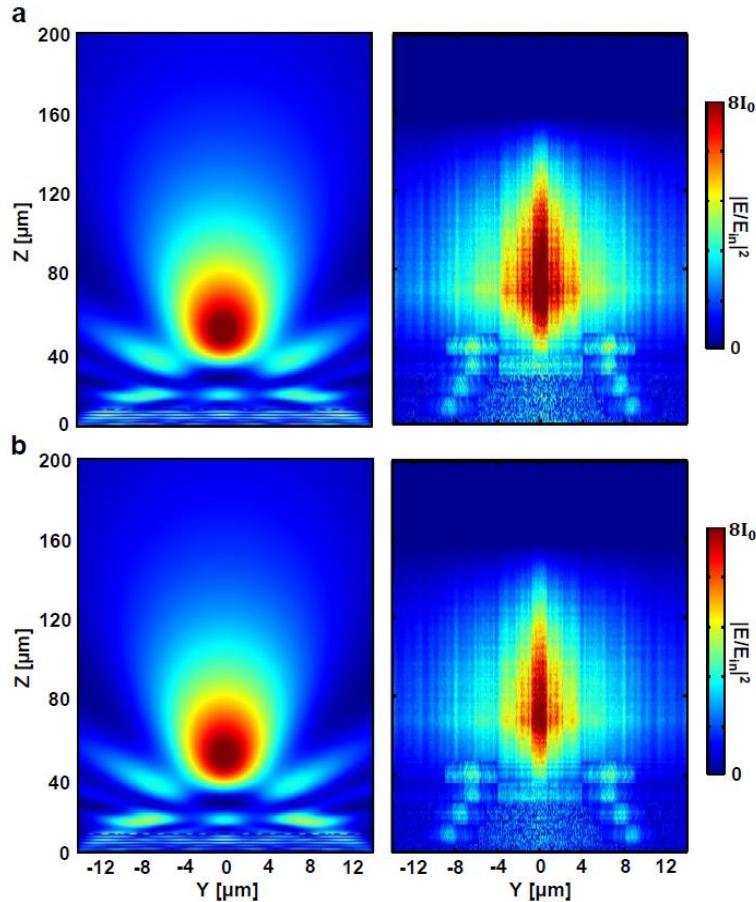


Figure 50: Comparison of the focal point in X-Z and Y-Z planes for the bi-layer lens with $P=1.3 \mu\text{m}$.

(a) The FDTD simulated (left) and measured cross section of the field intensity of the focal volume in y-z plane for the flat lens with period of $P= 1.3 \mu\text{m}$. (b) The FDTD simulated (left) and measured cross section of the field intensity of the focal volume in x-z plane for the flat lens with period of $P= 1.3 \mu\text{m}$.

Figures 48b and 48c compare the cross-section of the simulated and measured field intensity in the x-y plane (top view) for 45° linear polarized normal incident light. Comparison of Figures 48b and 48c not only proves the polarization-independency of the bi-layer flat lens, but

also shows that the increase in the period P gives rise to larger focal volume, similar to the single layer lens. In Figure 48, the simulated focal points are close to circle, while the measured ones look like a cross-like. There are two reasons for this effect which are related to the fabrication.

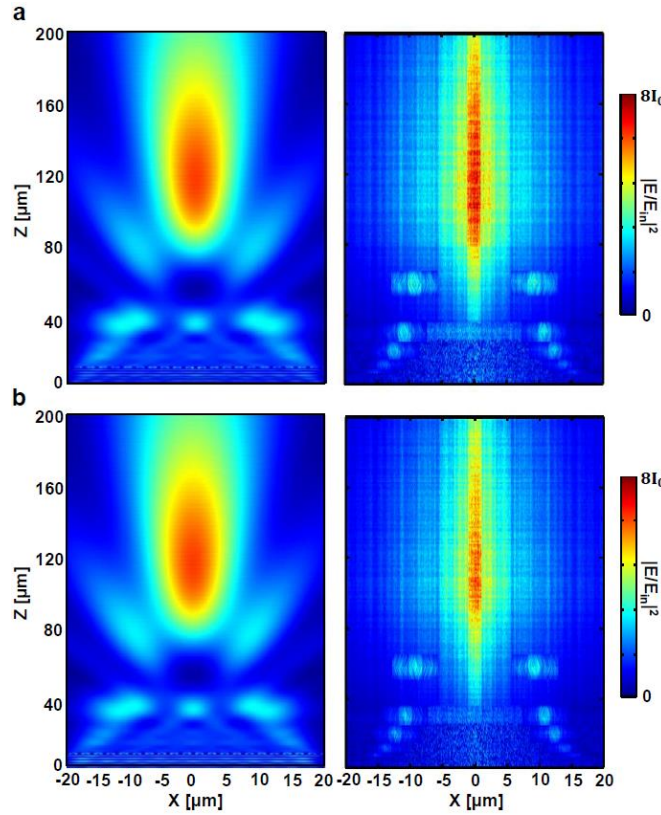


Figure 51: Comparison of the focal point in X-Z and Y-Z planes for the bi-layer lens with $P=2.0 \mu\text{m}$.

The first one is the misalignment between the first and second layers which creates discrepancy between simulation and the fabrication. Another reason is that the electron beam lithography system for writing any pattern needs to find the interface by using a laser beam. But due to the non-reflective dielectric spacer on top of the first layer, it finds the interface improperly. It means the second layer is a little bit different from the perfect pattern leading to the discrepancy between the simulation (ideal circle) and measurement (cross-like).

Figures 50 and 51 show the simulated and measured cross-sectional field intensity in the y-z and x-z plane (side view), which clearly show the same focal length and focus pattern for the perpendicular planes, thereby proving the polarization-independency of such a bi-layer flat lens. Comparing Figures 45, 47, 48 and 50-51, it is evident that the bi-layer lens further reduces the FWHM due to the double excitation of plasmon resonances passing through two layers (FWHM/Wavelength = 1.03/0.87 [single layer/bilayer] for $P = 1.3 \mu\text{m}$ and = 1.20/1.05 [single layer/bilayer] for $P = 2.0 \mu\text{m}$ at $\lambda = 5.0 \mu\text{m}$).

Any type of flat lens with continuous or discrete phase distribution has the monochromatic aberration like coma for the oblique or non-normal illumination. It means for an ideal Airy disc object the resultant image would be a comet-like spot similar to other singlet lenses. For having an optical lens free from coma and spherical aberrations, the Abbe sine condition should be established which means the ratio between the sine of the angle of the ray radiated from the object and the sine of the angle of the same ray reaching to the image should be constant for the rays. The optical lens which is designed to overcome both spherical and coma aberrations is aplanatic lens which is patterned on a spherical interface and used commonly in optical microscopes [126, 302, 303]. Here, the double-layer flat lens can be modified as an aplanatic lens, such that the first layer is designed to behave like the spherical interface for the second layer. For the current design, since the first layer has a cylindrical focal line, under certain conditions it can satisfy the Abbe sine condition and decrease the spherical and coma aberrations which are two different types of monochromatic aberrations.

Transmission efficiency

A crucial parameter of any type of optical lens is the amount of incident light that is focused in the forward direction is called transmission efficiency of the lens.

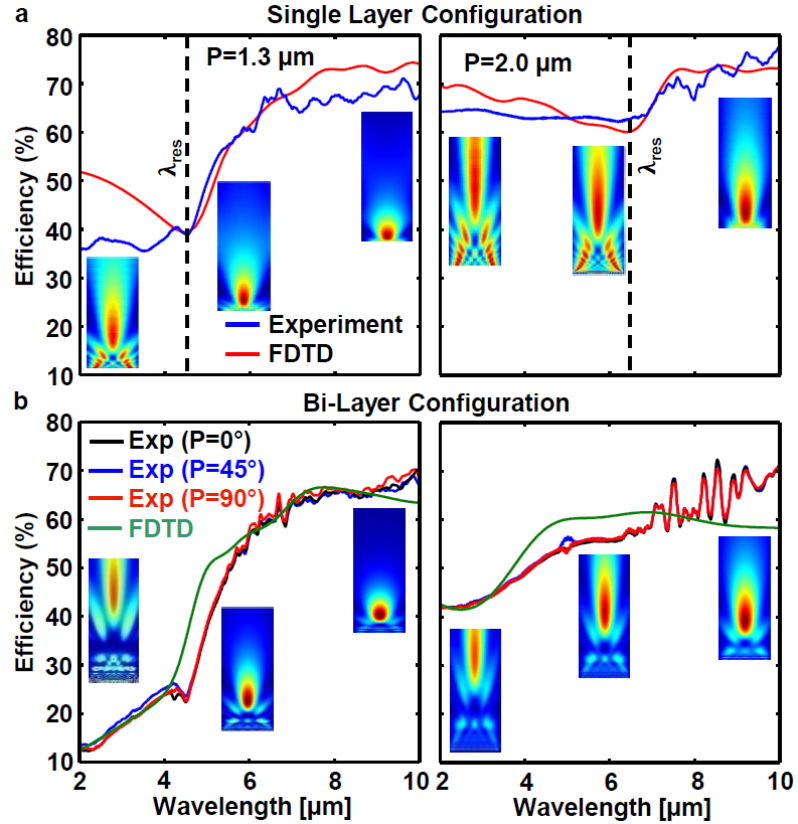


Figure 52: Transmission efficiency.

(a) The simulated (red) and the measured (blue) transmission efficiencies of the single layer plasmonic lenses with the periods of $P = 1.3 \mu\text{m}$ (left) and $P = 2.0 \mu\text{m}$ (right). (b) The simulated (green) and the measured (Polarization = 0° (black), 45° (blue) and 90° (red)) transmission efficiencies of the bilayer plasmonic lenses with the periods of $P = 1.3 \mu\text{m}$ (left) and $P = 2.0 \mu\text{m}$ (right).

Conventional refractive lens based on CaF_2 can reach $< 95 \%$ up to $\lambda = 6 \mu\text{m}$ and based on ZnSe can reach $< 70 \%$ up to $\lambda = 16 \mu\text{m}$ [Janis Research Company, LLC]. However, our proposed plasmonic flat lens does not allow such high transmission efficiency due to the metallic loss but enable almost aberration free subwavelength focusing with extremely low planar physical footprint ($\ll \lambda$). As predicted in Figure 43b, the present design allows higher transmission efficiency with larger pattern period P due to the lower metallic fill-fraction. Furthermore, due to the reduced near-

field and far-field interactions between plasmonic nanoantennas with the increase in period P , there is a red shift in the resonance wavelength pushing the lowest transmission at the resonance wavelength ($\lambda_{\text{res}} = 6.5 \mu\text{m}$) away from the designed wavelength ($\lambda = 5.0 \mu\text{m}$). However, the larger period P shifts the focal length to higher values due to the wider phase response distribution according to Equation. (25) and the weakening of coupling between neighboring disks, as can be observed in Figure 43b.

Figure 52a overlays the simulated and the measured transmission efficiencies of the single layer flat lenses with $P = 1.3 \mu\text{m}$ (left) and $P = 2.0 \mu\text{m}$ (right). Comparison of these two plots not only validates the simulated results, but also proves that the increase in the period enhances the transmission efficiency, besides keeping the focusing effect, which is shown by the cross section of field intensity in the y - z plane for different wavelengths. At the wavelengths above resonance, a broadband transmission efficiency higher than 60% is achieved, which is much higher compared to the other reported metasurface-based flat lenses operating in the mid-IR spectral range [17, 92]. Figure 52b shows the measured transmission efficiency of the bi-layer lens at the focal point for different linear-polarized incident light ($\text{pol} = 0^\circ, 45^\circ$ and 90°), which closely matches with the FDTD prediction of transmission of 0° linear-polarized light. Near perfect overlap between these plots further validates polarization-independency of this bilayer lens. Minor discrepancies originate from the mismatch between the alignment of the two layers during fabrication compared to the simulated supercell. Similar to the single layer plasmonic lens, the increase in the period P gives rise to higher transmission efficiency while maintaining focusing effect for the entire mid-IR wavelengths, as can be observed in Figure 52b. The bilayer flat lens acts like a spherical lens with ultrathin thickness ($\sim 300 \text{ nm}$), the focal volume of which is further tunable by geometrical parameters of two independent layers over broad spectral range. In order

to calculate the transmission efficiency from simulation and measurement, the incident light is taken as the reference and the amount of light transmitted at the focal point with respect to that reference has been considered as the transmission efficiency. This means the reflection loss from the first interface of the substrate has been contributed in the efficiency calculation.

Conclusion

In conclusion, various, planar lenses are demonstrated following the diffractive optics concept of phase control based on dielectric scatterers on a 2D plane. However, in the mid-infrared wavelength range (3-16 μm) such engineered dielectric surfaces are not possible due to the low spectral bandwidth and high thermal noise in long wavelengths. Plasmonic nanostructures enable abrupt change in phase, amplitude and polarization of the incident light using subwavelength optical scatterer on a planar surface. I demonstrated a novel flat plasmonic lens based on gold in single and bi-layer geometry to focus polarized and unpolarized light beams. The focal length and spot size are tunable with geometrical parameters providing design flexibility. The gradient design offers unique broadband near aberration free operation unlike other flat lenses. The design enables sub-wavelength focusing beyond the Abbe-Rayleigh diffraction limit while maintaining high transmission efficiency (~60%) with excellent agreement between electromagnetic simulations and confocal measurements. High transmission efficiency compared to the current flat lenses along with low FWHM of the focal point and ultrathin thickness make this lens a right candidate for the compact thermal imaging systems and photonic integrated circuits.

**APPENDIX A:
PUBLISHER'S PERMISSION**

Michele Hake (APS)

Jan 14, 15:58 EST

Date: 14Jan2019 11:52:49

From: Alireza Safaei alireza.safaei@knights.ucf.edu

Subject: Request for permission

To: "prb@aps.org" prb@aps.org

Dear Editor,

I am writing to request your permission for me to use a published article in Physical Review B in which I am the leading author. I am completing a doctoral dissertation degree at the University of Central Florida entitled "Nanoplasmonics in two-dimensional Dirac and three-dimensional metallic nanostructure systems". I would like your permission to reprint in my thesis/dissertation excerpts from the following:

Alireza Safaei, Sayan Chandra, Abraham Vázquez-Guardado, Jean Calderon, Daniel Franklin, Laurene Tetard, Lei Zhai, Michael N. Leuenberger, and Debashis Chanda, "Extraordinary Tunable Light Absorption in Monolayer Graphene," Physical Review B, Vol. 96, pp. 165431, 2017.

It would be great to read and sign the attached letter. Please fill the places where I mentioned in blue color.

Sincerely,

Alireza Safaei,

University of Central Florida,

4000 Central Florida Blvd. Orlando, Florida, 32816,

alireza.safaei@knights.ucf.edu

Michele Hake (APS)

Jan 14, 15:59 EST

Dear Dr. Safaei,

Thank you for writing. Kindly refer to our Copyright FAQ located at <https://journals.aps.org/copyrightFAQ.html>, specifically:

Q) - "As the author of an APS-published article, may I include my article or a portion of my article in my thesis or dissertation?"

A) - "Yes, the author has the right to use the article or a portion of the article in a thesis or dissertation without requesting permission from APS, provided the bibliographic citation and the APS copyright credit line are given on the appropriate pages."

I hope this is helpful to you.

Sincerely,

Michele Hake

help@aps.org

**APPENDIX B:
PUBLISHER'S PERMISSION**

**RightsLink**®[Home](#)[Account Info](#)[Help](#)

Title: Wide Angle Dynamically Tunable Enhanced Infrared Absorption on Large-Area Nanopatterned Graphene

Logged in as:
Alireza Safaei

[LOGOUT](#)

Author: Alireza Safaei, Sayan Chandra, Michael N. Leuenberger, et al

Publication: ACS Nano

Publisher: American Chemical Society

Date: Dec 1, 2018

Copyright © 2018, American Chemical Society

PERMISSION/LICENSE IS GRANTED FOR YOUR ORDER AT NO CHARGE

This type of permission/license, instead of the standard Terms & Conditions, is sent to you because no fee is being charged for your order. Please note the following:

- Permission is granted for your request in both print and electronic formats, and translations.
- If figures and/or tables were requested, they may be adapted or used in part.
- Please print this page for your records and send a copy of it to your publisher/graduate school.
- Appropriate credit for the requested material should be given as follows: "Reprinted (adapted) with permission from (COMPLETE REFERENCE CITATION). Copyright (YEAR) American Chemical Society." Insert appropriate information in place of the capitalized words.
- One-time permission is granted only for the use specified in your request. No additional uses are granted (such as derivative works or other editions). For any other uses, please submit a new request.

**APPENDIX C:
PUBLISHER'S PERMISSION**

RE: Request for permission

pubscopyright <copyright@osa.org>

Thu 1/24/2019 4:48 PM

To: Alireza Safaei <alireza.safaei@knights.ucf.edu>; pubscopyright <copyright@osa.org>;

Dear Alireza Safaei,

Thank you for contacting The Optical Society.

For the use of material from **[1]** Alireza Safaei, Sushrut Modak, Jonathan Lee, Sayan Chandra, Daniel Franklin, Abraham Vázquez-Guardado, and Debashis Chanda, "Multi-spectral frequency selective mid-infrared microbolometers," Opt. Express 26, 32931-32940 (2018) and **[2]** Alireza Safaei, Sushrut Modak, Abraham Vázquez-Guardado, Daniel Franklin, and Debashis Chanda, "Cavity-induced hybrid plasmon excitation for perfect infrared absorption," Opt. Lett. 43, 6001-6004 (2018):

Because you are the author of the source paper from which you wish to reproduce material, OSA considers your requested use of its copyrighted materials to be permissible within the author rights granted in the Copyright Transfer Agreement submitted by the requester on acceptance for publication of his/her manuscript. It is requested that a complete citation of the original material be included in any publication. This permission assumes that the material was not reproduced from another source when published in the original publication.

While your publisher should be able to provide additional guidance, OSA prefers the below citation formats:

For citations in figure captions:

[Reprinted/Adapted] with permission from ref [x], [Publisher]. (with full citation in reference list)

For images without captions:

Journal Vol. #, first page (year published) An example: Opt. Lett. 43, 6001 (2018)

OSA considers this email to be sufficient authorization for the use of the requested material.

Please let me know if you have any questions.

Kind Regards,

Rebecca Robinson

Rebecca Robinson
January 24, 2019
Authorized Agent, The Optical Society

The Optical Society (OSA)
2010 Massachusetts Ave., NW
Washington, DC 20036 USA
www.osa.org

Reflecting a Century of Innovation



**APPENDIX D:
PUBLISHER'S PERMISSION**

WG: Request for permission (adom.201800216 for dissertation)

Rights DE <RIGHTS-and-LICENCES@wiley-vch.de>

Tue 1/15/2019 5:34 AM

To: Alireza Safaei <alireza.safaei@knights.ucf.edu>;

Dear Editor,

I am writing to request your permission for me to use a published article in Advanced Optical Materials in which I am the leading author. I am completing a doctoral dissertation degree at the University of Central Florida entitled "Nanoplasmonics in two-dimensional Dirac and three-dimensional metallic nanostructure systems". I would like your permission to reprint in my thesis/dissertation excerpts from the following:

Alireza Safaei, Abraham Vázquez-Guardado, Daniel Franklin, Michael N Leuenberger, and Debashis Chanda, "High-Efficiency Broadband Mid-Infrared Flat Lens," Advanced Optical Materials, Vol. 6, 1800216, 2018.

The requested permission extends to any future revisions and editions of my thesis/dissertation, including non-exclusive world rights in all languages. These rights will in no way restrict republication of the material in any other form by you or by others authorized by you. Your signing of this letter will also confirm that you own or your company owns the copyright to the above-described material.

If these arrangements meet with your approval, please sign this letter where indicated below and return it to me in the enclosed return envelope. Thank you for your attention in this matter.

Sincerely,

Alireza Safaei,
University of Central Florida,
4000 Central Florida Blvd. Orlando, Florida, 32816,
alireza.safaei@knights.ucf.edu

We hereby grant permission for the requested use expected that due credit is given to the original source.

If material appears within our work with credit to another source, authorisation from that source must be obtained.

Credit must include the following components:

- Journals: Author(s) Name(s); Title of the Article. Name of the Journal. Publication year. Volume. Page(s). Copyright Wiley-VCH Verlag GmbH & Co. KGaA. Reproduced with permission.

If you also wish to publish your thesis in electronic format, you may use the article according to the Copyright transfer agreement:

3. Final Published Version.

Wiley-VCH hereby licenses back to the Contributor the following rights with respect to the final published version of the Contribution:

a. [...]

b. Re-use in other publications. The right to re-use the final Contribution or parts thereof for any publication authored or edited by the Contributor (excluding journal articles) where such re-used material constitutes less than half of the total material in such publication. In such case, any modifications should be accurately noted.

Kind regards

Bettina Loycke
Senior Rights Manager
Rights & Licenses

Wiley-VCH Verlag GmbH & Co. KGaA
Boschstraße 12
69469 Weinheim
Germany
www.wiley-vch.de

T + (49) 6201 606-280
F + (49) 6201 606-332
rightsDE@wiley.com

WILEY

LIST OF REFERENCES

1. H. P. Paudel, A. Safaei, and M. N. Leuenberger, "Nanoplasmonics in Metallic Nanostructures and Dirac Systems," in *Nanoplasmonics - Fundamentals and Applications*, D. G. Barbillon, ed. (InTech, 2017).
2. A. Safaei, S. Chandra, M. N. Leuenberger, and D. Chanda, "Wide Angle Dynamically Tunable Enhanced Infrared Absorption on Large-Area Nanopatterned Graphene," *ACS nano* (2018).
3. A. Safaei, S. Modak, A. Vazquez-Guardado, D. Franklin, and D. Chanda, "Cavity-induced hybrid plasmon excitation for perfect infrared absorption," *Optics letters* **43**, 6001-6004 (2018).
4. A. Safaei, S. Modak, J. Lee, S. Chandra, D. Franklin, A. Vázquez-Guardado, and D. Chanda, "Multi-spectral frequency selective mid-infrared microbolometers," *Optics express* **26**, 32931 (2018).
5. D. Franklin, S. Modak, A. Vazquez-Guardado, A. Safaei, and D. Chanda, "Covert infrared image encoding through imprinted plasmonic cavities," *Light, science & applications* **7**, 93 (2018).
6. A. Vazquez-Guardado, A. Safaei, S. Modak, D. Franklin, and D. Chanda, "Hybrid coupling mechanism in a system supporting high order diffraction, plasmonic, and cavity resonances," *Phys Rev Lett* **113**, 263902 (2014).
7. S. Chandra, D. Franklin, J. Cozart, A. Safaei, and D. Chanda, "Adaptive Multispectral Infrared Camouflage," *ACS Photonics* (2018).
8. D. Chanda, A. Safaei, and M. N. Leuenberger, "Optical detector device with patterned graphene layer and related methods," (2018).
9. D. Chanda, S. Modak, J. Lee, and A. Safaei, "Optical Frequency-Selective Absorber-based Infrared Detector, Methods, and Applications," (2018).
10. A. Safaei, A. Vázquez-Guardado, D. Franklin, M. N. Leuenberger, and D. Chanda, "High-Efficiency Broadband Mid-Infrared Flat Lens," *Advanced Optical Materials*, 1800216 (2018).
11. A. Safaei, S. Chandra, A. Vázquez-Guardado, J. Calderon, D. Franklin, L. Tetard, L. Zhai, M. N. Leuenberger, and D. Chanda, "Dynamically tunable extraordinary light absorption in monolayer graphene," *Physical Review B* **96**(2017).
12. A. Safaei, S. Chandra, M. N. Leuenberger, and D. Chanda, "Wide Angle Dynamically Tunable Enhanced Infrared Absorption on Large Area Nanopatterned Graphene " arxiv: 1806.00837 (2018).
13. R. Fleury and A. Alù, "Enhanced superradiance in epsilon-near-zero plasmonic channels," *Physical Review B* **87**(2013).
14. A. Alù, M. G. Silveirinha, A. Salandrino, and N. Engheta, "Epsilon-near-zero metamaterials and electromagnetic sources: Tailoring the radiation phase pattern," *Physical Review B* **75**(2007).
15. E. Brian, A. Andrea, E. Y. Michael, S. Mário, and E. Nader, "Experimental Verification of Epsilon-Near-Zero Metamaterial Coupling and Energy Squeezing Using a Microwave Waveguide," *Physical review letters* **100**(2008).

16. Y. Yao, R. Shankar, M. A. Kats, Y. Song, J. Kong, M. Loncar, and F. Capasso, "Electrically tunable metasurface perfect absorbers for ultrathin mid-infrared optical modulators," *Nano Lett* **14**, 6526-6532 (2014).
17. N. Yu and F. Capasso, "Flat optics with designer metasurfaces," *Nature materials* **13**, 139-150 (2014).
18. Y. Takahashi and T. Tatsuma, "Solid state photovoltaic cells based on localized surface plasmon-induced charge separation," *Applied Physics Letters* **99**, 182110 (2011).
19. H. A. Atwater and A. Polman, "Plasmonics for improved photovoltaic devices," *Nature materials* **9**, 205-213 (2010).
20. M. Furchi, A. Urich, A. Pospischil, G. Lilley, K. Unterrainer, H. Detz, P. Klang, A. M. Andrews, W. Schrenk, G. Strasser, and T. Mueller, "Microcavity-integrated graphene photodetector," *Nano Lett* **12**, 2773-2777 (2012).
21. D. K. Efetov, R. J. Shiue, Y. Gao, B. Skinner, E. D. Walsh, H. Choi, J. Zheng, C. Tan, G. Grosso, C. Peng, J. Hone, K. C. Fong, and D. Englund, "Fast thermal relaxation in cavity-coupled graphene bolometers with a Johnson noise read-out," *Nature nanotechnology* (2018).
22. X. Gan, R. J. Shiue, Y. Gao, K. F. Mak, X. Yao, L. Li, A. Szep, D. Walker, Jr., J. Hone, T. F. Heinz, and D. Englund, "High-contrast electrooptic modulation of a photonic crystal nanocavity by electrical gating of graphene," *Nano Lett* **13**, 691-696 (2013).
23. R. Ameling and H. Giessen, "Microcavity plasmonics: strong coupling of photonic cavities and plasmons," *Laser Photonics Rev* **7**, 141-169 (2013).
24. S. A. Maier, "Plasmonics: Fundamentals and applications," (2007).
25. B. Auguie and W. L. Barnes, "Collective resonances in gold nanoparticle arrays," *Phys Rev Lett* **101**, 143902 (2008).
26. S. Zou, N. Janel, and G. C. Schatz, "Silver nanoparticle array structures that produce remarkably narrow plasmon lineshapes," *The Journal of chemical physics* **120**, 10871-10875 (2004).
27. S. Thongrattanasiri and F. J. Garcia de Abajo, "Optical field enhancement by strong plasmon interaction in graphene nanostructures," *Phys Rev Lett* **110**, 187401 (2013).
28. D. Sun, G. Aivazian, A. M. Jones, J. S. Ross, W. Yao, D. Cobden, and X. Xu, "Ultrafast hot-carrier-dominated photocurrent in graphene," *Nature nanotechnology* **7**, 114-118 (2012).
29. R. Sundararaman, P. Narang, A. S. Jermyn, W. A. Goddard, 3rd, and H. A. Atwater, "Theoretical predictions for hot-carrier generation from surface plasmon decay," *Nature communications* **5**, 5788 (2014).
30. J. C. Song, M. S. Rudner, C. M. Marcus, and L. S. Levitov, "Hot carrier transport and photocurrent response in graphene," *Nano Lett* **11**, 4688-4692 (2011).
31. C. H. Liu, Y. C. Chang, T. B. Norris, and Z. H. Zhong, "Graphene photodetectors with ultra-broadband and high responsivity at room temperature," *Nature nanotechnology* **9**, 273-278 (2014).
32. A. B. Evlyukhin, G. Brucoli, L. Martin-Moreno, S. I. Bozhevolnyi, and F. J. Garcia-Vidal, "Surface plasmon polariton scattering by finite-size nanoparticles," *Physical Review B* **76**(2007).
33. M. Freitag, T. Low, W. Zhu, H. Yan, F. Xia, and P. Avouris, "Photocurrent in graphene harnessed by tunable intrinsic plasmons," *Nature communications* **4**, 1951 (2013).

34. N. R. W. Z. Engheta, "Metamaterials: Physics and Engineering Explorations," (Wiley & Sons, 2006).
35. M. Jablan, H. Buljan, and M. Soljacic, "Plasmonics in graphene at infrared frequencies," *Physical Review B* **80**(2009).
36. F. H. Koppens, D. E. Chang, and F. J. Garcia de Abajo, "Graphene plasmonics: a platform for strong light-matter interactions," *Nano Lett* **11**, 3370-3377 (2011).
37. Z. Fei, A. S. Rodin, G. O. Andreev, W. Bao, A. S. McLeod, M. Wagner, L. M. Zhang, Z. Zhao, M. Thiemens, G. Dominguez, M. M. Fogler, A. H. Castro Neto, C. N. Lau, F. Keilmann, and D. N. Basov, "Gate-tuning of graphene plasmons revealed by infrared nano-imaging," *Nature* **487**, 82-85 (2012).
38. A. Y. Nikitin, F. Guinea, and L. Martin-Moreno, "Resonant plasmonic effects in periodic graphene antidot arrays," *Applied Physics Letters* **101**, 151119 (2012).
39. V. W. Brar, M. S. Jang, M. Sherrott, J. J. Lopez, and H. A. Atwater, "Highly confined tunable mid-infrared plasmonics in graphene nanoresonators," *Nano Lett* **13**, 2541-2547 (2013).
40. T. J. Echtermeyer, S. Milana, U. Sassi, A. Eiden, M. Wu, E. Lidorikis, and A. C. Ferrari, "Surface Plasmon Polariton Graphene Photodetectors," *Nano Letters* **16**, 8-20 (2016).
41. G. X. Ni, L. Wang, M. D. Goldflam, M. Wagner, Z. Fei, A. S. McLeod, M. K. Liu, F. Keilmann, B. Ozyilmaz, A. H. C. Neto, J. Hone, M. M. Fogler, and D. N. Basov, "Ultrafast optical switching of infrared plasmon polaritons in high-mobility graphene," *Nature Photonics* **10**, 244-+ (2016).
42. S. Chakraborty, O. P. Marshall, T. G. Folland, Y. J. Kim, A. N. Grigorenko, and K. S. Novoselov, "Gain modulation by graphene plasmons in aperiodic lattice lasers," *Science* **351**, 246-248 (2016).
43. M. Z. Hasan and C. L. Kane, "Colloquium: Topological insulators," *Reviews of Modern Physics* **82**, 3045-3067 (2010).
44. W. Gao, J. Shu, C. Qiu, and Q. Xu, "Excitation of plasmonic waves in graphene by guided-mode resonances," *ACS nano* **6**, 7806-7813 (2012).
45. A. Y. Nikitin, F. Guinea, F. J. Garcia-Vidal, and L. Martin-Moreno, "Surface plasmon enhanced absorption and suppressed transmission in periodic arrays of graphene ribbons," *Physical Review B* **85**(2012).
46. S. Thongrattanasiri, F. H. Koppens, and F. J. Garcia de Abajo, "Complete optical absorption in periodically patterned graphene," *Phys Rev Lett* **108**, 047401 (2012).
47. L. Ju, B. Geng, J. Horng, C. Girit, M. Martin, Z. Hao, H. A. Bechtel, X. Liang, A. Zettl, Y. R. Shen, and F. Wang, "Graphene plasmonics for tunable terahertz metamaterials," *Nature nanotechnology* **6**, 630-634 (2011).
48. H. G. Yan, T. Low, W. J. Zhu, Y. Q. Wu, M. Freitag, X. S. Li, F. Guinea, P. Avouris, and F. N. Xia, "Damping pathways of mid-infrared plasmons in graphene nanostructures," *Nature Photonics* **7**, 394-399 (2013).
49. Z. Fang, Y. Wang, A. E. Schlather, Z. Liu, P. M. Ajayan, F. J. de Abajo, P. Nordlander, X. Zhu, and N. J. Halas, "Active tunable absorption enhancement with graphene nanodisk arrays," *Nano Lett* **14**, 299-304 (2014).
50. Z. Fang, S. Thongrattanasiri, A. Schlather, Z. Liu, L. Ma, Y. Wang, P. M. Ajayan, P. Nordlander, N. J. Halas, and F. J. Garcia de Abajo, "Gated tunability and hybridization of localized plasmons in nanostructured graphene," *ACS nano* **7**, 2388-2395 (2013).
51. J. C. W. Song, "Hot Carriers in Graphene," (Harvard University, 2014).

52. R. Kolesov, B. Grotz, G. Balasubramanian, R. J. Stohr, A. A. L. Nicolet, P. R. Hemmer, F. Jelezko, and J. Wrachtrup, "Wave-particle duality of single surface plasmon polaritons," *Nature Physics* **5**, 470-474 (2009).
53. J. A. Schuller, E. S. Barnard, W. Cai, Y. C. Jun, J. S. White, and M. L. Brongersma, "Plasmonics for extreme light concentration and manipulation," *Nature materials* **9**, 193-204 (2010).
54. S. A. Maier, *Plasmonic: Fundamentals and applications* (Springer, 2007).
55. C. Sonnichsen, T. Franzl, T. Wilk, G. von Plessen, and J. Feldmann, "Plasmon resonances in large noble-metal clusters," *New Journal of Physics* **4**(2002).
56. C. Sonnichsen, T. Franzl, T. Wilk, G. von Plessen, J. Feldmann, O. Wilson, and P. Mulvaney, "Drastic reduction of plasmon damping in gold nanorods," *Phys Rev Lett* **88**, 077402 (2002).
57. T. V. Shahbazyan, "Landau damping of surface plasmons in metal nanostructures," *Physical Review B* **94**(2016).
58. S. Mukherjee, F. Libisch, N. Large, O. Neumann, L. V. Brown, J. Cheng, J. B. Lassiter, E. A. Carter, P. Nordlander, and N. J. Halas, "Hot electrons do the impossible: plasmon-induced dissociation of H₂ on Au," *Nano Lett* **13**, 240-247 (2013).
59. F. Wang and N. A. Melosh, "Plasmonic energy collection through hot carrier extraction," *Nano Lett* **11**, 5426-5430 (2011).
60. J. Shah and R. C. C. Leite, "Radiative Recombination from Photoexcited Hot Carriers in GaAs," *Physical Review Letters* **22**, 1304-1307 (1969).
61. F. Huang, Y. Wang, X. Shen, G. Li, and S. Yan, "Analysis of space target detection range based on space-borne fisheye imaging system in deep space background," *Infrared Phys Techn* **55**, 475-480 (2012).
62. A. Karim and J. Y. Andersson, "Infrared detectors: Advances, challenges and new technologies," *IOP Conference Series: Materials Science and Engineering* **51**, 012001 (2013).
63. M. Santiago Cintrón, C. Fortier, D. J. Hinchliffe, and J. E. Rodgers, "Chemical imaging of secondary cell wall development in cotton fibers using a mid-infrared focal-plane array detector," *Textile Research Journal* **87**, 1040-1051 (2016).
64. M. P. Edgar, G. M. Gibson, R. W. Bowman, B. Sun, N. Radwell, K. J. Mitchell, S. S. Welsh, and M. J. Padgett, "Simultaneous real-time visible and infrared video with single-pixel detectors," *Scientific reports* **5**, 10669 (2015).
65. G. C. Dyer, J. D. Crossno, G. R. Aizin, E. A. Shaner, M. C. Wanke, J. L. Reno, and S. J. Allen, "A plasmonic terahertz detector with a monolithic hot electron bolometer," *Journal of Physics: Condensed Matter* **21**, 195803 (2009).
66. M. Mahjouri-Samani, Y. S. Zhou, X. N. He, W. Xiong, P. Hilger, and Y. F. Lu, "Plasmonic-enhanced carbon nanotube infrared bolometers," *Nanotechnology* **24**, 035502 (2013).
67. J. D. Vincent, *Fundamentals of Infrared Detector Operation & Testing* (John Wiley & Sons, New York, 1990).
68. U. Dillner, E. Kessler, and H. G. Meyer, "Figures of merit of thermoelectric and bolometric thermal radiation sensors," *Journal of Sensors and Sensor Systems* **2**, 85-94 (2013).
69. P. Dollfus, V. Hung Nguyen, and J. Saint-Martin, "Thermoelectric effects in graphene nanostructures," *Journal of physics. Condensed matter : an Institute of Physics journal* **27**, 133204 (2015).

70. Q. Guo, R. Yu, C. Li, S. Yuan, B. Deng, F. J. Garcia de Abajo, and F. Xia, "Efficient electrical detection of mid-infrared graphene plasmons at room temperature," *Nature materials* (2018).
71. X. Cai, A. B. Sushkov, R. J. Suess, M. M. Jadidi, G. S. Jenkins, L. O. Nyakiti, R. L. Myers-Ward, S. Li, J. Yan, D. K. Gaskill, T. E. Murphy, H. D. Drew, and M. S. Fuhrer, "Sensitive room-temperature terahertz detection via the photothermoelectric effect in graphene," *Nature nanotechnology* **9**, 814-819 (2014).
72. X. Xu, N. M. Gabor, J. S. Alden, A. M. van der Zande, and P. L. McEuen, "Photothermoelectric effect at a graphene interface junction," *Nano Lett* **10**, 562-566 (2010).
73. J. Duan, X. Wang, X. Lai, G. Li, K. Watanabe, T. Taniguchi, M. Zebarjadi, and E. Y. Andrei, "High thermoelectric power factor in graphene/hBN devices," *Proceedings of the National Academy of Sciences of the United States of America* **113**, 14272-14276 (2016).
74. L. A. Falkovsky and A. A. Varlamov, "Space-time dispersion of graphene conductivity," *Eur Phys J B* **56**, 281-284 (2007).
75. L. A. Falkovsky, "Optical properties of doped graphene layers," *J Exp Theor Phys+* **106**, 575-580 (2008).
76. R. R. Nair, P. Blake, A. N. Grigorenko, K. S. Novoselov, T. J. Booth, T. Stauber, N. M. Peres, and A. K. Geim, "Fine structure constant defines visual transparency of graphene," *Science* **320**, 1308 (2008).
77. E. Hecht, *Optics*, Fourth ed. (Addison Wesley, 2002).
78. F. M. Huang and N. I. Zheludev, "Super-Resolution without Evanescent Waves," *Nano Lett.* **9**, 1249-1254 (2009).
79. C. Pfeiffer and A. Grbic, "Metamaterial Huygens' surfaces: tailoring wave fronts with reflectionless sheets," *Phys Rev Lett* **110**, 197401 (2013).
80. J. Luo, H. Yu, M. Song, and Z. Zhang, "Highly efficient wavefront manipulation in terahertz based on plasmonic gradient metasurfaces," *Opt Lett* **39**, 2229-2231 (2014).
81. H. Shi, C. Du, and X. Luo, "Focal length modulation based on a metallic slit surrounded with grooves in curved depths," *Applied Physics Letters* **91**, 093111 (2007).
82. Z. Sun and H. K. Kim, "Refractive transmission of light and beam shaping with metallic nano-optic lenses," *Applied Physics Letters* **85**, 642-644 (2004).
83. S. Saxena, R. P. Chaudhary, A. Singh, S. Awasthi, and S. Shukla, "Plasmonic micro lens for extraordinary transmission of broadband light," *Scientific reports* **4**, 5586 (2014).
84. X. Wan, W. Xiang Jiang, H. Feng Ma, and T. Jun Cui, "A broadband transformation-optics metasurface lens," *Applied Physics Letters* **104**, 151601 (2014).
85. P. K. Jha, X. Ni, C. Wu, Y. Wang, and X. Zhang, "Metasurface-Enabled Remote Quantum Interference," *Phys Rev Lett* **115**, 025501 (2015).
86. M. Khorasaninejad, F. Aieta, P. Kanhaiya, M. A. Kats, P. Genevet, D. Rousso, and F. Capasso, "Achromatic Metasurface Lens at Telecommunication Wavelengths," *Nano Lett* **15**, 5358-5362 (2015).
87. B. Gjonaj, J. Aulbach, P. M. Johnson, A. P. Mosk, L. Kuipers, and A. Lagendijk, "Focusing and scanning microscopy with propagating surface plasmons," *Phys Rev Lett* **110**, 266804 (2013).
88. Z. W. Liu, J. M. Steele, W. Srituravanich, Y. Pikus, C. Sun, and Z. X., "Focusing surface plasmons with a plasmonic lens," *Nano Lett.* **5**, 1726-1729 (2005).

89. Y. Zhang, Y. Fu, and X. Zhou, "Investigation of Metallic Elliptical Nano-Pinholes Structure-Based Plasmonic Lenses: From Design to Testing," *Insciences Journal*, 18-29 (2011).
90. W. L. Barnes, A. Dereux, and T. W. Ebbesen, "Surface plasmon subwavelength optics," *Nature* **424**, 824-830 (2003).
91. H. J. Lezec, A. Degiron, E. Devaux, R. A. Linke, L. Martin-Moreno, F. J. Garcia-Vidal, and T. W. Ebbesen, "Beaming light from a subwavelength aperture," *Science* **297**, 820-822 (2002).
92. Y. Fu and X. Zhou, "Plasmonic Lenses: A Review," *Plasmonics* **5**, 287-310 (2010).
93. W. Srituravanich, L. Pan, Y. Wang, C. Sun, D. B. Bogy, and X. Zhang, "Flying plasmonic lens in the near field for high-speed nanolithography," *Nature nanotechnology* **3**, 733-737 (2008).
94. M. Khorasaninejad, W. T. Chen, R. C. Devlin, J. Oh, A. Y. Zhu, and F. Capasso, "Metalenses at visible wavelengths: Diffraction-limited focusing and subwavelength resolution imaging," *Science* **352**, 1190-1194 (2016).
95. M. Dupré, F. Lemoult, M. Fink, and G. Lerosey, "Exploiting spatiotemporal degrees of freedom for far-field subwavelength focusing using time reversal in fractals," *Physical Review B* **93**(2016).
96. D. Fattal, J. J. Li, Z. Peng, M. Fiorentino, and R. G. Beausoleil, "Flat dielectric grating reflectors with focusing abilities," *Nature Photonics* **4**, 466-470 (2010).
97. D. Lin, P. Fan, E. Hasman, and M. L. Brongersma, "Dielectric gradient metasurface optical elements," *Science* **345**, 298-302 (2014).
98. L. Verslegers, P. B. Catrysse, Z. Yu, J. S. White, E. S. Barnard, M. L. Brongersma, and S. Fan, "Planar lenses based on nanoscale slit arrays in a metallic film," *Nano Lett* **9**, 235-238 (2009).
99. X. Zheng, B. Jia, H. Lin, L. Qiu, D. Li, and M. Gu, "Highly efficient and ultra-broadband graphene oxide ultrathin lenses with three-dimensional subwavelength focusing," *Nature communications* **6**, 8433 (2015).
100. F. M. Huang, T. S. Kao, V. A. Fedotov, Y. F. Chen, and N. I. Zheludev, "Nanohole array as a lens," *Nano Lett.* **8**, 2469-2472 (2008).
101. A. Niv, G. Biener, V. Kleiner, and E. Hasman, "Spiral phase elements obtained by use of discrete space-variant subwavelength gratings," *Optics Communications* **251**, 306-314 (2005).
102. J. Hu, C. H. Liu, X. Ren, L. J. Lauhon, and T. W. Odom, "Plasmonic Lattice Lenses for Multiwavelength Achromatic Focusing," *ACS nano* **10**, 10275-10282 (2016).
103. A. V. Kildishev, A. Boltasseva, and V. M. Shalaev, "Planar photonics with metasurfaces," *Science* **339**, 1232009 (2013).
104. P. Biagioni, M. Savoini, J.-S. Huang, L. Duò, M. Finazzi, and B. Hecht, "Near-field polarization shaping by a near-resonant plasmonic cross antenna," *Physical Review B* **80**(2009).
105. C. L. Holloway, E. F. Kuester, J. A. Gordon, J. O'Hara, J. Booth, and D. R. Smith, "An Overview of the Theory and Applications of Metasurfaces: The Two-Dimensional Equivalents of Metamaterials," *Ieee Antenn Propag M* **54**, 10-35 (2012).
106. B. Walther, C. Helgert, C. Rockstuhl, F. Setzpfandt, F. Eilenberger, E. B. Kley, F. Lederer, A. Tunnermann, and T. Pertsch, "Spatial and spectral light shaping with metamaterials," *Advanced materials* **24**, 6300-6304 (2012).

107. Z. H. Jiang, S. Yun, L. Lin, J. A. Bossard, D. H. Werner, and T. S. Mayer, "Tailoring dispersion for broadband low-loss optical metamaterials using deep-subwavelength Inclusions," *Scientific reports* **3**, 1571 (2013).
108. X. Ni, N. K. Emani, A. V. Kildishev, A. Boltasseva, and V. M. Shalaev, "Broadband light bending with plasmonic nanoantennas," *Science* **335**, 427 (2012).
109. N. Yu, F. Aieta, P. Genevet, M. A. Kats, Z. Gaburro, and F. Capasso, "A broadband, background-free quarter-wave plate based on plasmonic metasurfaces," *Nano Lett* **12**, 6328-6333 (2012).
110. S. Sun, K. Y. Yang, C. M. Wang, T. K. Juan, W. T. Chen, C. Y. Liao, Q. He, S. Xiao, W. T. Kung, G. Y. Guo, L. Zhou, and D. P. Tsai, "High-efficiency broadband anomalous reflection by gradient meta-surfaces," *Nano Lett* **12**, 6223-6229 (2012).
111. S. L. Sun, Q. He, S. Y. Xiao, Q. Xu, X. Li, and L. Zhou, "Gradient-index meta-surfaces as a bridge linking propagating waves and surface waves," *Nat. Mater.* **11**, 426-431 (2012).
112. F. Aieta, P. Genevet, M. A. Kats, N. Yu, R. Blanchard, Z. Gaburro, and F. Capasso, "Aberration-free ultrathin flat lenses and axicons at telecom wavelengths based on plasmonic metasurfaces," *Nano Lett* **12**, 4932-4936 (2012).
113. X. Ni, S. Ishii, A. V. Kildishev, and V. M. Shalaev, "Ultra-thin, planar, Babinet-inverted plasmonic metalenses," *Light: Science & Applications* **2**, e72 (2013).
114. A. Pors, M. G. Nielsen, R. L. Eriksen, and S. I. Bozhevolnyi, "Broadband focusing flat mirrors based on plasmonic gradient metasurfaces," *Nano Lett* **13**, 829-834 (2013).
115. F. M. Huang, N. Zheludev, Y. Chen, and F. Javier Garcia de Abajo, "Focusing of light by a nanohole array," *Applied Physics Letters* **90**, 091119 (2007).
116. M. Khorasaninejad, W. T. Chen, A. Y. Zhu, J. Oh, R. C. Devlin, C. Roques-Carmes, I. Mishra, and F. Capasso, "Visible Wavelength Planar Metalenses Based on Titanium Dioxide," *Ieee J Sel Top Quant* **23**(2017).
117. W. Wang, X. Cui, E. Yang, Q. Fan, and B. Xiang, "Negative refraction in molybdenum disulfide," *Optics express* **23**, 22024-22033 (2015).
118. D. Vella, D. Ovchinnikov, N. Martino, V. Vega-Mayoral, D. Dumcenco, Y. C. Kung, M. R. Antognazza, A. Kis, G. Lanzani, D. Mihailovic, and C. Gadermaier, "Unconventional electroabsorption in monolayer MoS₂," *2D Materials* **4**, 021005 (2017).
119. P. Bharadwaj, B. Deutsch, and L. Novotny, "Optical Antennas," *Advances in Optics and Photonics* **1**, 438 (2009).
120. L. Novotny, "Antennas for light," *Nature Photonics* **5**, 83 (2011).
121. M. A. Kats, D. Sharma, J. Lin, P. Genevet, R. Blanchard, Z. Yang, M. M. Qazilbash, D. N. Basov, S. Ramanathan, and F. Capasso, "Ultra-thin perfect absorber employing a tunable phase change material," *Applied Physics Letters* **101**, 221101 (2012).
122. N. Fang, H. Lee, C. Sun, and X. Zhang, "Sub-diffraction-limited optical imaging with a silver superlens," *Science* **308**, 534-537 (2005).
123. S. Larouche and D. R. Smith, "Reconciliation of generalized refraction with diffraction theory," *Opt Lett* **37**, 2391-2393 (2012).
124. N. Yu, P. Genevet, M. A. Kats, F. Aieta, J. P. Tetienne, F. Capasso, and Z. Gaburro, "Light propagation with phase discontinuities: generalized laws of reflection and refraction," *Science* **334**, 333-337 (2011).
125. J. Lin, J. P. Mueller, Q. Wang, G. Yuan, N. Antoniou, X. C. Yuan, and F. Capasso, "Polarization-controlled tunable directional coupling of surface plasmon polaritons," *Science* **340**, 331-334 (2013).

126. F. Aieta, P. Genevet, N. Yu, M. A. Kats, Z. Gaburro, and F. Capasso, "Out-of-plane reflection and refraction of light by anisotropic optical antenna metasurfaces with phase discontinuities," *Nano Lett* **12**, 1702-1706 (2012).
127. J. W. Goodman, *Introduction To Fourier Optics*, Third ed. (Roberts & Company, Stanford University, 2005).
128. S. Kim, M. S. Jang, V. W. Brar, Y. Tolstova, K. W. Mauser, and H. A. Atwater, "Electronically tunable extraordinary optical transmission in graphene plasmonic ribbons coupled to subwavelength metallic slit arrays," *Nature communications* **7**, 12323 (2016).
129. Y. Hu, G.-q. Liu, Z.-q. Liu, X.-s. Liu, X.-n. Zhang, Z.-j. Cai, M.-l. Liu, H.-g. Gao, and G. Gu, "Extraordinary Optical Transmission in Metallic Nanostructures with a Plasmonic Nanohole Array of Two Connected Slot Antennas," *Plasmonics* **10**, 483-488 (2014).
130. F. Miyamaru, M. Kamijyo, N. Hanaoka, and M. W. Takeda, "Controlling extraordinary transmission characteristics of metal hole arrays with spoof surface plasmons," *Applied Physics Letters* **100**, 081112 (2012).
131. S. Fan, "Propagating plasmonic mode in nanoscale apertures and its implications for extraordinary transmission," *Journal of Nanophotonics* **2**, 021790 (2008).
132. Y. Ding, J. Yoon, M. H. Javed, S. H. Song, and R. Magnusson, "Mapping Surface-Plasmon Polaritons and Cavity Modes in Extraordinary Optical Transmission," *IEEE Photonics Journal* **3**, 365-374 (2011).
133. J. L. Briscoe and S. Y. Cho, "Hybridised extraordinary optical transmission in plasmonic cavity," *Electron Lett* **50**, 1860-U1227 (2014).
134. R. Ortuño, C. García-Meca, F. J. Rodríguez-Fortuño, J. Martí, and A. Martínez, "Role of surface plasmon polaritons on optical transmission through double layer metallic hole arrays," *Physical Review B* **79**(2009).
135. H. F. Ghaemi, T. Thio, D. E. Grupp, T. W. Ebbesen, and H. J. Lezec, "Surface plasmons enhance optical transmission through subwavelength holes," *Physical Review B* **58**, 6779-6782 (1998).
136. F. Przybilla, A. Degiron, C. Genet, T. W. Ebbesen, F. de Leon-Perez, J. Bravo-Abad, F. J. Garcia-Vidal, and L. Martin-Moreno, "Efficiency and finite size effects in enhanced transmission through subwavelength apertures," *Optics express* **16**, 9571-9579 (2008).
137. Y. Wang, W. Srituravanich, C. Sun, and X. Zhang, "Plasmonic nearfield scanning probe with high transmission," *Nano Lett* **8**, 3041-3045 (2008).
138. L. Yin, V. K. Vlasov, A. Rydh, J. Pearson, U. Welp, S. H. Chang, S. K. Gray, G. C. Schatz, D. B. Brown, and C. W. Kimball, "Surface plasmons at single nanoholes in Au films," *Applied Physics Letters* **85**, 467-469 (2004).
139. T. Thio, H. J. Lezec, and T. W. Ebbesen, "Strongly enhanced optical transmission through subwavelength holes in metal films," *Physica B* **279**, 90-93 (2000).
140. A. Degiron, H. J. Lezec, N. Yamamoto, and T. W. Ebbesen, "Optical transmission properties of a single subwavelength aperture in a real metal," *Optics Communications* **239**, 61-66 (2004).
141. F. Bonaccorso, Z. Sun, T. Hasan, and A. C. Ferrari, "Graphene photonics and optoelectronics," *Nature Photonics* **4**, 611-622 (2010).
142. L. A. Falkovsky and S. S. Pershoguba, "Optical far-infrared properties of a graphene monolayer and multilayer," *Physical Review B* **76**(2007).
143. V. Singh, D. Joung, L. Zhai, S. Das, S. I. Khondaker, and S. Seal, "Graphene based materials: Past, present and future," *Progress in Materials Science* **56**, 1178-1271 (2011).

144. F. Schwierz, "Graphene transistors," *Nature nanotechnology* **5**, 487-496 (2010).
145. M. Liu, X. Yin, E. Ulin-Avila, B. Geng, T. Zentgraf, L. Ju, F. Wang, and X. Zhang, "A graphene-based broadband optical modulator," *Nature* **474**, 64-67 (2011).
146. Z. Sun and H. Chang, "Graphene and graphene-like two-dimensional materials in photodetection: mechanisms and methodology," *ACS nano* **8**, 4133-4156 (2014).
147. Z. Liu, S. P. Lau, and F. Yan, "Functionalized graphene and other two-dimensional materials for photovoltaic devices: device design and processing," *Chemical Society reviews* (2015).
148. Z. Sun, T. Hasan, F. Torrisi, D. Popa, G. Privitera, F. Wang, F. Bonaccorso, D. M. Basko, and A. C. Ferrari, "Graphene mode-locked ultrafast laser," *ACS nano* **4**, 803-810 (2010).
149. H. Yan, F. Xia, W. Zhu, M. Freitag, C. Dimitrakopoulos, A. A. Bol, G. Tulevski, and P. Avouris, "Infrared spectroscopy of wafer-scale graphene," *ACS nano* **5**, 9854-9860 (2011).
150. J. H. Andrew R. Banman, "Mid-IR Excitation of Graphene," *Macalester Journal of Physics and Astronomy* **3**(2015).
151. H. P. Paudel, A. Safaei, and M. N. Leuenberger, " Nanoplasmonics in Metallic Nanostructures and Dirac Systems," in *Nanoplasmonics - Fundamentals and Applications*, D. G. Barbillon, ed. (InTech, 2017).
152. M. S. Jang, V. W. Brar, M. C. Sherrott, J. J. Lopez, L. Kim, S. Kim, M. Choi, and H. A. Atwater, "Tunable large resonant absorption in a midinfrared graphene Salisbury screen," *Physical Review B* **90**(2014).
153. M. Grande, M. A. Vincenti, T. Stomeo, G. V. Bianco, D. de Ceglia, N. Akozbek, V. Petruzzelli, G. Bruno, M. De Vittorio, M. Scalora, and A. D'Orazio, "Graphene-based absorber exploiting guided mode resonances in one-dimensional gratings," *Optics express* **22**, 31511-31519 (2014).
154. N. K. Emani, T. F. Chung, X. Ni, A. V. Kildishev, Y. P. Chen, and A. Boltasseva, "Electrically tunable damping of plasmonic resonances with graphene," *Nano Lett* **12**, 5202-5206 (2012).
155. T. Otsuji, V. Popov, and V. Ryzhii, "Active graphene plasmonics for terahertz device applications," *J Phys D Appl Phys* **47**, 094006 (2014).
156. Y. Zhang, Y. Feng, B. Zhu, J. Zhao, and T. Jiang, "Graphene based tunable metamaterial absorber and polarization modulation in terahertz frequency," *Optics express* **22**, 22743-22752 (2014).
157. A. Majumdar, J. Kim, J. Vuckovic, and F. Wang, "Graphene for Tunable Nanophotonic Resonators," *Ieee J Sel Top Quant* **20**(2014).
158. A. M. Brown, R. Sundararaman, P. Narang, W. A. Goddard, 3rd, and H. A. Atwater, "Nonradiative Plasmon Decay and Hot Carrier Dynamics: Effects of Phonons, Surfaces, and Geometry," *ACS nano* **10**, 957-966 (2016).
159. R. Alaee, M. Farhat, C. Rockstuhl, and F. Lederer, "A perfect absorber made of a graphene micro-ribbon metamaterial," *Optics express* **20**, 28017-28024 (2012).
160. D. Franklin, Y. Chen, A. Vazquez-Guardado, S. Modak, J. Boroumand, D. Xu, S. T. Wu, and D. Chanda, "Polarization-independent actively tunable colour generation on imprinted plasmonic surfaces," *Nature communications* **6**, 7337 (2015).
161. D. Chanda, K. Shigeta, T. Truong, E. Lui, A. Mihi, M. Schulmerich, P. V. Braun, R. Bhargava, and J. A. Rogers, "Coupling of plasmonic and optical cavity modes in quasi-three-dimensional plasmonic crystals," *Nature communications* **2**, 479 (2011).

162. A. Y. Nikitin, P. Alonso-Gonzalez, S. Velez, S. Mastel, A. Centeno, A. Pesquera, A. Zurutuza, F. Casanova, L. E. Hueso, F. H. L. Koppens, and R. Hillenbrand, "Real-space mapping of tailored sheet and edge plasmons in graphene nanoresonators," *Nature Photonics* **10**, 239-+ (2016).
163. Z. Fei, M. D. Goldflam, J. S. Wu, S. Dai, M. Wagner, A. S. McLeod, M. K. Liu, K. W. Post, S. Zhu, G. C. Janssen, M. M. Fogler, and D. N. Basov, "Edge and Surface Plasmons in Graphene Nanoribbons," *Nano Lett* **15**, 8271-8276 (2015).
164. A. Y. Nikitin, F. Guinea, F. J. García-Vidal, and L. Martín-Moreno, "Edge and waveguide terahertz surface plasmon modes in graphene microribbons," *Physical Review B* **84**(2011).
165. A. Safaei, S. Chandra, M. N. Leuenberger, and D. Chanda, "Tunable enhanced mid-infrared light absorption in graphene," in *CLEO: Applications and Technology*, (2017).
166. A. Safaei, S. Chandra, M. N. Leuenberger, and D. Chanda, "Wide Angle Electronically Tunable Enhanced Light Absorption in Nanopatterned Graphene," *Bulletin of the American Physical Society* **F14.00008**(2019).
167. D. Chanda, K. Shigeta, S. Gupta, T. Cain, A. Carlson, A. Mihi, A. J. Baca, G. R. Bogart, P. Braun, and J. A. Rogers, "Large-area flexible 3D optical negative index metamaterial formed by nanotransfer printing," *Nature nanotechnology* **6**, 402-407 (2011).
168. W. S. Weiglhofer, A. Lakhtakia, and B. Michel, "Maxwell Garnett and Bruggeman formalisms for a particulate composite with bianisotropic host medium (vol 15, pg 263, 1997)," *Microwave and Optical Technology Letters* **22**, 221-221 (1999).
169. C. G. Granqvist and O. Hunderi, "Conductivity of Inhomogeneous Materials - Effective-Medium Theory with Dipole-Dipole Interaction," *Physical Review B* **18**, 1554-1561 (1978).
170. G. W. Hanson, "Dyadic Green's functions and guided surface waves for a surface conductivity model of graphene," *Journal of Applied Physics* **103**, 064302 (2008).
171. D. V. van Coevorden, R. Sprik, A. Tip, and A. Lagendijk, "Photonic Band Structure of Atomic Lattices," *Phys Rev Lett* **77**, 2412-2415 (1996).
172. L. L. Zhao, K. L. Kelly, and G. C. Schatz, "The extinction spectra of silver nanoparticle arrays: Influence of array structure on plasmon resonance wavelength and width," *J Phys Chem B* **107**, 7343-7350 (2003).
173. H. Hirai, H. Tsuchiya, Y. Kamakura, N. Mori, and M. Ogawa, "Electron mobility calculation for graphene on substrates," *Journal of Applied Physics* **116**, 083703 (2014).
174. H. S. Song, S. L. Li, H. Miyazaki, S. Sato, K. Hayashi, A. Yamada, N. Yokoyama, and K. Tsukagoshi, "Origin of the relatively low transport mobility of graphene grown through chemical vapor deposition," *Scientific reports* **2**, 337 (2012).
175. J. H. Chen, W. G. Cullen, C. Jang, M. S. Fuhrer, and E. D. Williams, "Defect scattering in graphene," *Phys Rev Lett* **102**, 236805 (2009).
176. C. R. Dean, A. F. Young, I. Meric, C. Lee, L. Wang, S. Sorgenfrei, K. Watanabe, T. Taniguchi, P. Kim, K. L. Shepard, and J. Hone, "Boron nitride substrates for high-quality graphene electronics," *Nature nanotechnology* **5**, 722-726 (2010).
177. J. D. Jackson, *Classical Electrodynamics*, 3th ed. (Wiley, 1998).
178. N. D. M. Neil W. Ashcroft, *Solid state physics*, 1st ed. (College edition, 1976).
179. H. Weingartner, P. Sasisanker, C. Daguinet, P. J. Dyson, I. Krossing, J. M. Slattery, and T. Schubert, "The dielectric response of room-temperature ionic liquids: effect of cation variation," *J Phys Chem B* **111**, 4775-4780 (2007).

180. J. H. Cho, J. Lee, Y. Xia, B. Kim, Y. He, M. J. Renn, T. P. Lodge, and C. D. Frisbie, "Printable ion-gel gate dielectrics for low-voltage polymer thin-film transistors on plastic," *Nature materials* **7**, 900-906 (2008).
181. J. S. Ponraj, Z. Q. Xu, S. C. Dhanabalan, H. Mu, Y. Wang, J. Yuan, P. Li, S. Thakur, M. Ashrafi, K. McCoubrey, Y. Zhang, S. Li, H. Zhang, and Q. Bao, "Photonics and optoelectronics of two-dimensional materials beyond graphene," *Nanotechnology* **27**, 462001 (2016).
182. Y. Liu, A. Chadha, D. Zhao, J. R. Piper, Y. Jia, Y. Shuai, L. Menon, H. Yang, Z. Ma, S. Fan, F. Xia, and W. Zhou, "Approaching total absorption at near infrared in a large area monolayer graphene by critical coupling," *Applied Physics Letters* **105**, 181105 (2014).
183. E. H. Hwang and S. Das Sarma, "Dielectric function, screening, and plasmons in two-dimensional graphene," *Physical Review B* **75**(2007).
184. R. Fuchs and K. L. Kliewer, "Optical Modes of Vibration in an Ionic Crystal Slab," *Physical Review* **140**, A2076-A2088 (1965).
185. B. Wunsch, T. Stauber, F. Sols, and F. Guinea, "Dynamical polarization of graphene at finite doping," *New Journal of Physics* **8**, 318-318 (2006).
186. E. H. Hwang, R. Sensarma, and S. Das Sarma, "Plasmon-phonon coupling in graphene," *Physical Review B* **82**(2010).
187. J. Qian, M. J. Allen, Y. Yang, M. Dutta, and M. A. Stroschio, "Quantized long-wavelength optical phonon modes in graphene nanoribbon in the elastic continuum model," *Superlattices and Microstructures* **46**, 881-888 (2009).
188. A. A. Balandin, "Thermal properties of graphene and nanostructured carbon materials," *Nat Mater* **10**, 569-581 (2011).
189. D. L. Nika and A. A. Balandin, "Two-dimensional phonon transport in graphene," *Journal of physics. Condensed matter : an Institute of Physics journal* **24**, 233203 (2012).
190. R. Jalabert and S. Das Sarma, "Quasiparticle properties of a coupled two-dimensional electron-phonon system," *Physical review. B, Condensed matter* **40**, 9723-9737 (1989).
191. S. Hemmatiyani, M. Polini, A. Abanov, A. H. MacDonald, and J. Sinova, "Stable path to ferromagnetic hydrogenated graphene growth," *Physical Review B* **90**(2014).
192. Y. Lu, B. R. Goldsmith, N. J. Kybert, and A. T. C. Johnson, "DNA-decorated graphene chemical sensors," *Applied Physics Letters* **97**, 083107 (2010).
193. F. Yavari and N. Koratkar, "Graphene-Based Chemical Sensors," *The journal of physical chemistry letters* **3**, 1746-1753 (2012).
194. E. Singh, M. Meyyappan, and H. S. Nalwa, "Flexible Graphene-Based Wearable Gas and Chemical Sensors," *ACS applied materials & interfaces* **9**, 34544-34586 (2017).
195. S. Kim, M. S. Jang, V. W. Brar, K. W. Mauser, L. Kim, and H. A. Atwater, "Electronically Tunable Perfect Absorption in Graphene," *Nano Lett* **18**, 971-979 (2018).
196. C. Deng, W. Lin, G. Agnus, D. Dragoe, D. Pierucci, A. Ouerghi, S. Eimer, I. Barisic, D. Ravelosona, C. Chappert, and W. Zhao, "Reversible Charge-Transfer Doping in Graphene due to Reaction with Polymer Residues," *The Journal of Physical Chemistry C* **118**, 13890-13897 (2014).
197. S. Shin, S. Kim, T. Kim, H. Du, K. S. Kim, S. Cho, and S. Seo, "Graphene transfer with self-doping by amorphous thermoplastic resins," *Carbon* **111**, 215-220 (2017).
198. H. Kocer, S. Butun, E. Palacios, Z. Liu, S. Tongay, D. Fu, K. Wang, J. Wu, and K. Aydin, "Intensity tunable infrared broadband absorbers based on VO₂ phase transition using planar layered thin films," *Scientific reports* **5**, 13384 (2015).

199. M. Freitag, T. Low, L. Martin-Moreno, W. Zhu, F. Guinea, and P. Avouris, "Substrate-sensitive mid-infrared photoresponse in graphene," *ACS nano* **8**, 8350-8356 (2014).
200. Y. Liu, R. Cheng, L. Liao, H. Zhou, J. Bai, G. Liu, L. Liu, Y. Huang, and X. Duan, "Plasmon resonance enhanced multicolour photodetection by graphene," *Nature communications* **2**, 579 (2011).
201. P. Gowda, D. R. Mohapatra, and A. Misra, "Enhanced photoresponse in monolayer hydrogenated graphene photodetector," *ACS applied materials & interfaces* **6**, 16763-16768 (2014).
202. B. Y. Zhang, T. Liu, B. Meng, X. Li, G. Liang, X. Hu, and Q. J. Wang, "Broadband high photoresponse from pure monolayer graphene photodetector," *Nature communications* **4**, 1811 (2013).
203. N. M. Gabor, J. C. W. Song, Q. Ma, N. L. Nair, T. Taychatanapat, K. Watanabe, T. Taniguchi, L. S. Levitov, and P. Jarillo-Herrero, "Hot Carrier-Assisted Intrinsic Photoresponse in Graphene," *Science* **334**, 648-652 (2011).
204. A. C. Ferrari, J. C. Meyer, V. Scardaci, C. Casiraghi, M. Lazzeri, F. Mauri, S. Piscanec, D. Jiang, K. S. Novoselov, S. Roth, and A. K. Geim, "Raman spectrum of graphene and graphene layers," *Phys Rev Lett* **97**, 187401 (2006).
205. X. Tang, N. Reckinger, O. Poncelet, P. Louette, F. Urena, H. Idrissi, S. Turner, D. Cabosart, J. F. Colomer, J. P. Raskin, B. Hackens, and L. A. Francis, "Damage evaluation in graphene underlying atomic layer deposition dielectrics," *Scientific reports* **5**, 13523 (2015).
206. S. Kim, S. Shin, T. Kim, H. Du, M. Song, K. S. Kim, S. Cho, S. W. Lee, and S. Seo, "A reliable and controllable graphene doping method compatible with current CMOS technology and the demonstration of its device applications," *Nanotechnology* **28**, 175710 (2017).
207. M. Schubert, T. E. Tiwald, and C. M. Herzinger, "Infrared dielectric anisotropy and phonon modes of sapphire," *Physical Review B* **61**, 8187-8201 (2000).
208. R. Kim, V. Perebeinos, and P. Avouris, "Relaxation of optically excited carriers in graphene," *Physical Review B* **84**(2011).
209. E. H. Hwang, B. Y.-K. Hu, and S. Das Sarma, "Inelastic carrier lifetime in graphene," *Physical Review B* **76**(2007).
210. R. Murali, Y. Yang, K. Brenner, T. Beck, and J. D. Meindl, "Breakdown current density of graphene nanoribbons," *Applied Physics Letters* **94**, 243114 (2009).
211. T. Mueller, F. N. A. Xia, and P. Avouris, "Graphene photodetectors for high-speed optical communications," *Nature Photonics* **4**, 297-301 (2010).
212. M. P. Edgar, G. M. Gibson, and M. J. Padgett, "Principles and prospects for single-pixel imaging," *Nature Photonics* **13**, 13-20 (2018).
213. F. Yesilkoy, R. A. Terborg, J. Pello, A. A. Belushkin, Y. Jahani, V. Pruneri, and H. Altug, "Phase-sensitive plasmonic biosensor using a portable and large field-of-view interferometric microarray imager," *Light: Science & Applications* **7**, 17152 (2018).
214. P. Ginzburg, "Cavity quantum electrodynamics in application to plasmonics and metamaterials," *Reviews in Physics* **1**, 120-139 (2016).
215. F. Todisco, M. Esposito, S. Panaro, M. De Giorgi, L. Dominici, D. Ballardini, A. I. Fernandez-Dominguez, V. Tasco, M. Cuscuna, A. Passaseo, C. Ciraci, G. Gigli, and D. Sanvitto, "Toward Cavity Quantum Electrodynamics with Hybrid Photon Gap-Plasmon States," *ACS nano* **10**, 11360-11368 (2016).

216. L. Y. Hsu, W. Ding, and G. C. Schatz, "Plasmon-Coupled Resonance Energy Transfer," *The journal of physical chemistry letters* **8**, 2357-2367 (2017).
217. A. Vazquez-Guardado and D. Chanda, "Superchiral Light Generation on Degenerate Achiral Surfaces," *Phys Rev Lett* **120**, 137601 (2018).
218. J. B. Khurgin, "How to deal with the loss in plasmonics and metamaterials," *Nature nanotechnology* **10**, 2-6 (2015).
219. L. Lin and Y. Zheng, "Optimizing plasmonic nanoantennas via coordinated multiple coupling," *Scientific reports* **5**, 14788 (2015).
220. Z. Yong, S. Zhang, C. Gong, and S. He, "Narrow band perfect absorber for maximum localized magnetic and electric field enhancement and sensing applications," *Scientific reports* **6**, 24063 (2016).
221. Z. Liao, Y. Luo, A. I. Fernandez-Dominguez, X. Shen, S. A. Maier, and T. J. Cui, "High-order localized spoof surface plasmon resonances and experimental verifications," *Scientific reports* **5**, 9590 (2015).
222. C. Yan, K.-Y. Yang, and O. J. F. Martin, "Fano-resonance-assisted metasurface for color routing," *Light: Science & Applications* **6**, e17017 (2017).
223. G. Khitrova, H. M. Gibbs, F. Jahnke, M. Kira, and S. W. Koch, "Nonlinear optics of normal-mode-coupling semiconductor microcavities," *Reviews of Modern Physics* **71**, 1591-1639 (1999).
224. R. Ameling and H. Giessen, "Cavity plasmonics: large normal mode splitting of electric and magnetic particle plasmons induced by a photonic microcavity," *Nano Lett* **10**, 4394-4398 (2010).
225. Z. Wang, J. K. Clark, Y.-L. Ho, B. Vilquin, H. Daiguji, and J.-J. Delaunay, "Narrowband Thermal Emission Realized through the Coupling of Cavity and Tamm Plasmon Resonances," *ACS Photonics* **5**, 2446-2452 (2018).
226. W. Wang, J. Zhang, X. Che, and G. Qin, "Large Absorption Enhancement in Ultrathin Solar Cells Patterned by Metallic Nanocavity Arrays," *Scientific reports* **6**, 34219 (2016).
227. W. Ding and S. Y. Chou, "Plasmonic Nanocavity Organic Solar Cells with Highly Enhanced Power Conversion Efficiency, Broad-Band, and Omni-Acceptance," 2014 Ieee 40th Photovoltaic Specialist Conference (Pvsc), 2804-2807 (2014).
228. Y. Guo, L. Yan, W. Pan, B. Luo, and X. Luo, "Ultra-Broadband Terahertz Absorbers Based on 4×4 Cascaded Metal-Dielectric Pairs," *Plasmonics* **9**, 951-957 (2014).
229. Q. Feng, M. Pu, C. Hu, and X. Luo, "Engineering the dispersion of metamaterial surface for broadband infrared absorption," *Optics letters* **37**, 2133-2135 (2012).
230. M. Pu, C. Hu, M. Wang, C. Huang, Z. Zhao, C. Wang, Q. Feng, and X. Luo, "Design principles for infrared wide-angle perfect absorber based on plasmonic structure," *Optics express* **19**, 17413-17420 (2011).
231. A. Dorodnyy, Y. Salamin, P. Ma, J. V. Plestina, N. Lassaline, D. Mikulik, P. Romero-Gomez, A. F. I. Morral, and J. Leuthold, "Plasmonic Photodetectors," *Ieee J Sel Top Quant* **24**(2018).
232. A. Safaei, S. Modak, J. Lee, S. Chandra, D. Franklin, A. Vasquez-Gaurdado, and D. Chanda, "Multi-spectral frequency selective mid-infrared microbolometers," *Optics Express (Under revision)* (2018).
233. T. W. Ebbesen, Lezec, H. J., Ghaemi, H. F., Thio, T. & Wolff, P. A., "Extraordinary optical transmission through sub-wavelength hole arrays.," *Nature* **391**, 667 (1998).

234. W. J. Fan, S. Zhang, B. Minhas, K. J. Malloy, and S. R. J. Brueck, "Enhanced infrared transmission through subwavelength coaxial metallic arrays," *Physical Review Letters* **94**(2005).
235. J. B. Pendry, L. Martin-Moreno, and F. J. Garcia-Vidal, "Mimicking surface plasmons with structured surfaces," *Science* **305**, 847-848 (2004).
236. R. Stanley, "Plasmonics in the mid-infrared," *Nature Photonics* **6**, 409-411 (2012).
237. F. J. García de Abajo, "Colloquium: Light scattering by particle and hole arrays," *Reviews of Modern Physics* **79**, 1267-1290 (2007).
238. H. Paudel, A. Safaei, and M. Leuenberger, "Nanoplasmonics in Metallic Nanostructures and Dirac Systems," *IntechOpen* (2017).
239. S. A. Maier, *Plasmonics: Fundamentals and applications* (2007).
240. S. Modak, A. Safaei, and D. Chanda, "Cavity Induced Tunable Extraordinary Transmission: A Unique Way of Funneling Light through Subwavelength Apertures," eprint arXiv:1710.00392, arXiv:1710.00392 (2017).
241. A. Safaei, S. Chandra, A. Vázquez-Guardado, J. Calderon, D. Franklin, L. Tetard, L. Zhai, M. N. Leuenberger, and D. Chanda, "Dynamically tunable extraordinary light absorption in monolayer graphene," *Physical Review B* **96**, 165431 (2017).
242. M. L. Brongersma, N. J. Halas, and P. Nordlander, "Plasmon-induced hot carrier science and technology," *Nature Nanotechnology* **10**, 25 (2015).
243. W. D. Newman, C. L. Cortes, J. Atkinson, S. Pramanik, R. G. DeCorby, and Z. Jacob, "Ferrell–Berreman Modes in Plasmonic Epsilon-near-Zero Media," *ACS Photonics* **2**, 2-7 (2015).
244. R. de Waele, S. P. Burgos, H. A. Atwater, and A. Polman, "Negative refractive index in coaxial plasmon waveguides," *Optics express* **18**, 12770-12778 (2010).
245. F. Peragut, L. Cerutti, A. Baranov, J. P. Hugonin, T. Taliercio, Y. De Wilde, and J. J. Greffet, "Hyperbolic metamaterials and surface plasmon polaritons," *Optica* **4**, 1409-1415 (2017).
246. A. M. Brown, R. Sundararaman, P. Narang, W. A. Goddard, and H. A. Atwater, "Nonradiative Plasmon Decay and Hot Carrier Dynamics: Effects of Phonons, Surfaces, and Geometry," *ACS Nano* **10**, 957-966 (2016).
247. R. Sundararaman, P. Narang, A. S. Jermyn, W. A. Goddard Iii, and H. A. Atwater, "Theoretical predictions for hot-carrier generation from surface plasmon decay," *Nature communications* **5**, 5788 (2014).
248. T. D. Dao, K. Chen, S. Ishii, A. Ohi, T. Nabatame, M. Kitajima, and T. Nagao, "Infrared Perfect Absorbers Fabricated by Colloidal Mask Etching of Al–Al₂O₃–Al Trilayers," *ACS Photonics* **2**, 964-970 (2015).
249. T. D. Dao, S. Ishii, T. Yokoyama, T. Sawada, R. P. Sugavaneshwar, K. Chen, Y. Wada, T. Nabatame, and T. Nagao, "Hole Array Perfect Absorbers for Spectrally Selective Midwavelength Infrared Pyroelectric Detectors," *ACS Photonics* **3**, 1271-1278 (2016).
250. Y. Nishijima, A. Balčytis, S. Naganuma, G. Seniutinas, and S. Juodkazis, "Tailoring Metal and Insulator Contributions in Plasmonic Perfect Absorber Metasurfaces," *ACS Applied Nano Materials* **1**, 3557-3564 (2018).
251. J. Rosenberg, R. V. Shenoi, S. Krishna, and O. Painter, "Design of plasmonic photonic crystal resonant cavities for polarization sensitive infrared photodetectors," *Optics express* **18**, 3672-3686 (2010).

252. J. Rosenberg, R. V. Shenoi, T. E. Vandervelde, S. Krishna, and O. Painter, "A multispectral and polarization-selective surface-plasmon resonant midinfrared detector," *Applied Physics Letters* **95**, 161101 (2009).
253. T. Gu, A. Andryieuski, Y. Hao, Y. Li, J. Hone, C. W. Wong, A. Lavrinenko, T. Low, and T. F. Heinz, "Photonic and Plasmonic Guided Modes in Graphene–Silicon Photonic Crystals," *ACS Photonics* **2**, 1552-1558 (2015).
254. J.-K. Yang, M.-K. Seo, I.-K. Hwang, S.-B. Kim, and Y.-H. Lee, "Polarization-selective resonant photonic crystal photodetector," *Applied Physics Letters* **93**, 211103 (2008).
255. X. Hu, M. Li, Z. Ye, W. Y. Leung, K.-M. Ho, and S.-Y. Lin, "Design of midinfrared photodetectors enhanced by resonant cavities with subwavelength metallic gratings," *Applied Physics Letters* **93**, 241108 (2008).
256. J. S. White, G. Veronis, Z. F. Yu, E. S. Barnard, A. Chandran, S. H. Fan, and M. L. Brongersma, "Extraordinary optical absorption through subwavelength slits," *Optics letters* **34**, 686-688 (2009).
257. N. I. Landy, S. Sajuyigbe, J. J. Mock, D. R. Smith, and W. J. Padilla, "Perfect Metamaterial Absorber," *Physical review letters* **100**, 207402 (2008).
258. D. Li and D. Pacifici, "Strong amplitude and phase modulation of optical spatial coherence with surface plasmon polaritons," *Science Advances* **3**(2017).
259. A. S. Gawarikar, R. P. Shea, and J. J. Talghader, "High Detectivity Uncooled Thermal Detectors With Resonant Cavity Coupled Absorption in the Long-Wave Infrared," *IEEE Transactions on Electron Devices* **60**, 2586-2591 (2013).
260. F. B. P. Niesler, J. K. Gansel, S. Fischbach, and M. Wegener, "Metamaterial metal-based bolometers," *Applied Physics Letters* **100**, 203508 (2012).
261. J. Y. Suen, K. Fan, J. Montoya, C. Bingham, V. Stenger, S. Sriram, and W. J. Padilla, "Multifunctional metamaterial pyroelectric infrared detectors," *Optica* **4**, 276-279 (2017).
262. D. D. Coon, R. P. G. Karunasiri, and L. Z. Liu, "Narrow band infrared detection in multiquantum well structures," *Applied Physics Letters* **47**, 289-291 (1985).
263. Z. Qian, S. Kang, V. Rajaram, and M. Rinaldi, "Narrowband MEMS resonant infrared detectors based on ultrathin perfect plasmonic absorbers," in *2016 IEEE SENSORS*, 2016), 1-3.
264. G. C. Dyer, G. R. Aizin, J. L. Reno, E. A. Shaner, and S. J. Allen, "Novel Tunable Millimeter-Wave Grating-Gated Plasmonic Detectors," *IEEE Journal of Selected Topics in Quantum Electronics* **17**, 85-91 (2011).
265. J. J. Talghader, A. S. Gawarikar, and R. P. Shea, "Spectral selectivity in infrared thermal detection," *Light: Science & Applications* **1**, e24 (2012).
266. K. C. Liddiard, "Thin-Film Resistance Bolometer IR Detectors," *Infrared Phys.* **24**, 57-64 (1984).
267. Frank Niklaus, Christer Jansson, Adit Decharat, Jan-Erik Källhammer, Håkan Pettersson, and Göran Stemme, "Uncooled infrared bolometer arrays operating in a low to medium vacuum atmosphere: performance model and tradeoffs," in *Infrared Technology and Applications XXXIII*, (SPIE, 2007),
268. P. Bouchon, F. Pardo, B. Portier, L. Ferlazzo, P. Ghenuche, G. Dagher, C. Dupuis, N. Bardou, R. Haïdar, and J.-L. Pelouard, "Total funneling of light in high aspect ratio plasmonic nanoresonators," *Applied Physics Letters* **98**, 191109 (2011).
269. R. Wood, *Monolithic silicon microbolometer arrays*, Uncooled Infrared Imaging Arrays and Systems (Academic Press, 1997), Vol. 47.

270. E. L. Dereniak and G. D. Boreman, *Infrared Detectors and Systems* (John Wiley & Sons, Inc).
271. A. Rogalski, "Infrared detectors: an overview," *Infrared Physics & Technology* **43**, 187-210 (2002).
272. A. Rogalski, J. Antoszewski, and L. Faraone, "Third-generation infrared photodetector arrays," *Journal of Applied Physics* **105**, 091101 (2009).
273. P. W. Kruse, *Uncooled thermal imaging : arrays, systems, and applications / Paul W. Kruse*, Tutorial texts in optical engineering: v. TT 51 (Bellingham, Wash., USA : SPIE Press, c2001., 2001).
274. S. D. Gunapala, S. V. Bandara, J. K. Liu, J. M. Mumolo, S. B. Rafol, D. Z. Ting, A. Soibel, and C. Hill, "Quantum Well Infrared Photodetector Technology and Applications," *Ieee J Sel Top Quant* **20**(2014).
275. D. M. T. Kuo, A. B. Fang, and Y. C. Chang, "Theoretical modeling of dark current and photo-response for quantum well and quantum dot infrared detectors," *Infrared Phys Techn* **42**, 433-442 (2001).
276. A. Vázquez-Guardado, A. Safaei, S. Modak, D. Franklin, and D. Chanda, "Hybrid Coupling Mechanism in a System Supporting High Order Diffraction, Plasmonic, and Cavity Resonances," *Physical review letters* **113**, 263902 (2014).
277. E. D. Palik, "Handbook of Optical-Constants," *J Opt Soc Am A* **1**, 1297-1297 (1984).
278. R. W. Ziolkowski, "Propagation in and scattering from a matched metamaterial having a zero index of refraction," *Physical review. E, Statistical, nonlinear, and soft matter physics* **70**, 046608 (2004).
279. Ernst Jan R. Vesseur, Toon Coenen, Humeyra Caglayan, Nader Engheta, and A. Polman, "Experimental Verification of $n = 0$ Structures for Visible Light," *Physical review letters* **110**(2013).
280. A. M. Mahmoud and N. Engheta, "Wave-matter interactions in epsilon-and-mu-near-zero structures," *Nature communications* **5**, 5638 (2014).
281. J. C. Mather, "Electrical Self-Calibration of Nonideal Bolometers," *Appl Optics* **23**, 3181-3183 (1984).
282. M. Ou-Yang, C. S. Sheen, and J. S. Shie, "Parameter extraction of resistive thermal microsensors by AC electrical method," *Ieee T Instrum Meas* **47**, 403-408 (1998).
283. Y. M. Chen, J. S. Shie, and T. Hwang, "Parameter extraction of resistive thermal sensors," *Sensor Actuat a-Phys* **55**, 43-47 (1996).
284. J. B. Herzog, M. W. Knight, and D. Natelson, "Thermoplasmonics: quantifying plasmonic heating in single nanowires," *Nano Lett* **14**, 499-503 (2014).
285. A. Varpula, A. V. Timofeev, A. Shchepetov, K. Grigoras, J. Hassel, J. Ahopelto, M. Ylilammi, and M. Prunnila, "Thermoelectric thermal detectors based on ultra-thin heavily doped single-crystal silicon membranes," *Applied Physics Letters* **110**, 262101 (2017).
286. G. Wang, V. Yefremenko, V. Novosad, J. Pearson, R. Divan, C. L. Chang, L. Bleem, A. T. Crites, J. Mehl, B. A. Benson, T. Natoli, K. Story, S. S. Meyer, J. E. Carlstrom, J. McMahan, J. Sayre, J. Ruhl, E. George, N. Harrington, C. Reichardt, E. Shirokoff, E. Young, A. Lee, and W. Holzappel, "An Absorber-coupled TES Bolometer for Measuring CMB Polarization," *Physics Procedia* **37**, 1349-1354 (2012).
287. L. F. Zou, W. Withayachumnankul, C. M. Shah, A. Mitchell, M. Bhaskaran, S. Sriram, and C. Fumeaux, "Dielectric resonator nanoantennas at visible frequencies," *Optics express* **21**, 1344-1352 (2013).

288. H. Zuo, D.-Y. Choi, X. Gai, P. Ma, L. Xu, D. N. Neshev, B. Zhang, and B. Luther-Davies, "High-Efficiency All-Dielectric Metalenses for Mid-Infrared Imaging," *Advanced Optical Materials* **5**, 1700585 (2017).
289. A. Arbabi, R. M. Briggs, Y. Horie, M. Bagheri, and A. Faraon, "Efficient dielectric metasurface collimating lenses for mid-infrared quantum cascade lasers," *Optics express* **23**, 33310-33317 (2015).
290. R. D. H. Jr, *Infrared System Engineering*, 1st Edition ed. (John Wiley & Sons, 2006).
291. J. J. Talghader, A. S. Gawarikar, and R. P. Shea, "Spectral selectivity in infrared thermal detection," *Light: Science & Applications* **1**, e24-e24 (2012).
292. V. Giannini, A. I. Fernandez-Dominguez, S. C. Heck, and S. A. Maier, "Plasmonic nanoantennas: fundamentals and their use in controlling the radiative properties of nanoemitters," *Chemical reviews* **111**, 3888-3912 (2011).
293. O. Akin and H. V. Demir, "Mid-wave infrared metasurface microlensed focal plane array for optical crosstalk suppression," *Optics express* **23**, 27020-27027 (2015).
294. J. P. Tetienne, R. Blanchard, N. Yu, P. Genevet, M. A. Kats, J. A. Fan, T. Edamura, S. Furuta, M. Yamanishi, and F. Capasso, "Dipolar modeling and experimental demonstration of multi-beam plasmonic collimators," *New J Phys* **13**, 053057 (2011).
295. E. Verhagen, A. Polman, and L. K. Kuipers, "Nanofocusing in laterally tapered plasmonic waveguides," *Optics express* **16**, 45-57 (2008).
296. A. Safaei, M. N. Leuenberger, and D. Chanda, "Mid-infrared high-efficiency plasmonic flat lens," in *Photonic and Phononic Properties of Engineered Nanostructures VII*, (International Society for Optics and Photonics, 2017), p. 101120P.
297. O. J. Martin, C. Girard, and A. Dereux, "Generalized Field Propagator for Electromagnetic Scattering and Light Confinement," *Phys Rev Lett* **74**, 526-529 (1995).
298. A. B. Evlyukhin, C. Reinhardt, E. Evlyukhin, and B. N. Chichkov, "Multipole analysis of light scattering by arbitrary-shaped nanoparticles on a plane surface," *J Opt Soc Am B* **30**, 2589-2598 (2013).
299. S. Modak, A. Safaei, and D. Chanda, "Cavity Induced Tunable Extraordinary Transmission: A Unique Way of Funneling Light through Subwavelength Apertures," *arXiv* **1710.00392**(2017).
300. D. R. H. CRAIG F. BOHREN *Absorption and Scattering of Light by Small Particles* (John Wiley & Sons, Inc. , 1998).
301. P. Wang, N. Mohammad, and R. Menon, "Chromatic-aberration-corrected diffractive lenses for ultra-broadband focusing," *Scientific reports* **6**, 21545 (2016).
302. K. R and J. R. B, *Fundamentals of Light Microscopy and Electronic Imaging*, 2nd ed. (John Wiley & Sons, 2009).
303. F. Aieta, P. Genevet, M. Kats, and F. Capasso, "Aberrations of flat lenses and aplanatic metasurfaces," *Optics express* **21**, 31530-31539 (2013).